One-Dimensional Cold Filling Simulation of a Molten Salt Central Receiver Pipe

by
Jean Jacques Swart

Thesis presented in partial fulfilment of the requirements for the degree of Master of Engineering (Mechanical) in the Faculty of Engineering at Stellenbosch University

Supervisor: Dr JE Hoffmann

December 2017

DECLARATION

By submitting this thesis electronically, I declare that the entirety of the work contained therein is my own, original work, that I am the sole author thereof (save to the extent explicitly otherwise stated), that reproduction and publication thereof by Stellenbosch University will not infringe any third party rights and that I have not previously in its entirety or in part submitted it for obtaining any qualification.

Date: December 2017

ABSTRACT

One-Dimensional Transient Cold Filling Simulation of a Molten Salt Central Receiver Pipe

JJ Swart
Department of Mechanical and Mechatronic Engineering
Stellenbosch University
Private Bag X1, 7602 Matieland, South Africa
Thesis: M. Eng (Mechanical)
December 2017

In this study, cold filling was investigated as a more efficient means of filling a receiver panel with molten salt, eliminating or reducing the need for trace heating before filling the panel. Cold filling can be defined as the filling of a receiver that is initially at a temperature below the molten salt freezing temperature. A one-dimensional numerical model was developed to enable the investigation of the molten salt characteristic response during cold filling under various conditions.

The model was verified and then validated against two cold filling studies to ensure that it produces reliable results. Some differences were observed between the results produced by the model built in the current study and the validation studies, but the characteristic trends proved to correlate well. As a result, it was determined that the validation was sufficient for the investigation of the molten salt characteristic trends, as was required by this study.

A test case scenario was investigated where the molten salt temperature and solidification behaviour as well as the receiver tube temperature was analysed. It was evident from the test results that the molten salt temperature decreases with distance and increases with time. A worst-case scenario, where the receiver was subjected to strong wind and rain during the filling process, was also investigated. Although possible, it is suggested that cold filling should not be used under such harsh conditions so that damage to the receiver pipes may be prevented. Additionally, the effect that changing the size of the receiver pipe has on the cold filling characteristics was determined. Larger pipes proved to have superior cold filling characteristics up to a certain pipe size. As a result, both the filling characteristics and the molten salt response during normal heated operation need to be considered when choosing the receiver pipe size. Finally, the effect that using a different salt mixture has on the filling process was considered. It was determined that Hitec™ salt has superior cold filling properties compared to Solar Salt, but Solar Salt has a higher upper operating temperature and is less expensive. A plant specific analysis is, therefore, required to determine which salt type is operationally better.

UITTREKSEL

Eendimensionele Transiënte Koue Vulling van ‘n Gesmelte Sout Sentrale Ontvangerpyp

JJ Swart
Departement van Meganies and Megatroniese Ingenieurswese
Universiteit Stellenbosch
Privaatsak X1, 7602 Matieland, Suid-Afrika
Tesis: M. Ing (Meganies)
Desember 2017

In die huidige studie word koue vulling ondersoek as ‘n meer doeltreffende manier om ‘n ontvanger paneel met gesmelte sout te vul, eeder as om die paneel te voorverhit met elektriese verhitting. Koue vulling word gedefinieer as die vul van ‘n ontvangerpyp wat aanvanklik by ‘n temperatuur onder die gesmelte sout se vriespunt is. ‘n Eendimensionele numeriese model is ontwikkel om die gesmelte sout se reaksie tydens koue vulling onder verskeie toestande te ondersoek.

Die model is geverifieer en toe teen twee koue vulling studies gevalideer om te verseker dat dit betroubare resultate lewer. Verskille tussen hierdie studie se resultate en die resultate van die validasie studies, is waargeneem. Die gesmelte sout se kenmerkende tendense het egter goed vergelyk met die validasie data. Die doel van die studie is om die gesmelte sout se kenmerkende tendense en reaksies onder ‘n verskeidenheid omstandighede te ondersoek. Daar is bepaal dat die validasie voldoende is vir die doeleindes van hierdie studie.

‘n Toets scenario is ondersoek om die gesmelte sout se temperatuur, snelheid en stollingsgedrag te bepaal. Daar is bevind dat die gesmelte sout se temperatuur daal oor afstand en styg met tyd. ‘n Ergste geval scenario is ook ondersoek waar die onvangerpyp aan sterk wind en swaar reën blootgestel is. Alhoewel koue vulling onder hierdie onstandighede moontlik is, word dit nie aanbeveel nie, omdat dit skade aan die ontvangerpype kan veroorsaak. Die effek wat ‘n verandering in die grootte van die pyp op die koue vulling eienskappe het, is ook bepaal. Die bevindinge dui daarop dat groter pype beter koue vulling eienskappe toon tot ‘n bepaalde pypgrootte. Die gevolgtrekking is dat beide die koue vulling eienskappe en die gesmelte sout se reaksie tydens die normale verhittingsproses in ag geneem moet word wanneer die ontvangerpype se grootte gekies word. Laastens is die impak, wat die gebruik van ‘n alternatiewe sout tipe op die koue vulling proses het, ook ondersoek. Die studie het bevind dat Hitec™ sout beter koue vulling eienskappe toon as Solar Salt, maar dat Solar Salt ‘n hoër boonste bedryfstemperatuur het en goedkoper is. ‘n Aanleg spesifieke ontleding word dus benodig om die beste operasionele sout tipe te bepaal.

ACKNOWLEDGEMENTS

Thank you to

Dr. Jaap Hoffmann for his continual guidance and willingness to help.

The **STERG** group and the **NRF** for funding throughout this thesis.

Parents and **parents in-law** for their support.

Liesel, my wife, for her loving support and understanding.

God for giving me the strength and peace required to complete this thesis.

TABLE OF CONTENTS

Declaration i
Abstract ii
Uittreksel iii
Acknowledgements iv
Table of Contents v
List of Tables vii
List of Figures viii
List of Acronyms ix
List of Symbols ix
CHAPTER 1: Introduction 1
1.1 Background 1
1.2 Problem Statement 2
1.3 Objectives 2
CHAPTER 2: Literature Study 3
2.1 Commercial Molten Salt Mixtures 3
2.2 Central Receiver Plant 7
2.2.1 Overview 7
2.2.2 Components 8
2.3 Start-up and Shutdown 10
2.3.1 Operating Modes 10
2.3.2 Freeze Protection and Receiver Filling 12
2.3.3 Cold Filling and Receiver Freeze Up 12
2.4 Modelling Tools 16
2.5 Literature Study Conclusion 20
CHAPTER 3: Modelling Theory 21
3.1 Pipe Model 21
3.2 Heat Transfer Fluid Model 24
3.3 Rain Model 27
CHAPTER 4: Model Development 29
4.1 Physical Description of the Model 29
4.2 Modelling Methodology 31
4.3 Mathematical Modelling of the Receiver 32
4.3.1 Property Functions 33
4.3.2 Pressure and Velocity Relations 35
4.3.3 Mathematical Model of the Heat Transfer Fluid 40
4.3.4 Mathematical Model of the Frozen Salt Layer 47
4.3.5 Mathematical Model of the Receiver Tube 50
CHAPTER 5: Verification and Validation 58
5.1 Verification 58
5.2 Validation 59
CHAPTER 6: Results 65
6.1 Molten Salt Characteristics 66
6.2 Extreme Weather Analysis 70
6.3 Pipe Size Analysis 73
6.4 Salt Type and Property Function Analysis 75
6.4.1 Solar Salt and Hitec™ Salt Comparison 75
6.4.2 Solar Salt Property Function Comparison 77

CHAPTER 7: Conclusions 80
CHAPTER 8: Future Work 82
Appendix A: Multiple Tube Calculations 83
Appendix B: MATLAB Code 86
B.1 Main Script 86
B.2 Molten Salt Property Function Scripts 99
B.3 Air Property Function Scripts 100
B.4 Velocity Sub-function Script 101
B.5 Pressure Sub-Function Script 103
B.6 Molten Salt Sub-function Script 104
B.7 Solid Salt Sub-function Script 106
B.8 Receiver Tube Sub-function Script 109
References 113

LIST OF TABLES

Table 2.1: Characteristics of nitrate salts (Kearney et al., 2003) 4
Table 2.2: Effective storage medium cost (Kearney et al., 2003) 4
Table 2.3: Solar Salt properties (Ferri et al., 2008) 4
Table 2.4: Hitec^{TM} salt properties (Wu et al., 2012) 5
Table 2.5: Solar Salt properties - global review (Serrano-López et al., 2013) 6
Table 2.6: Hitec^{TM} salt properties - global review (Serrano-López et al., 2013) 6
Table 2.7: MSEE results and penetration distance correlation results (Pacheco et al., 1995) 13
Table 2.8: Receiver freezing test scenarios (Pacheco & Dunkin, 1996) 14
Table 4.1: Solar salt properties used in current study (Xu et al. (2017) 35
Table 6.1: Hitec^{TM} salt properties suggested in this study 75
Table 6.2: Solar Salt property functions suggested in this study 77

LIST OF FIGURES

Figure 2.1: Central receiver plant schematic (Ortega et al., 2008) 8
Figure 3.1: Receiver pipe heat transfer assumptions (Doupis et al., 2016) 21
Figure 3.2: Receiver pipe heat flux distribution (Yang et al., 2012) 22
Figure 3.3: Receiver pipe heat transfer and fluid flow schematic (Zhang et al., 2015) 22
Figure 3.4: Receiver pipe during pumping (Lu et al., 2013) 23
Figure 3.5: Receiver pipe filling process (Lu et al., 2013) 24
Figure 3.6: Common interface morphologies (Alexiades, 1992) 25
Figure 3.7: Spray-wall impingement regimes (Jafari, 2014) 28
Figure 4.1: Flood mode receiver panel filling (Liao et al., 2015) 30
Figure 4.2: First validation model depiction (Liao et al., 2015) 31
Figure 4.3: System mass balance 39
Figure 4.4: System heat transfer - with freezing 40
Figure 4.5: System heat transfer - without freezing 41
Figure 4.6: Molten salt heat transfer 41
Figure 4.7: Solid salt heat transfer 48
Figure 4.8: Steel receiver tube heat transfer 50
Figure 5.1: Relative error between different time steps and spatial increments 58
Figure 5.2: Receiver pressure drop versus distance (T_{ms_inlet} = 445 K, t = 1.75 s) 60
Figure 5.3: Molten salt temperature versus distance (T_{ms_inlet} = 445 K, t = 1.75 s) 61
Figure 5.4: Receiver pressure drop versus time (T_{ms} = 295 K) 62
Figure 5.5: Molten salt velocity versus time (T_{ms_inlet} = 295 K, z = 0 m) 63
Figure 5.6: Critical inlet molten salt temperatures for different initial receiver tube temperatures at different velocities (Xu et al. (2017) 64
Figure 5.7: Critical inlet molten salt temperatures for different initial receiver tube temperatures at different velocities (current study data) 64
Figure 6.1: Test case - liquid fraction versus distance (t = 1.75 s) 66
Figure 6.2: Test case - liquid fraction versus time for five distances 67
Figure 6.3: Test case - molten salt temperature versus distance at different times 68
Figure 6.4: Test case - molten salt temperature versus time for five distances . 69
Figure 6.5: Test case - molten salt and receiver tube temperatures versus time70
Figure 6.6: Extreme weather - molten salt and receiver tube temperatures versus time 71
Figure 6.7: Extreme weather - molten salt temperature versus time for five distances 72
Figure 6.8: Critical inlet molten salt temperatures, outlet molten salt temperatures and internal pipe areas with trend lines for five different internal pipe diameters 74
Figure 6.9: Solar Salt - molten salt temperature versus distance at different times 76
Figure 6.10: Hitec^{TM} - molten salt temperature versus distance at different times 76
Figure 6.11: Solar Salt property comparison - molten salt temperature versus time for five distances 78
Figure A.1: Multiple tube receiver layout 83

LIST OF ACRONYMS

CFD	Computational Fluid Dynamics
CSP	Concentrated Solar Power
DNI	Direct Normal Irradiance
FEA	Finite Element Analysis
HTF	Heat Transfer Fluid
LCOE	Levelised Cost of Electricity
MS	Molten Salt

LIST OF SYMBOLS

Roman:

A	Area
c_p	Specific Heat
C	Solar Concentration Ratio
d	Diameter
dt	Time Step Size
dz	Spatial Increment Size
E	Energy
F	Start-up Factor
Fn	Shape Factor
f	Friction Factor
f_l	Liquid Phase Content
f_S	Solid Phase Content
g	Gravity
H	Height
h	Heat Transfer Coefficient
k	Thermal Conductivity
L	Length
L_h	Latent Heat of Fusion
m	Mass
$\dot{m}$	Mass Flow Rate
Nu	Nusselt Number
N_f	Number of Cycles to Failure
P	Pressure
Pr	Prandtl Number
Q	Heat Transfer
$\dot{Q}$	Heat Transfer Rate
q	Heat Flux
R	Thermal Resistance
Ra	Rayleigh Number
Re	Reynolds Number
Re_p	Droplet Reynolds Number
r	Radius
T	Temperature
t	Time
$\dot{V}$	Volume Flow Rate
V_s	Wetting Intensity

v	Velocity
z	Distance to Freeze Closed

Greek:

α	Thermal Diffusivity
γ	Latent to Sensible Heat Importance Parameter
ε	Emissivity
η	Efficiency
θ	Angle of Incoming Solar Irradiance
μ	Dynamic Viscosity
ν	Kinematic Viscosity
ξ	Local Pressure Loss Coefficient
ρ	Density
σ	Stephan-Boltzmann Constant

Superscript:

i	Spatial increment Iteration
n	Tube Number

Subscript:

a	Air
B	Bend
cs	Cross Section
cs_f	Cross Section with Freezing
DNI	Direct Normal Irradiance
ext	External
H	Horizontal
in	Inlet
int	Internal
k	Time Step Iteration
LH	Latent Heat
ms	Molten Salt
out	Outlet
PB	Power Block
pu	Pump
r	Rain
re	Receiver
S	Solid
s	Steel
sky	Sky
ss	Solid Salt
w	Wind

CHAPTER 1: INTRODUCTION

1.1 Background

Fossil fuel sources are steadily being depleted, leading to ever rising conventional fuel based energy costs. This limited conventional fuel supply as well as the high CO_2 emissions from these hydrocarbon fuel sources is resulting in an increasing need for environmentally friendly and sustainably generated electricity. Solar thermal power plants, especially Concentrated Solar Power (CSP) plants, have great potential to help solve these problems.

A central receiver plant consists of a single tower located at the centre of a heliostat field. The heliostat field reflects the energy from the sun onto the top of the central receiver tower, where there plant's receiver is located. This receiver consists of a larger number of thin, vertically orientated tubes, which have a heat transfer fluid (HTF) running through them to transport the captured heat to the rest of the plant.

These central receiver plants operate at high temperatures that allow them to produce the highest efficiencies of all the current commercially active solar thermal power plants (El Hefni & Soler, 2015). El Hefni and Soler (2015) note that using molten salt as a HTF and coupling it with molten salt thermal energy storage can aid in overcoming solar powered electricity generation's largest challenge – the ability to produce electricity continuously. This study will consider such a central receiver plant with molten salt as its HTF.

Unfortunately, solar energy is only available intermittently as a result of the day/night cycle, clouds, maintenance and periods of low direct normal irradiance (DNI), such as in winter. Even with the progress that has been made in thermal energy storage, only a few CSP plants can run continuously for extended periods. Additionally, most countries' renewable energy feed-in-tariff policies do not support electricity production during night-time when the electricity demand is low. The result is a discontinuous energy input, which means that the plant has to start up and shut down regularly. This makes it exceedingly important to model the transient behaviour of the plant.

Extensive work has been done on modelling CSP plant's start up and shut down strategies, but little work has been done relating to the filling and draining of these plant's receivers. In general, a plant operator fills the receiver with HTF when it is expected to receiver heat from the solar field and then drains the receiver again when an extended period of zero irradiance is expected. In this study, the filling of a receiver tube with molten salt will be evaluated.

Molten salts have freezing temperatures ranging from 120 °C to 220 °C depending on the mixture. These high freezing temperatures may result in freezing of the salt during receiver filling if there is insufficient incoming heat. As the salt starts freezing from the receiver pipe walls inward, it results in a narrowing of the flow area (Lu et al., 2010). This in turn results in a significant increase in pressure loss or even full blocking of the pipe. According to Suárez

et al. (2015), the plant would cease to function if the salt inside the pipes were to freeze shut. To address this problem, trace heating is typically used to preheat the receiver pipes before the salt enters the receiver (Kearney et al., 2003). However, trace heating is expensive and takes time to heat up the receiver pipes.

In this study, cold filling is considered as an alternative to the use of trace heating. Cold filling can be defined as the filling of a receiver that is initially at a temperature below the molten salt freezing temperature. Salt from the thermal energy storage tanks is pumped through the receiver pipes to heat them up. Filling a cold receiver with hot salt may result in partial or full freezing of the salt in the pipes. As a result, it is even more important to be able to accurately predict the molten salt behaviour if cold filling is used compared to preheated filling methods. The advantage of this method is that it can greatly reduce preheating costs. Furthermore, if no preheating is required, the receiver can be filled earlier and operate for longer.

The temperature of the molten salt in the receiver pipes during receiver cold filling is, therefore, of particular interest. For this study, receiver panel cold filling will be investigated under various conditions. It is important to determine the lowest temperature and velocity at which a receiver panel can be filled with minimal risk of freezing to increase the plant's overall efficiency. Further scenarios will also be investigated including a worst-case weather scenario and a pipe size analysis.

1.2 Problem Statement

Trace heating is commonly used to prevent the molten salt in receiver pipes from freezing. In this study, cold filling is investigated as a method to reduce or even eliminate the receiver preheating costs. To successfully implement cold filling, it is important to be able to predict the molten salt characteristics during the filling process under various conditions.

1.3 Objectives

By considering the above problem, the goal of this study is to produce a reliable numerical model of the physical problem. The results obtained from this model can be used in future to reduce receiver preheating costs during filling and increase the receiver's operating time by employing cold filling. The model can also be used to conduct initial receiver design. This goal will be achieved by completing the following objectives:

1) Selecting an appropriate modelling platform
2) Developing a model than can be used to investigate the molten salt characteristics under various conditions
3) Verify and validate the model
4) Determining the molten salt response under various conditions

CHAPTER 2: LITERATURE STUDY

2.1 Commercial Molten Salt Mixtures

Molten salts have high freezing points ranging from 120 to 220 °C. As noted by Kearney et al. (2003), this introduces the problem of the salt freezing inside the receiver pipes, which could be disastrous; especially if the salt freezes in some of the larger pipes. To counteract this, freeze protection is required. When the freeze protection is implemented using auxiliary heating, Biencinto et al. (2014) found that a plant using molten salt will use up to five times more fossil fuel for auxiliary heating purposes than an equivalent thermal oil plant. This comparison is not necessarily a valid one since molten salt is almost exclusively used as a HTF in central receiver plants, while thermal oil is almost exclusively used as a HTF in parabolic trough plants. The point does, however, remain that CSP plants that use molten salt as their HTF have high preheating costs due to the high freezing temperatures of these salt mixtures. Steps should therefore be taken to reduce or eliminate the need for auxiliary heating in central receiver plants. The most basic step would be to choose the most appropriate salt mixture for the system.

Commercially available salt mixtures include fluoride mixtures, chloride mixtures and nitrate mixtures. Nitrate salts are preferred over the other mixtures for use in solar thermal power plants because of their favourable properties (Kearney et al., 2003). Nitrate salts have relatively low corrosion rates when coming into contact with standard piping materials, have low vapour pressures, are thermally stable in the operating range required by CSP plants, are widely available and are relatively inexpensive when compared with other salts (Kearney et al., 2003). This statement is further supported by the study conducted by Heller (2013), in which he states that molten nitrate salt has always been used as a HTF in central receiver systems from the Molten Salt Electric Experiment (MSEE); the first solar-to-electrical central receiver system that used molten salt as a HTF, to the Gemasolar plant, which was arguably the most advanced CSP plant at the time.

Based on a review of the available literature, the leading candidates among the nitrate salts are Solar Salt and Hitec^{TM} salt as these are the ones most commonly used in commercial plants and are also most frequently investigated (Suárez et al., 2015; Lu et al., 2010; Serrano-López et al., 2013; Ferri et al., 2008; Lu et al., 2013; Kearney et al., 2003). Kearney et al. (2003) and Ferri et al. (2008) note that Solar Salt is a binary salt consisting of 60 wt % $NaNO_3$ and 40 wt % KNO_3. Kearney et al. (2003) as well as Yang & Garimella (2013) note that Hitec^{TM} is a ternary salt consisting of 53 wt % KNO_3, 40 wt % $NaNO_2$ and 7 wt % $NaNO_3$.

Table 2.1 and Table 2.2 show some of the properties of these two nitrate salts.

Table 2.1: Characteristics of nitrate salts (Kearney et al., 2003)

Property	Solar Salt	Hitec™
Freezing point (°C)	220	142
Upper temperature (°C)	600	535
Density @ 300 °C (kg/m^3)	1899	1640
Viscosity @ 300 °C (cp)	3.26	3.16
Heat capacity @ 300 °C (J/kg.K)	1495	1560

Table 2.2: Effective storage medium cost (Kearney et al., 2003)

Salt Mixture	Temperature Rise (°C)	Cost per kg ($/kg)	Storage Cost ($/kWh$_{th}$)
Hitec™	200	0.93	10.7
Solar Salt	200	0.49	5.8

Solar Salt has the highest upper operating temperature at 600 °C, as seen in Table 2.1, and is significantly less expensive than Hitec™ salt, as seen in Table 2.2. It is, however, important to note that Solar Salt also has the highest freezing point at 220 °C, as seen in Table 2.1. This is much higher than that of Hitec™ salt, which is a challenge that needs to be overcome when using Solar Salt as a HTF. Kearney et al. (2003) therefore recommends using Hitec™ salt when molten salt is used for both the HTF and storage in parabolic trough plants. Solar Salt, however, would likely be a better option, if freezing in the receiver panels can be avoided, as a higher operating temperature will increase the efficiency of the Rankine cycle.

As discussed by Yang and Garimella (2013), molten salt's physical properties vary with temperature. It is therefore important to find or develop functions to determine these properties before attempting to solve any problem requiring them. Biencinto et al. (2014) used Solar Salt in their simulation and assigned constant values for the density, specific heat and thermal conductivity of the Solar Salt given as: 1823 kg/m^3, 1515 J/kg K and 0.52 W/m K respectively. Ferri et al. (2008) used the Solar Salt property functions defined in Table 2.3. Although not explicitly stated, they likely got these properties from the RELAP5 code they used since these are the properties documented in Sloan et al. (1994); the RELAP5 code manual.

Table 2.3: Solar Salt properties (Ferri et al., 2008)

Property	Function
ρ (kg/m^3)	$2090 - 0.636(T - 273.15)$
c_p (J/kg.K)	$1443 + 0.172(T - 273.15)$
μ (kg/m.s)	$0.022714(T - 273.15) + 2.281 \times 10^{-7}(T - 273.15)^2$ $-1.474 \times 10^{-10}(T - 273.15)^3$
k (W/m.K)	$0.443 + 0.00019T$

Where ρ is density, c_p is specific heat, μ is dynamic viscosity, k is thermal conductivity and T is the molten salt temperature given in Kelvin in this case. Note that the number of significant figures given in Table 2.3 is not consistent. The higher order terms with fewer significant figures therefore lose accuracy, which diminishes some of the lower order terms' accuracy.

Wu et al. (2012) measured the density, specific heat, thermal conductivity and viscosity of Hitec™ salt. Their findings are summarised in Table 2.4 with the molten salt temperature given in Kelvin.

Table 2.4: Hitec™ salt properties (Wu et al., 2012)

Property	Equation	Validity Range
ρ (kg/m^3)	$2083.5 - 0.748(T - 273.15)$	$493\ K < T < 773\ K$
c_p (kJ/kg K)	1.424	$493\ K < T < 773\ K$
μ (kg/m s)	$0.0017 - 0.2149\mathrm{e}^{-(T-273.15)/57.05}$	$493\ K < T < 773\ K$
k (W/m K)	$0.586 - 0.00064(T - 273.15)$	$573\ K < T < 773\ K$

Santini et al. (1984) conducted a study in which they measured the thermal conductivity of three pure molten salts as well as Hitec™ salt within the range of 100 °C to 500 °C. They proposed the polynomial property function given by equation (2.1) to determine the thermal conductivity of Hitec™ salt. The temperature in equation (2.1) is given in Kelvin.

$$k = 0.78 - 1.25 \times 10^{-3}T + 1.6 \times 10^{-6}T^2 \quad (2.1)$$

Many authors such as Janz & Tomkins (1980) have experimentally determined the properties of a large number of molten salts under various conditions and formulated property functions for these salts. Serrano-López et al. (2013) conducted a review of a large number of studies prior to 2013 aiming to determine the density, specific heat, dynamic viscosity and thermal conductivity property functions for various pure molten salts and common molten salt mixtures. Density correlations for Solar Salt and Hitec™ salt from different studies were generally found to correspond well, following similar trends with little variation (Serrano-López et al., 2013). The specific heat property functions derived for these salts are not as congruent. Some studies found that specific heat decreases with temperature, some studies found that it remains nearly constant and other studies found that it increases with temperature (Serrano-López et al., 2013). For Solar Salt, a negligible difference was found between the dynamic viscosities with respect to temperature as determined by several studies (Serrano-López et al., 2013). As for the thermal conductivity of Solar Salt and Hitec™ salt, the property functions obtained in various studies again followed both increasing and decreasing trends, while some studies determined that thermal conductivity remains constant as temperature increases (Serrano-López et al., 2013). Clearly, large uncertainty regarding the input data used to generate the molten salt property functions is present. Serrano-López et al. (2013) compared previous studies and suggested the best correlation for each salt

mixture. The suggested property functions for Solar Salt are summarised in Table 2.5, with all temperatures given in Kelvin.

Table 2.5: Solar Salt properties - global review (Serrano-López et al., 2013)

Property	Equation
ρ (kg/m^3)	$2263.641 - 0.636T$
c_p (kJ/kg K)	$1396.044 + 0.172T$
μ (kg/m s)	$0.075439 - 2.77 \times 10^{-4}(T - 273.15) + 3.49 \times 10^{-7}$ $(T - 273.15)^2 - 1.474 \times 10^{-10}(T - 273.15)^3$
k (W/m K)	0.45

The property functions that Serrano-López et al. (2013) suggests for Hitec™ salt is summarised in Table 2.6, with the molten salt temperature given in Kelvin.

Table 2.6: Hitec™ salt properties - global review (Serrano-López et al., 2013)

Property	Equation
ρ (kg/m^3)	$2279.799 - 0.7324T$
c_p (kJ/kg K)	1560
μ (kg/m s)	$e^{\{-4.343-2.0143[\ln(T-273.15)-5.011]\}}$
k (W/m K)	0.48

Based on the Serrano-López et al. (2013) research methodology, the fact that their study is recent and that it is a review of many sources, the suggestions given in Table 2.5 and Table 2.6 are more dependable that those given in other studies. It is important to note, however, that care should be taken when selecting property functions for which high deviations in results have been obtained. For this study, the suggestions made by Serrano-López et al. (2013) were further compared to other studies, as seen in Section 4.3.1, and based on these results, appropriate property functions were chosen.

There will likely be a change in density between the freezing and melting temperatures of the salt. This change is not described by any of the density property functions reviewed and as a result a shared density between phases was assumed by authors in most studies similar to this one, for example Xu et al. (2017). The effects of this change should be investigated in future studies.

As determined by Lu et al. (2013), when the salt starts to freeze or melt, the solid-liquid two-phase zone can be described by equation (2.2) and (2.3).

$$f_l = \begin{cases} 1 & for\ T > T_l \\ (T - T_s)/(T_l - T_s) & for\ T_s \leq T \leq T_l \\ 0 & for\ T < T_s \end{cases} \tag{2.2}$$

$$f_S = 1 - f_l \tag{2.3}$$

Where f_l and f_S denote the content of the liquid and solid phases in the two-phase molten salt zone.

2.2 Central Receiver Plant

This section provides a brief overview of

- What its advantages are as a CSP technology
- How a central receiver plant works
- Which of their components are typically modelled
- Of which materials these components are typically made

2.2.1 Overview

Central receiver plants have several advantages over other CSP technologies. Ortega et al. (2008) as well as El Hefni & Soler (2015) note that central receiver plants operate at the highest efficiencies of all the current commercially active CSP plants. Central receiver plants also have the highest capacity molten salt thermal storage potential (Ortega et al., 2008). This results in the plant being able to produce dispatchable power[1]. Furthermore, Ortega et al. (2008) states that central receiver plants require the least amount of land for power production. It is also less important to level the land that a central receiver plant is built on, compared to what is required for a parabolic trough plant. According to Ortega et al. (2008) these advantages result in central receiver plants having the lowest cost per kWh_e produced of all commercially active CSP plants.

A schematic of a typical central receiver plant can be seen in Figure 2.1. The flow directions as well as the hot and cold temperatures of the molten salt in the loop are also displayed.

[1] Dispatchable power is electricity that can be supplied to the grid as the grid demands it.

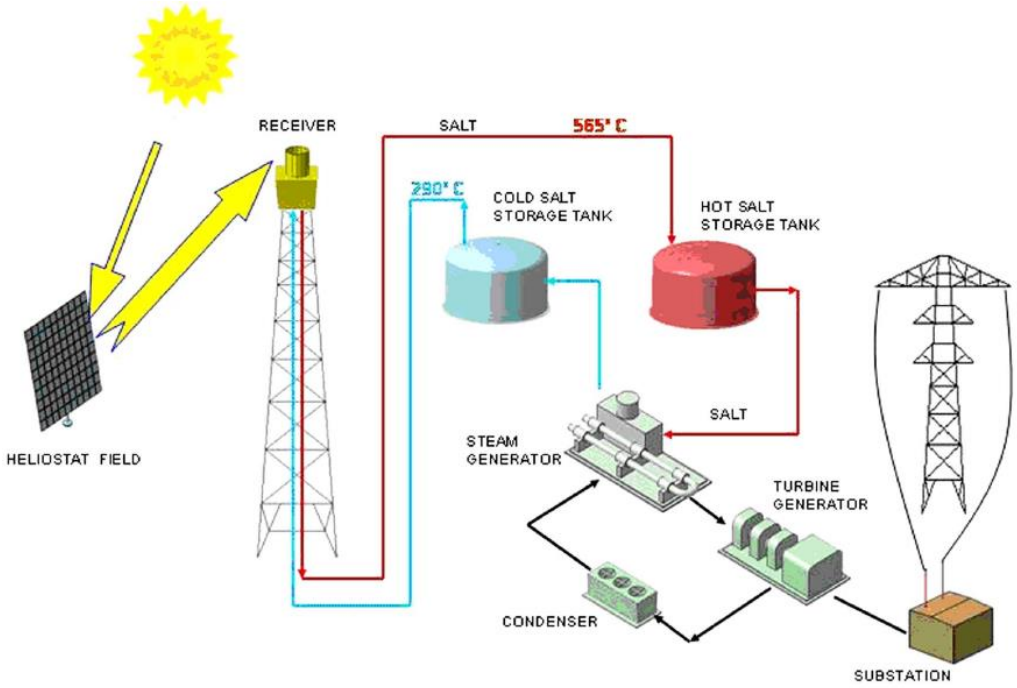

Figure 2.1: Central receiver plant schematic (Ortega et al., 2008)

As seen in Figure 2.1, the molten salt is heated in the receiver, which is the plant component that is the focus of this study, by solar irradiance reflected onto the receiver from the heliostat field. The heated molten salt then flows through the hot salt storage tank and into the steam generator. Depending on the current solar availability and energy demand, the hot salt tank is either filled with more molten salt or supplies molten salt to the steam generator. The molten salt temperature drops in the steam generator, as some of the heat from the molten salt is used to convert water into steam, and is pumped back to the cold storage tank. In the steam cycle, the hot molten salt in the steam generator superheats the water. This steam then drives a turbine to produce electricity. After passing through the turbine, the water and steam is cooled by a condenser before re-entering the steam generator. The steam generator, turbine and condenser are typically comprised of a number of components. Several alternatives to the plant layout shown in Figure 2.1 exist, but the basic principles of how electricity is produced in a central receiver plant are shown.

2.2.2 Components

Depending on the research objectives and methodology, varying levels of detail need to be included when modelling a CSP plant. A variety of different approaches can be found in available literature.

El Hefni & Soler (2015) and Manenti & Ravaghi-Ardebili (2013) performed dynamic simulations relating to the operating strategies of two different CSP plants. El Hefni and Soler (2015) included an economizer, evaporator, superheater, tank, air-cooled condenser, turbines, feed water heaters, pumps, valves and pipes in their water/steam cycle and a solar receiver, as well as hot

and cold molten salt storage tanks. Manenti and Ravaghi-Ardebili (2013) included pumps, valves, hot and cold storage tanks, and a steam generator line that consists of two superheaters, a boiler and an economizer. For their purposes, Manenti and Ravaghi-Ardebili (2013) did not need to include the solar receiver or the remainder of the water steam cycle.

Doupis et al. (2016) as well as Falchetta & Rossi (2014) performed transient drainage simulations on two different CSP plants. To simulate normal circulation, draining and filling operations, Doupis et al. (2016) modelled inlet and outlet tanks, headers, unheated piping, heated tubing, valves and tank vent valves. Falchetta and Rossi (2014) modelled a parabolic trough plant, which, unlike a central receiver plant, has thermal oil cycling through the solar field. For this reason, they chose to include the solar field, comprised of solar collectors, receivers, input and output valves, passive connections and distributing piping, into their model. Falchetta and Rossi (2014) built two models, one for normal operation and one for drainage operation. For the draining model, they included additional draining valves and air vent valves.

For the current study, the modelling scope is limited to a single pipe in the receiver panel. The effects of other components may be taken into account, but will not be explicitly modelled.

In addition to selecting appropriate components to model, the correct materials should also be used to model the various components with. Although the nitrate salts discussed in Section 2.1 are not as corrosive as most other salts, they still contain impurities (Kearney et al., 2003). Kearney et al. (2003) suggests A335 ferritic steel for pipes exposed to peak temperatures higher than 450 °C. Yang et al. (2012) suggests using Inconel 625, a Nickel-Chromium alloy, for the heat transfer pipes in the central receiver due to its high strength, excellent manufacturability and its strong corrosion resistance. According to Yang et al. (2012), Inconel 625 has a thermal conductivity of 16.3 W/m K, a specific heat capacity of 505 J/kg K and a density of 8440 kg/m^3. They do not specify the temperature at which these properties are obtained, but from High Temp Metals (2015) it can be seen that the thermal conductivity was taken at a temperature of about 350 °C and the specific heat capacity was taken at 450 °C. Since the temperature at which these properties were taken does not correspond and the properties do vary with temperature, these values should not be used. From High Temp Metals (2015) it can be seen that the thermal conductivity varies from 9.8 W/m K at 23 °C to 17.6 W/m K at 400 °C and the specific heat varies from 429 J/kg K at 0 °C to 496 J/kg K at 400 °C, which is the approximate range that would be expected for a receiver pipe.

The tower height should be established to know how long the pipes transporting the molten salt in the central receiver should be. According to Terdalkar et al. (2015), a typical central receiver tower height is about 200 meters. The review conducted by Thriumalai et al. (2014) documents tower heights for various central receiver plants. They found that tower heights ranged from 46 m to 200 m. Based on this this review, a typical tower height may be closer to 150 m. If the pipes leading up to the receiver panels at the top of the tower are preheated, the height of the tower may not be important when modelling the

receiver panel, but if these pipes are not preheated to a constant temperature this height is an important consideration.

2.3 Start-up and Shutdown

After studying the existing literature, it became apparent that there is a need to investigate the transient response of CSP plants. El Hefni & Soler (2015) concluded that there is a need to simulate the start-up and shutdowns of CSP plants in future studies. According to Manenti & Ravaghi-Ardebili (2013), there is a need to optimize the start-up and shutdowns of CSP plants to improve the plant's efficiency and safe guard units. An additional reason to investigate the transient response of a CSP plant, rather than being content with a steady state analysis, is the effect that thermal inertia has on the system. Azizian et al. (2011), Wagner & Wittmann (2014) as well as Biencinto et al. (2014) all found that thermal inertia strongly influences the controllability and lifetime of the system and its components. The effect that thermal inertia has on the system is an important factor that is neglected if only a steady state analysis is performed. Employing cold filling will introduce higher thermal stresses in the receiver panels. However, the extent of these thermal stresses falls outside the scope of this study and has already been investigated by several researchers, such as Xu et al. (2017).

2.3.1 Operating Modes

CSP plants function on an intermittent source of energy. Factors including night-time, cloudy or low DNI weather, maintenance and component failure will inevitably result in plant shutdowns. Operating modes and start-up procedures need to be put in place to account for these factors. To be able to improve on the operating modes, the modes that are typically evaluated in literature first have to be investigated.

Azizian et al. (2011) simulate the following five events in their response time study:

1) Plant start-up
2) An out of service collector field
3) Tracking or other collector field problem
4) Cloudy or low DNI weather
5) Changes in operational conditions

Wagner & Wittmann (2014) performed three transient analyses:

1) Transient solar field, stationary power block and auxiliary heating off
2) Transient solar field, standby power block and auxiliary heating off
3) Transient solar field, standby power block and auxiliary heating on

Wagner and Wittmann (2014) suggest pumping the molten salt from the solar field into the hot tank if it is above 485 °C and to the cold tank if it is below 485 °C during start-up and shutdown.

According to Terdalkar et al. (2015) the following operating strategies should be followed:

1) Short or long cloud events are followed by a hot-start
2) Periods of extended shutdown are followed by a cold-start
3) Partial load operation occurs during light cloud events

Doupis et al. (2016) simulated three operations:

1) Normal circulation
2) Draining
3) Filling

Doupis et al. (2016) performed the above operations for three scenarios:

1) Warm restart due to daily start-up and shut down
2) Hot restart scenarios for condition 1
3) Hot restart scenarios for condition 2

The main difference between condition 1 and condition 2 is the system's response to two different cloud events. For condition 1 the receiver is drained during 0 % load condition, while for condition 2 the molten salt is circulated at 90 % of the nominal flow rate to prevent freezing.

Kearney et al. (2003) consider two freeze protection operations:

1) The HTF is circulated at a low flow rate during night time to prevent pipe cooling
2) If the HTF falls below its critical value, the auxiliary heating switches on to prevent the HTF from freezing

From these two scenarios, Kearney et al. (2003) found that the minimum molten salt start-up temperature is 250 °C for a one-hour storage system and 280 °C for a six-hour storage system.

Delameter & Bergan (1986) conducted a review of the MSEE. The receiver can be efficiently operated during cloud events by keeping the receiver warm and thus ready to collect energy (Delameter & Bergan, 1986). According to Delameter & Bergan (1986), this is best achieved by circulating the cold salt through the receiver to keep the receiver warm and the salt from freezing. At some point, however, the pumping costs and thermal losses from the receiver will become too high and this process will no longer be the most efficient operating strategy (Delameter & Bergan, 1986). If this is the case, the molten salt should be drained from the receiver (Delameter & Bergan, 1986). The disadvantage of draining the receiver is that it slows down the start-up process once the cloud event has passed (Delameter & Bergan, 1986).

One thing that all of the above studies have in common is that they all considered start-up and or shutdown scenarios using a systems level approach. This study is different to the above studies in the sense that it will consider receiver start-up at a more detailed component level.

2.3.2 Freeze Protection and Receiver Filling

If the temperature of the molten salt in the pipes drops below its freezing temperature a solidification layer starts to form on the pipe walls (Lu et al., 2010). This solidification layer results in a decrease in the pipe's cross-sectional area, which in turn causes large pressure losses to occur. This loss in pressure will result in a reduced flow rate in the pipe, which in turn accelerates freezing. As a result, these pressure losses can be catastrophic to the system's performance and the component's safety (Lu et al., 2010). It is therefore essential to prevent the molten salt in the pipes from freezing. Several options are available to prevent freezing. As mentioned before, Kearney et al. (2003) suggests circulating the HTF even when the plant is in standby mode. Kearney et al. (2003) also suggests monitoring the molten salt's temperature and activating the auxiliary heating when it drops below its critical value. It is possible to detect the presence of frozen salt using gamma-ray spectrometry and activating the auxiliary heating based on this feedback (Grena et al., 2010).

Kearney et al. (2003) notes that the pipes should be preheated before the filling process can commence. The auxiliary heating can be used to heat the HTF pipes by one of two trace heating methods: impedance heating or resistance heating (Kearney et al., 2003). Kearney et al. (2003) suggests using resistance heating for the piping in the receiver because the resistivity of the piping is comparatively low due to the relatively large thickness of the pipe walls as compared to normal impedance heating applications.

2.3.3 Cold Filling and Receiver Freeze Up

Several authors including Kearney et al. (2003) and Lu et al. (2010) are of the opinion that salt freezing in the receiver tubes would be highly problematic. There are, however, some studies that have been conducted that have concluded that salt freezing in the receiver tubes should be avoided if possible, but that it is not as problematic as thought by authors who claim that it would result in major damage to the plant. If receiver freeze up is in fact not catastrophic, there would be an argument for cold filling of the receiver, which would in turn allow the receiver to be operated more effectively. In this section, previous work relating to cold filling is reviewed.

Delameter & Bergan (1986)

In their review of the MSEE, Delameter & Bergan (1986) noted that an important thawing method was developed when the receiver inadvertently partially froze up. Using only a few heliostats, they were able to thaw the receiver, proving that partial receiver freeze up is not a catastrophic event as was previously believed. Larger sections of pipe, which are not exposed to the heliostats such as the headers, are far more difficult to thaw and so freezing in these sections is still viewed as catastrophic. They demonstrated that cold filling a receiver tube is possible at initial tube temperatures as low as 116 °C and inlet molten salt temperatures as low as 344 °C. The preheating of the receiver tubes can be done using the heliostat field instead of using trace heating (Delameter & Bergan, 1986). The first clear advantage of not requiring trace heating is a reduction in parasitic costs. In addition to this, they found that during the MSEE project, the

trace heating often burned out, which requires considerable effort and time to repair. Since cold filling was demonstrated to be possible and receiver freeze up not to be excessively damaging, they concluded that the molten salt in the receiver can be operated at a temperature much closer to its freezing point than previously thought. This is especially applicable to operation during cloud events and start-up.

Pacheco et al. (1995)

Pacheco et al. (1995) conducted four categories of experiments at the Sandia National Laboratories namely: cold filling, freezing and thawing, component testing and instrumentation testing. They noted that the Martin Marietta molten salt receiver became frozen and was successfully thawed, but that no stress or strain measurements were taken before or after the event. They also noted that in general there is very little data available for the filling of receivers where the receiver pipes have been preheated to a temperature below the molten salt freezing temperature. They found that cold filling could be achieved provided the molten salt flow rate was high enough, but also not so high as to cause the entrapment of air in the salt mixture. An important factor to determine when considering transient freezing in pipes is how far the salt will be able to travel before the pipe freezes shut. This distance is referred to as the penetration distance. Several correlations exist to estimate this distance, but Pacheco et al. (1995) suggests using equation (2.4) as it correlates data from several experiments and can be used for a variety of fluids. For this correlation, constant wall temperature is assumed.

$$\frac{z}{d} = 0.23 Pr^{\frac{1}{2}} Re^{\frac{3}{4}} \left(\frac{\alpha_l}{\alpha_s}\right)^{\frac{1}{9}} \left[\frac{L_h}{Cp_s\,(T_S - T_{wall})}\right]^{\frac{1}{3}} \left[1 + \frac{\gamma\, Cp_m\,(T_0 - T_f)}{h_f}\right] \qquad (2.4)$$

Where d is the pipe diameter, z is the distance to freeze closed, α_l is the thermal diffusivity of the liquid, α_s is the thermal diffusivity of the solid, L_h is the heat of fusion, T_S is the freezing point, T_{wall} is the wall temperature, γ is a parameter used to measure the relative importance of sensible to latent heat and is calibrated to be 0.7 and T_0 is the inlet liquid temperature. This correlation was validated against the results obtained from the MSEE. The results are given in Table 2.7.

Table 2.7: MSEE results and penetration distance correlation results (Pacheco et al., 1995)

Wall Temp (°C)	Salt Temp (°C)	Penetration Distance (m)	MSEE Result
163	371	5.8	Fill OK
116	343	4.2	Fill OK
99	371	4.5	Partially frozen panel

The penetration distance given in Table 2.7 is the penetration distance that Pacheco et al. (1995) calculated using equation (2.4). If the penetration distance is larger than 3.5 m, which is the length of the receiver tube, it means that the fill was successful. The MSEE result indicates the experimental result obtained for

the same conditions as was used for the penetration distance calculation. From these results, it can be seen that the correlation is optimistic since the receiver was partially frozen for the third set of conditions described in Table 2.7, while the correlation predicts that the panel will only become fully frozen after 4.5 m, which is 1 m further along than the length of the receiver tubes. Clearly a more detailed model is required to accurately predict the penetration distance.

From their experiments, Pacheco et al. (1995) concluded that cold filling is feasible, but not required for normal operation. It should rather be reserved for cloud events. Thermal stresses acting on the receiver pipes were found to fall within an acceptable range. Even so, Pacheco et al. (1995) still suggests that valves, flanges and instrumentation should be maintained at a temperature close to that of the molten salt to avoid any excessive thermal shock, which could adversely influence their performance.

Pacheco & Dunkin (1996)

The study performed by Pacheco & Dunkin (1996) is a smaller branch-off study from the study performed by Pacheco et al. (1995). They analysed a molten salt central receiver during periods of receiver freeze up and receiver thawing. They postulate that it is highly likely for a receiver to freeze up at least once during its lifetime. Central receivers have multiple drain valves and each drain valve typically has a one in a thousand chance to fail during draining (Pacheco & Dunkin, 1996). Although a single valve failing is of little consequence, there is a high likelihood that more than one valve will fail at once within the receiver panel lifetime, which could result in the panel failing to drain and then freezing shut (Pacheco & Dunkin, 1996). They were concerned that if the salt in the receiver freezes within a closed section of pipe, such that the whole pipe is filled with frozen salt, the pipes could be damaged or even burst upon thawing since molten salt expands by 4.6 % when melting. Although this is a valid concern and worth investigating, if the molten salt flow rate is low enough, there should be no air entrapment in the salt. As a result, if there is no air to be trapped, the voids will simply be filled with more salt. Due to their concern, they conducted experiments to determine the stress and strain that the receiver pipes are exposed to during thawing. Like Delameter & Bergan (1986), they also used heliostats to thaw the molten salt in the receiver. From their experiments, they found that the heliostats did not thaw all the salt. The heat could not reach the sections of pipe that were insulated (Pacheco & Dunkin, 1996). To thaw these areas, they first had to thaw the rest of the salt and then pump the newly heated salt through the frozen regions. They also suggested installing additional temporary thermocouples or infrared cameras to locate the frozen regions. They ran several scenarios that are documented in Table 2.8.

Table 2.8: Receiver freezing test scenarios (Pacheco & Dunkin, 1996)

Series No.	Freeze First	Freeze Second	Thaw First	Thaw Second
1	Lower	Upper	Lower	Upper
2	Upper	Lower	Lower	Upper
3	Lower	Keep upper hot	Lower	Keep upper hot
4	Upper	Keep lower hot	Upper	Keep lower hot

The four scenarios in Table 2.8 describe the sequence in which the receiver is frozen and thawed. From these experiments, Pacheco & Dunkin (1996) found a maximum strain of over 4 % present in the receiver tubes. They concluded that the way in which the receiver panel froze up and the method used to thaw it determines the severity of the damage caused. Although the freezing in the receiver panel may not break or even severely damage the tubes, it can still take hours to thaw a frozen panel resulting in significant downtime (Pacheco & Dunkin, 1996). Their study seems to suggest that receiver freeze up results in great economic and efficiency losses, but would not require parts to be replaced except for in extreme circumstances. In other words, such an event would be bad, but not catastrophic.

Lu et al. (2010)

Lu et al. (2010) numerically investigated the cold filling of a 2 m section of horizontal pipe with a ternary salt mixture. They modelled the problem in three dimensions. They used their model to evaluate the basic dynamic filling characteristics such as solidification and melting. They also investigated the thermal performance during the filling process by looking at temperature distributions in the salt as well as the heat flux evolution profiles in the pipe wall. They also determined the solidification and melting behaviour of the salt under various inlet conditions. From their simulation results, Lu et al. (2010) made several conclusions. The maximum axis velocity occurs at the maximum solid fraction; provided that the pipe is not frozen shut (Lu et al., 2010). Molten salt boundary heat flux is increased by solidification and decreased by melting (Lu et al., 2010). A higher molten salt inlet temperature reduces the pressure loss in the receiver (Lu et al., 2010). Finally, they found that by increasing the inlet velocity, the flow resistance without solidification increases, but solidification is less likely to occur, which in turn means that the pressure drop over the receiver reaches a maximum at a moderate flow velocity.

Lu et al. (2013)

The model built by Lu et al. (2013) is similar to the model used by Lu et al. (2010). The only difference is that Lu et al. (2010) assumed a constant inlet velocity, while Lu et al. (2013) used a polynomial pumping curve to determine the inlet velocity of the salt. Lu et al. (2013) investigated the same conditions as Lu et al. (2010) did. According to Lu et al. (2013), the inlet temperature greatly affects the filling characteristics. They also note that the inlet velocity decreases with time as the tube is filled and flow resistance increases.

Liao et al. (2014)

Liao et al. (2014) also built a numerical model to investigate cold filling of a 2 m section of pipe with a ternary salt mixture. They changed the pipe direction from horizontal to vertical. Liao et al. (2014) also noted that the problem is an axisymmetric one, which allowed them to model it in two dimensions rather than three. They used their model to determine the effects that changing various parameters has on the receiver pressure drop. They found that the inlet molten salt velocity, inlet molten salt temperature and initial receiver tube temperature have the most significant effects on the system. To prevent freezing, a sufficiently high inlet velocity, molten salt temperature and initial receiver tube temperature should be used (Liao et al., 2014). They also found that the heat transfer

coefficient between the molten salt and the receiver tube has little effect on the receiver pressure drop. Finally, they noted that a high inlet velocity results in a large temperature difference between the inner and outer walls of the receiver tube causing great strain in the tube wall. As a result, inlet velocities that are too high should be avoided. Liao et al. (2014) did not compare this strain in the receiver tube wall to the strain experienced during normal heated operation. This is an important comparison to make to determine the severity of the strain during receiver filling.

Liao et al. (2015)

The model built by Liao et al. (2015) is similar to the model used by Liao et al. (2014). The only differences are the following: Liao et al. (2014) assumed a constant inlet velocity, while Liao et al. (2015) used a polynomial pumping curve to determine the inlet velocity of the salt; Liao et al. (2015) used a binary salt mixture called Solar Salt rather than the ternary salt used by Liao et al. (2014) and they used a 3.5 m pipe rather than a 2 m pipe. Liao et al. (2015) considered three filling modes under three initial receiver tube temperatures. The three modes are successful filling, partial frozen filling and unsuccessful or frozen filling. Liao et al. (2015) simply concluded that the initial receiver tube temperature should be carefully selected and controlled, presumably by trace heating, to prevent receiver freeze-up.

Xu et al. (2017)

Xu et al. (2017) investigated the cold filling of a 3.5 m receiver pipe with Solar Salt. They used a three-dimensional model for the purposes of the finite element analysis (FEA) part of their simulation. They also assumed a constant inlet velocity boundary condition, rather than using a pumping curve to determine the inlet velocity. Xu et al. (2017) ran several simulations to determine the conditions for which successful receiver filling is only just possible. Initial receiver tube temperature from -10 °C to 30 °C were tested with inlet molten salt temperatures ranging from 260 °C to 290 °C (Xu et al., 2017). For each combination, the minimum inlet velocity for which full freezing of the receiver is just avoided was determined (Xu et al., 2017). They concluded that using a higher inlet molten salt velocity allows for a lower inlet molten salt temperature.

From the literature reviewed in this section, it was found that some work has been done on cold filling and receiver freeze up, but more research is required to allow for confident use of this strategy in operating plants. This study aims to recreate some of the work done by the authors in this section using a different modelling approach and then also to address new aspects of the problem. In this study a numerical model, similar to the model built by Xu et al. (2017), is developed to investigate a similar problem.

2.4 Modelling Tools

When building a numerical model of this kind, it is important to select the correct program to model the problem with. The problem can be modelled using a high-level code program such as MATLAB, which includes many predefined functions, but carries significant overheads making it slower than low level coding languages such as C or FORTRAN, which would be alternative options. It can

also be modelled in a more specialised program specifically developed to model flow problems such as ANSYS Fluent.

Pletcher et al. (2012) suggests using FORTRAN, or to a lesser extent, C for computing the conservation equations typical to flow problems. Pletcher et al. (2012) say that FORTRAN is particularly powerful when it comes to solving the Navier-Stokes equations. MATLAB is preferred for solving equations involving small vectors and scalar variables (Pletcher et al., 2012). Based on this information it can be concluded that MATLAB should be avoided when solving systems of large matrices, such as is required when performing a multi-dimensional fluid flow analysis, but should be considered when solving a one-dimensional fluid flow and heat transfer problems for its predefined user-friendly functions. To the author's knowledge, even though MATLAB seems to be an appropriate tool for these one-dimensional fluid flow and heat transfer problems, relatively few researchers have used it when compared to the number of studies conducted using FORTRAN and C. Koo & Kleinstreuer (2003) used a combination of FORTRAN and MATLAB to analyse microfluidic flow effects in micro-channels. They used FORTRAN to do the pre- and post-processing of all large matrices and vectors. They then used MATLAB to solve the resulting set of smaller matrices and vectors.

Several researchers have used MATLAB to model CSP plants. Cardozo (2012) modelled a molten salt central receiver plant using a combination of MATLAB and a MATLAB tool called Simulink. Vergura & Di Fronzo (2012) modelled a parabolic trough plant using MATLAB. DNV.GL (2014) conducted a report for the California Energy Commission in which they used a combination of MATLAB and Simulink to model a CSP plant including its wider integration with the grid, real time market and other energy sources. In each of these cases, Simulink was used to model system level designs, while the MATLAB main script was used to model the more detailed aspects of the plants. It stands to reason that Simulink should be reserved for system level design, while the MATLAB main script should be used when more detail is required.

Azizian et al. (2011) performed a response time analysis on the Shirzas solar power plant; a parabolic trough plant. To do this they used the TRANSYS 16 library and the STEC components library to define the model conditions and select the model components. They then imported the source code from the TRANSYS 16 and STEC libraries into the TRNEDIT environment where editing and reprogramming is possible.

Like Azizian et al. (2011), Biencinto et al. (2014) also used the TRANSYS library to model a parabolic trough plant, with their focus being on the operational strategies used to run these plants. In addition to using the standard TRANSYS library, they also implemented new components using FORTRAN.

El Hefni & Soler (2015) built a dynamic model of a central receiver plant using the ThermoSysPro library, which is open source code developed by EDF. According to El Hefni & Soler (2015), the library can be used for multi-domain modelling, which includes, but is not limited to, thermal-hydraulics, neutronics, combustion, solar radiation, instrumentation and control. They note that the ThermoSysPro

library is especially useful for modelling water/steam, oil and gas systems, but can also be used to model molten salt systems. They state that the most frequently used heat transfer and pressure drop correlations are given by default, but can be edited by the user. They also state that single-phase, mixed, two-phase and separated flow is supported. They prefer this library to some other programs because its two-phase flow is especially well developed, which is a common flow type in CSP plants. They further state that the ThermoSysPro library provides accurate geometrical data for some commonly used heat exchangers. According to them, the ThermoSysPro library only implements the essential constructs of the Modelica language to ensure a high level of compatibility with other tools, modifications and libraries.

Zhang et al. (2015) used Dymola to model a molten salt cavity receiver. Dymola is based on the ThermoSys library that El Hefni and Soler (2015) used. Zhang et al. (2015) also notes that the ThermoSys library is especially good at modelling oil or gas systems, but can be used for molten salt systems. According to Zhang et al. (2015), the ThermoSys library uses first principle mass, momentum and energy balance equations to couple the calculation of the molten salt temperature, velocity and pressure.

Doupis et al. (2016) performed a transient simulation of a central receiver during normal operation, draining and filling using ISAAC Dynamics. They chose this tool based on previous work of a similar nature. The ISAAC Dynamics solver makes use of the Newton-Raphson method to solve a set of equations to a default tolerance of 10^{-5}. They also performed a computational fluid dynamics (CFD) analysis using ANSYS Fluent as well as a FEA.

Falchetta & Rossi (2014) also used ISAAC Dynamics to model a molten salt parabolic trough, with a focus on draining. They noted that ISAAC Dynamics can be used to develop either “models” or “simulators”. Models solve equation sets simultaneously, while simulators run a number of models sequentially without having to solve as many simultaneous equations, assuming the system is decoupled or nearly decoupled.

Wagner & Wittmann (2014) used EBSILON®Professional, developed by Steag Energy Services GmbH, to investigate the influence that different operating strategies have on running a molten salt solar thermal power plant. They used the add-ons EbsSolar and EbsScript to model the solar field and the operation strategies respectively. They analysed the different operating strategies based on the annual plant yield, which they calculated using the EBSILON®Professional time series function.

Zaversky et al. (2013) performed transient simulations of parabolic trough plants with molten salt as a HTF using the Modelica language. According to them, Modelica is a powerful programming language used for multi-purpose physical modelling. They describe Modelica as an amalgamation of several prominent modelling approaches that uses state-of-the-art algorithms to provide the user with exceptional flexibility and functionality. They also note that Modelica is available in both commercial and open-source environments.

Terdalkar et al. (2015) performed a transient analysis of a central receiver for Alstom Power Inc. using the APROS dynamic simulation platform. They chose APROS based on the extensive experience that Alstom has in modelling transient behavior of CSP plants and their components. According to Terdalkar et al. (2015), APROS has not only been validated by Alstom, but also by other recognised companies. They state that APROS has a wide range of capabilities, including being able to account for detailed flow physics, such as solving for two or more coupled flow patterns at once. APROS also has a large component library and strong control modelling capabilities. According to Terdalkar et al. (2015), APROS can also be used to evaluate metal temperature, which is important for systems with long sections of piping in which thermal inertia plays a critical role.

Additional widely accepted CSP modelling tools include the National Renewable Energy Laboratory's (NERL) programs System Advisor Model (SAM) and SolarPILOT. SAM is a free software package open for public use (Wagner et al., 2010; Dobos et al., 2014). According to Dobos et al. (2014), SAM utilises TRANSYS, which Azizian et al. (2011) and Biencinto et al. (2014) used directly. Dobos et al. (2014) also states that the core engineering principals are coded in FORTRAN. The description of SAM given by Wagner et al. (2010) and Dobos et al. (2014) indicates that it is used for system level simulation. SAM returns annual performance, cost and financing results (Blair et al., 2008), but lacks the ability to present short-term transient plant responses. According to the NERL's webpage, SolarPILOT is a heliostat and heliostat field design and optimisation tool (NERL, 2015). The program has the ability to integrate ray-tracing to optimise the solar field cost and performance (NERL, 2015). It cannot, however, be used for transient receiver modelling.

Two of the three numerical models built in the studies discussed in Section 2.3.3, namely the one built by Lu et al. (2010) and Lu et al. (2013) as well as the one built by Liao et al. (2014) and Liao et al. (2015), were developed using ANSYS Fluent. ANSYS Fluent is a powerful CFD program that has been developed over decades. The third of these models, built by Xu et al. (2017), used CFD software developed by EDF called Code_Saturne. Code_Saturne is very similar to ANSYS Fluent in the sense that most of the fluid flow mathematics in these programs overlap. Since the model built in this study is similar to those built in the aforementioned studies, it is clear that these types of CFD programs are appropriate for the problem considered in this study.

Clearly, a wide variety of tools are available with which to model CSP plants or their components. From the literature reviewed in this section, it seems that a CFD program such as ANSYS Fluent might be the best for modelling the type of problem considered in this study. When it comes to understanding the physics behind the problem, however, it is best to use a low-level code such as FOTRAN or C. Although MATLAB is a higher order code, it also requires the user to define their own correlations and thus build their own model from first principals. This approach involves redoing a lot of work that other developers have already done, but it enables the researcher to understand the field better than if they were to use a modelling tool that only requires the correct input values. In this study, high importance is placed on understanding the problem from first principles, which is

why MATLAB was chosen as the program in which to model the problem. Furthermore, the author is already proficient in MATLAB as it forms part of several subjects offered at the University of Stellenbosch.

2.5 Literature Study Conclusion

The literature reviewed in this chapter serves two purposes. The first is to provide the reader with a background to the problem. The second is for it to be used to better understand and define the problem considered in this study.

From Section 2.1 it was seen that it is important to select the best salt mixture for the problem and ensure that the property functions used to describe that salt's behaviour is accurate. It was found that either Solar Salt or Hitec^{TM} salt should be used.

A brief overview of a typical central receiver plant was given in Section 2.2 to sketch the context of the problem considered in this study. Sections 2.3.1 and Section 2.3.2 provide some background into how a central receiver plant is operated, how it is filled and how freezing can be prevented. These sections were included to further describe how this study fits into the bigger picture.

Previous work done on cold filling was discussed in Section 2.3.3 to determine how studies have been conducted in the past and what new work is still required. This greatly aided in defining the problem more precisely as a numerical cold filling simulation of a single receiver tube with Solar Salt or Hitec^{TM} salt. It was also found that wind and rain during the cold filling process has never been taken into account.

Next, a review of available modelling tools was conducted in Section 2.4. It was determined that ANSYS Fluent is probably the best tool for modelling the problem posed in this study. It was decided, however, to rather use MATLAB as the author is already proficient with it and it enables the author to better understand the physics and mathematics behind the problem.

CHAPTER 3: MODELLING THEORY

When modelling a system, it is important to know which methods will be followed. Without this knowledge, it is difficult to know which components to model and how detailed those models should be. The problem under consideration should be well understood before these strategies and methods are selected. This study models a single receiver tube that is to be representative of a whole receiver panel. The molten salt temperature is of particular importance as that is what dictates freezing in the pipe. The model should be able to determine whether the receiver will fill successfully at different operating conditions. Modelling strategies and methods should be chosen based on these problem outlines.

3.1 Pipe Model

Receiver pipes can be modelled as having a hot and a cold side since solar radiation is only incident on one side of the pipe. Doupis et al. (2016) made this assumption in their model as seen in Figure 3.1. This assumption is appropriate when modelling a system being heated by the heliostat field. Such a system cannot be modelled using axis symmetry. When only filling is considered under low or zero DNI conditions, there need not be a distinction between the front and the back of the tube. As a result, the pipe can be modelled using axis symmetry. Doupis et al. (2016) also indicated the various types of radial heat transfer that they included in their model as shown in Figure 3.1.

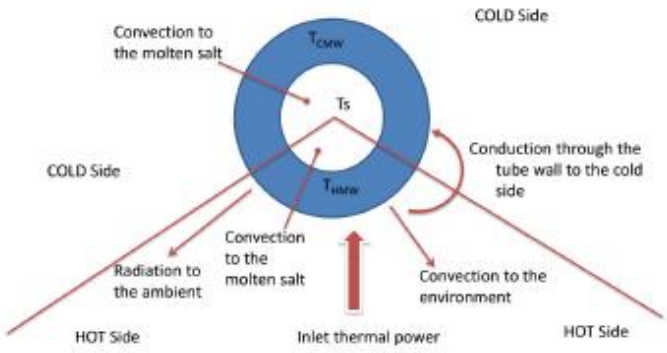

Figure 3.1: Receiver pipe heat transfer assumptions (Doupis et al., 2016)

From Figure 3.1 it can be seen that a simple lumped-mass approach was followed, as only one element was used to model the salt temperature and one element to model the tube temperature in the radial direction. Doupis et al. (2016) deemed the temperature difference between the inside and outside of the tube to be negligible. The back of the cold side is assumed to be well insulated and can therefore be modelled as an adiabatic surface. Convection, radiation and conduction were taken into account in this model. This model will only be applicable to a central receiver with one row of receiver tubes. If multiple rows of receiver tubes are present, the tubes will receive radiation from the tube rows behind them and should therefore not be insulated.

As seen in Figure 3.2, Yang et al. (2012) also assumed that the receiver pipes have hot and cold surfaces. They modelled the heat flux according to the cosine function given by equation (3.1).

$$q(\theta) = q_{net}\ cos(\theta) \tag{3.1}$$

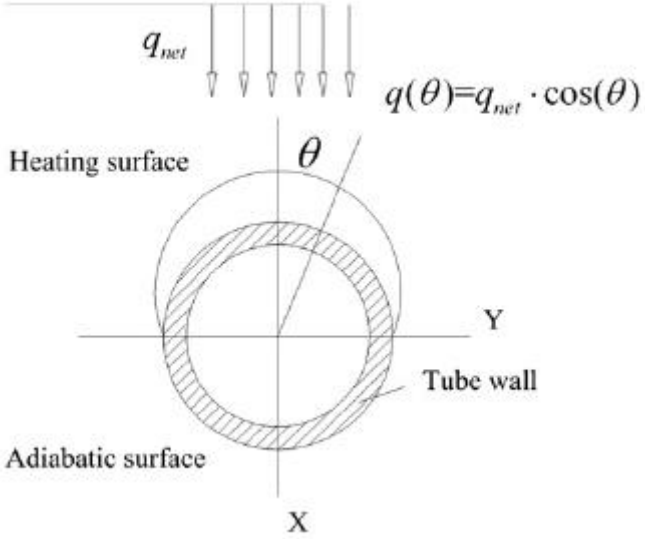

Figure 3.2: Receiver pipe heat flux distribution (Yang et al., 2012)

Zhang et al. (2015) considered three forms of heat transfer, which can be seen in Figure 3.3. These include the thermal conduction in the metal tube, the thermal convection from the outer surface of the tube to its surroundings and the thermal convection from the inner tube surface to the HTF inside the tube. Not shown in Figure 3.3 is the thermal radiation from the outer surface of the pipe to the environment, which Zhang et al. (2015) also included.

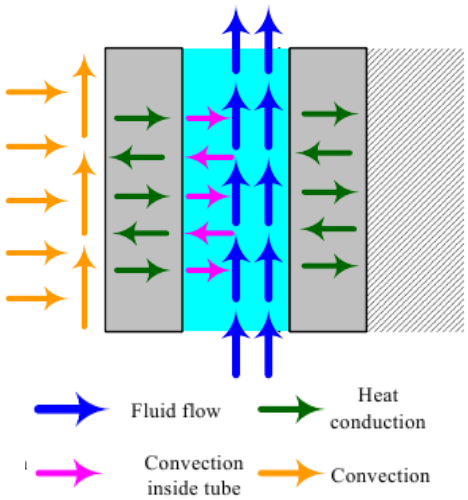

Figure 3.3: Receiver pipe heat transfer and fluid flow schematic (Zhang et al., 2015)

In addition to modelling the heat transfer in and around the pipe, the filling dynamics should also be described. Lu et al. (2013) investigated the filling dynamics of molten salt in a central receiver pipe. In their study, they chose to determine the inlet velocity into the receiver by means of a characteristic pumping curve. Lu et al. (2013) defined the pressure head of the pump, P_{pu}, in equation (3.2).

$$P_{pu} = P_{re} + P_1 \tag{3.2}$$

P_1 is the pressure drop in the initial segment and P_{re} is the pressure drop in the receiver pipe with the sections being defined as shown in Figure 3.4. The initial segment is the section of pipe between the pump outlet and the receiver inlet. Lu et al. (2013) defines the pressure drop in the initial segment in equation (3.3).

$$\mathrm{P_1} = \frac{\mathrm{L_1}}{\mathrm{d}} \frac{\rho_{\mathrm{ms}} \, \mathrm{v_{avg}}^2}{2} \, \mathrm{f} \tag{3.3}$$

Where L_1 is the initial segment length, v_{avg} is the average velocity of the molten salt and f is the McAdams friction factor defined by equation (3.4) as:

$$f = \frac{0.184}{Re^{0.2}} \tag{3.4}$$

If, however, a constant inlet velocity assumption is made, there is no need for equation (3.2) to equation (3.4). This is an assumption made by several authors such as Xu et al. (2017), as discussed in Section 2.3.3.

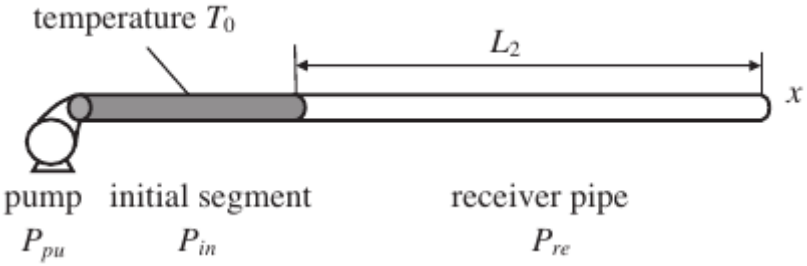

Figure 3.4: Receiver pipe during pumping (Lu et al., 2013)

Lu et al. (2013) also provides a model of the parabolic trough receiver pipe during filling. This is depicted in Figure 3.5.

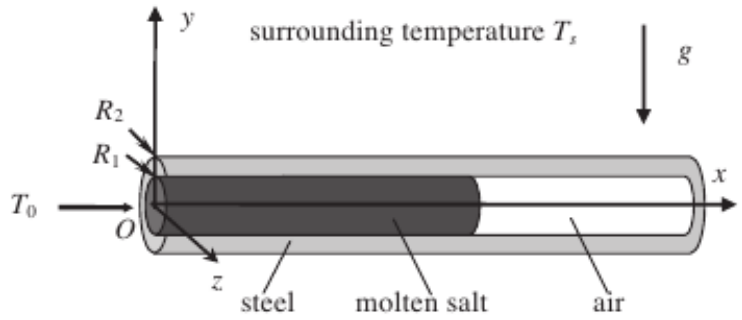

Figure 3.5: Receiver pipe filling process (Lu et al., 2013)

In Figure 3.5 it can be seen that the receiver pipe is initially filled with air before being pumped full of molten salt. The air needs to be vented out of the pipe through air vent valves to make space for the molten salt. Lu et al. (2013) assumes a constant initial segment temperature T_0, which is also the initial molten salt temperature when it enters the receiver pipe as seen in Figure 3.4 and Figure 3.5.

3.2 Heat Transfer Fluid Model

The HTF can be modelled in different ways, depending on the type of study being performed. For studies that focus mainly on the operational aspect of the plant under consideration, such as the studies conducted by El Hefni & Soler (2015) and Biencinto et al. (2014), no two-phase, solidification or crystallization considerations need to be taken into account. For the study performed by Lu et al. (2013), which analyses solidification and filling dynamics, it is important to include two-phase behaviour in the HTF model. The two-phase equations used by these and other authors can be found in Section 2.1.

As is the case for the study performed by Lu et al. (2013), it is important to model the flow of the molten salt as a two-phase flow when considering detail level transient response. Two-phase flow is complex because of a number of factors, namely: it is a three dimensional flow; it is time dependent; the different phases have different material properties; and there is heat, mass and momentum transfer at the phase interfaces. As a result, decisions need to be made regarding how much detail should be included in the modelling process. For one problem it may be important to determine the exact microstructure at every point of the flow, while for another problem a more holistic view of the solid-liquid transition region would be sufficient.

To be able to decide which assumptions can be made and which ones would result in an oversimplification of the problem, two-phase flow must first be understood. Alexiades (1992) decribes much of the two-phase behaviour required for the mathematical modelling of melting and freezing processes. Many materials have a melting temperature which coinsides exactly with its freezing temperature, for some set of conditions (e.g. fixed pressure) (Alexiades, 1992). The phase-transition region where the solid and liquid coexist is referred to as the solid-liquid interface and can range from being only a few Angstroms thick to

being a much thicker region (Alexiades, 1992). This thickness is dependent on several factors, including the material composition, the temperature gradient in the material, the cooling rate, surface tension etc. (Alexiades, 1992). According to Voile & Prakash (1987), if the material in question is not pure, it typically has a separate melting and freezing temperature. If this is the case, the transition region has an apparent thickness and temperature fluctuations occur within this region (Alexiades, 1992). For these materials, the transition region is called the mushy zone (Voile & Prakash, 1987). If a mushy zone exists, the fluid microstructure is typically dendritic or columnar as seen in Figure 3.6 (Alexiades, 1992). In contrast, as discussed before, the numerical studies discussed in Section 2.3.3 models the mushy zone using a macroscopic approach described by equation (2.2) and equation (2.4).

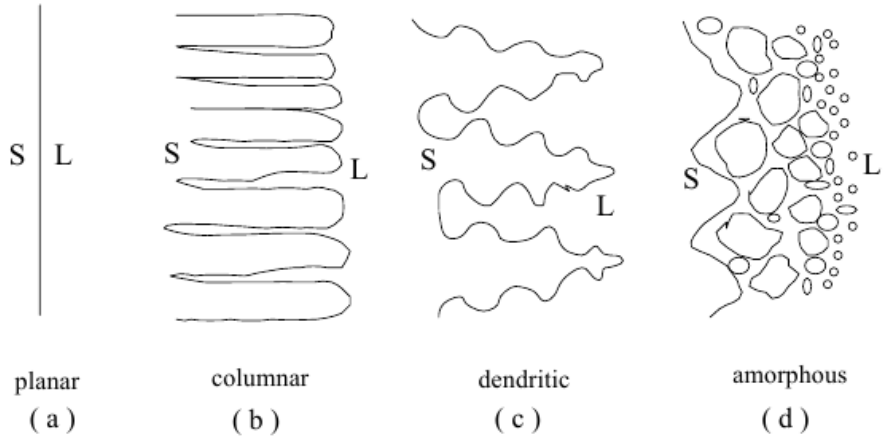

Figure 3.6: Common interface morphologies (Alexiades, 1992)

If determining the microstructure in the mushy zone is important, the Gibbs-Thomson effect should be taken into account. The Gibbs-Thomson effect describes how the local freezing temperature at a curved solid surface in contact with the liquid becomes depressed by an amount dependent on the surface tension that exists between the solid and the liquid as well as the local curvature (Alexiades, 1992). Alexiades (1992) also states that for materials where the solid is denser than the liquid, as is the case with molten salt mixtures, voids are likely to form during freezing and the container that the material is held in may break or be damaged upon melting. This supports the concern posed by Pacheco & Dunkin (1996) that repeated freeze-thaw cycles may damage the receiver tubes.

Alexiades (1992) decribes temperature responses inherent to two-phase flow problems by means of three examples. The first example is that of a molten metal in a cast solidifying where it comes into contact with the cast (Alexiades, 1992). This causes the metal to contract, which breaks the contact between the metal and the cast (Alexiades, 1992). This in turn reduces the cooling effect that the cast has on the metal and may result in remelting (Alexiades, 1992). Similarly, the materials used in latent heat storage, which is used to store solar energy during sunshine hours for use during times when there is no sun, experience many cycles of freezing and melting, resulting in many phase change fronts

(Alexiades, 1992). The last example is that of two ice cubes placed close to one other. If the two ice cubes are close enough, a connecting ice layer will form between them as a result of the local freezing of the water (Alexiades, 1992). It stands to reason that unforeseen temperature fluctuations may occur in complex systems where two-phase behaviour is present. As these fluctuations are often unexpected, it is important to model the system so that it is able to predict these fluctuations and then use the information to prevent equipment damage or better operate the system.

Another decision that needs to be made regarding the modelling of the HTF is whether to model the flow as being one-dimensional, two-dimensional or three-dimensional. The simplest model that is sufficient to describe the problem accurately should be used. The dimensional analysis chosen is highly problem specific. Entrance region flow, for example, is likely to be modelled in two or three dimensions due to the complex profile of the flow. If the flow analysis is occurring further down the pipe where it no longer experiences entrance region effects, a one-dimensional flow analysis might be sufficient. Hibiki & Ishii (2003) states that one-dimensional flow equations might not give a good representation of extreme two-phase flow conditions such as at high flow rates and microgravity conditions, where the wall shear stress can cause a significant difference in relative velocity between the liquid and solid phases. As discussed in Section 3.1, pipes experiencing heating from only one side cannot simply be modelled in one-dimension. For this study, however, the pipe will only be investigated under zero or low DNI scenarios. As a result, a one-dimensional analysis may be sufficient to accurately describe the problem. In the radial direction, the salt may be in one of three states namely, molten salt, solid salt, or a homogenous combination of the two. A one-dimensional analysis should preferably be validated against a higher order dimensional analysis to confirm that the error between the approaches is sufficiently small. If this can be successfully done, a lot of computational effort can be saved.

When modelling longer transient events, it may be advantageous to use adaptive time stepping to better model periods of rapid change. For this model, however, it was decided to use a fixed time step since the transients involved occur over a time period for which changes can be rapid at any point. Choosing the spatial increment can also be approached using two methods. The spatial increment is effectively a mesh, even for the case when it is only a one-dimensional mesh. The one option is to assign a fixed grid mesh to the fluid and pipe. Voile & Prakash (1987) developed a fixed grid numerical modelling methodology to be used for phase change problems in the mushy region. According to Voile & Prakash (1987), a major problem with fixed grids is that, without additional assumptions or methods, it does not allow for the zero velocity condition that occurs when solidification takes place or when the pumping pressure ceases to be sufficient to move the fluid. Several techniques exist to artificially stimulate zero velocity flow. According to Voile & Prakash (1987), these techniques include fixing the velocity to zero when the mean latent heat of a cell reaches a predetermined value close to zero. A more subtle method is to increase the viscosity of the fluid as the velocity decreases (Voile & Prakash, 1987). The high viscosity of the fluid will then simulate the frozen state of the solid (Voile & Prakash, 1987).

The other option is to model the fluid and pipe using a variable mesh. According to Hirt & Nichols (1981), a variable mesh approach can be used to increase the accuracy of a solution in a local area where higher accuracy is required and similarly reduce the accuracy of the solution in local areas where a high accuracy answer is not needed. An example of this advantage from a different field would be to use a fine mesh on an area of high stress and strain and a coarse mesh on areas of low stress and strain. This, however, does not mean that variable meshes are always better. As discussed by Hirt & Nichols (1981), a variable mesh may diverge from the true solution when certain assumptions are made. It is best to use gradual variations in mesh size to increase the accuracy of the mesh and to minimize the reduction in approximation order (Hirt & Nichols, 1981). Based on this information, it is important to use variable meshes with care. Approximations should be tested to ensure that they do not result in diverging solutions.

A decision also needs to be made regarding the heat transfer coefficients that are to be used in the model. The studies considered in Section 2.3.3 assumed constant heat transfer coefficients. In this study, however, it was decided to rather calculate the heat transfer coefficients using generally accepted heat transfer formulae. This should result in an increased accuracy over the temperature range considered.

3.3 Rain Model

Outside of component failure, the worst-case scenario during operation is probably an unexpected downpour of rain coupled with wind. The combined effect of the rain and the wind causes high heat loss from the receiver pipes and may cause the salt to freeze the pipe shut. Extensive work has been done on forced and natural convection due to air flowing over hot cylinders, but to the author's knowledge, no work has been done on simulating the heat loss from hot pipes due to rain. The most closely related subject on which work has been done was found to be spray water-cooling. According to Wendelstorf et al. (2008), spray water cooling is particularly important in the metal production and processing industry. Hot metals of a variety of shapes and sizes are cooled using a cool jet of water (Wendelstorf et al., 2008). Wendelstorf et al. (2008) notes that spray cooling is used to cool internal combustion engines, gas turbines and electronic components used in space technology, to name a few. As the potential applications for spray cooling correlations are quite varied, the heated receiver tubes of a central receiver could fall under the list of items that can be modelled by these spray-cooling correlations.

Jafari (2014) developed an advanced model to predict the spray's interaction with the object it comes into contact with. The model built by Jafari (2014) determines that each individual droplet would interact with the wall in one of four ways: adhesion, rebound, spread or splash. Which of the four possibilities occurs is dependent on the droplet size, temperature and velocity, wall temperature, incident angle, surface roughness, fluid properties and wall film thickness (Jafari, 2014). Jafari (2014) defines the four possibilities as follows:

Adhesion: At low energies, the droplets adhere to the wall in a nearly spherical manner.

Rebound: The droplet does not stick at all and is reflected back after striking the wall.

Spread: The droplet strikes the wall and spreads out creating a localised film on the wall.

Splash: The droplet collides with the wall and then breaks up into smaller droplets. The newly formed smaller droplets rebound, while the rest adhere to the wall.

The Nusselt number used for the heat transfer correlation proposed by Jafari (2014) is given by equation (3.5). The equation is valid for spherical droplets with a droplet Reynolds number of up to 5000. All the other equations required to complete the simulation is documented by Jafari (2014), but their modelling methodology is summarised in Figure 3.7.

$$Nu = 2(1 + 0.3Re_p^{\frac{1}{2}} Pr^{\frac{1}{3}}) \tag{3.5}$$

Where Nu is the Nusselt number, Re_p is the droplet's Reynold's number and Pr is the Prandtl number.

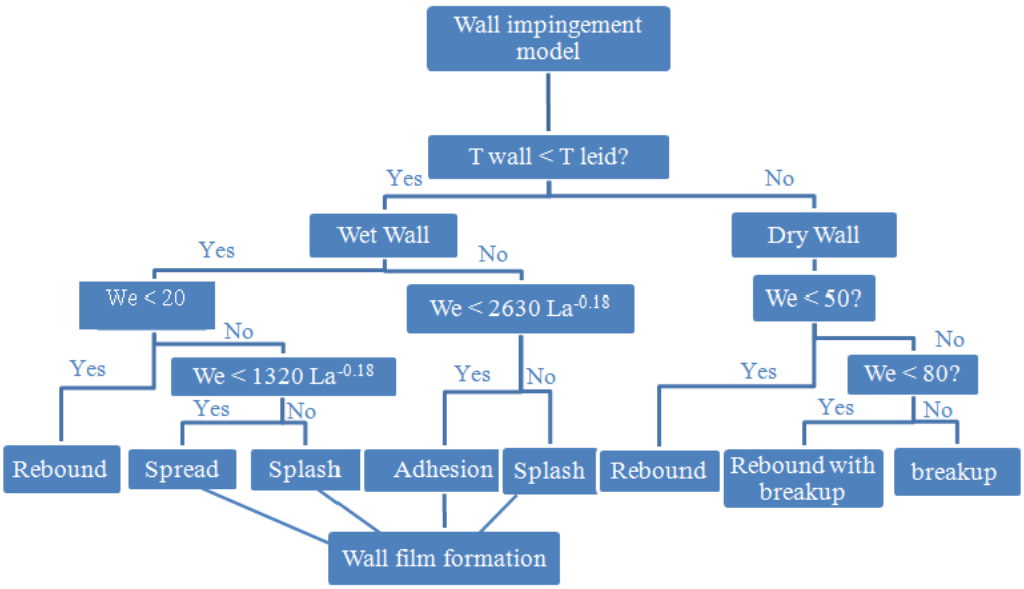

Figure 3.7: Spray-wall impingement regimes (Jafari, 2014)

The methodology followed in Figure 3.7 is too computationally expensive for the resources available to this study, especially if it is only to serve as a small sub-function of a much larger model. It is therefore unlikely that such a complex model will be used to simulate rain on receiver tubes. The advantage in result

accuracy that stands to be gained from using such a complex model is also relatively small when compared to the much simpler models that are available.

In contrast to the detailed single droplet tracking model proposed by Jafari (2014), Wendelstorf et al. (2008) proposed a far simpler model. While the model developed by Jafari (2014) required a large number of input variables, Wendelstorf et al. (2008) believes that only two parameters are essential to describe the heat transfer between the spray water and the object it is colliding with. The primary parameter is the surface temperature and the secondary parameter is the impact density or wetting intensity (Wendelstorf et al., 2008). As the biggest difference between spray water-cooling and rain is the droplet velocity and size, an equation that is dependent on the wetting intensity (which is a function of droplet velocity and size) would be ideal for simulating both spray water-cooling and rain. Wendelstorf et al. (2008) created an analytical correlation from all their experimental data sets. The correlation will be given in Section 4.3.5 by equation (4.69).

Wendelstorf et al. (2008) did not have enough computational power available to run a simulation that evaluates each drop individually. Similarly, depending on the accuracy required and the computational power available, either a more complex model such as the one developed by Jafari (2014), or a simpler model such as the one developed by Wendelstorf et al. (2008) should be used.

CHAPTER 4: MODEL DEVELOPMENT

This chapter delivers a detailed account of how the receiver system is modelled. This includes all methodologies followed, the physical description of the model and all assumptions and limitations present in the model.

4.1 Physical Description of the Model

In this study, several simulations were performed. Two versions of the model were built using two different assumptions. The first is the variable inlet velocity assumption. For this case, the receiver inlet velocity is controlled by a pumping characteristic curve. The second version was built using a constant inlet velocity assumption. The first version of the model was built to validate characteristic curves at certain points. For instance, it was used to validate the molten salt temperature profile versus time at a specific distance along the pipe. This validation was done against the study conducted by Liao et al. (2015). The second version was used to validate the model's response to changes in the system and was validated against the study conducted by Xu et al. (2017). The second model was also used to perform the simulations conducted in this study.

Flood mode filling is a typical method used to fill a multi-pass central receiver panel with molten salt (Liao et al., 2015). A graphical depiction of this filling mode can be seen in Figure 4.1.

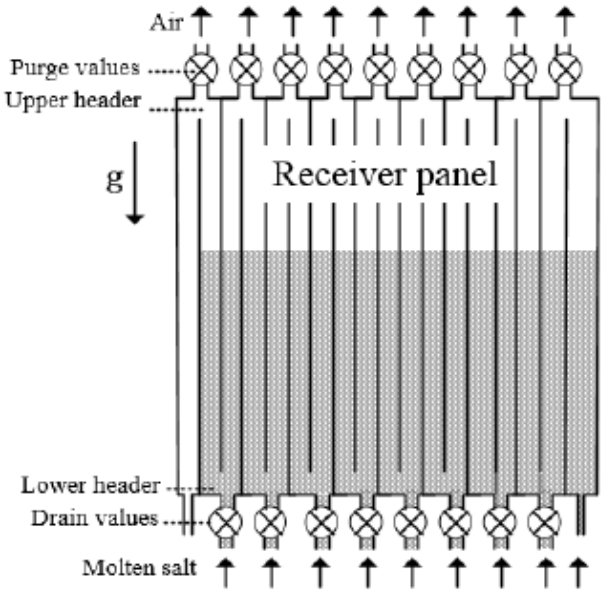

Figure 4.1: Flood mode receiver panel filling (Liao et al., 2015)

The purge valves are opened to allow the air in the receiver to be vented out from the upper header to make space for the molten salt being pumped in from the lower header at the bottom of the panel. Unlike the receiver depicted in Figure 4.1, newer receiver panels have gaps in between the tubes (Falcone, 1986). The older designs had the advantage of preventing 'shine-through' of solar irradiance since there were no gaps in between the panels (Falcone, 1986). This is acceptable for conventional utility plants as the water inside the tubes of these plants boil causing all the tubes to expand at the same rate, but solar power plants experience extensive non-uniform cyclic loading that can result in a range of fatigue failure modes if the tubes have no space to expand and contract (Falcone, 1986). Therefore, the receiver panel tubes will have gaps between them.

For the model built in this study, the receiver 'panel' consists of only one receiver tube. The first validation model also includes a molten salt pump as well as a horizontal section of pipe and a bent section of pipe leading up to the receiver tube. The horizontal section and the bend do not form part of the receiver and thus do not receive heat from the solar field during operation. As a result, these sections will always require trace heating. This setup was chosen to correspond with the study performed by Liao et al. (2015). This model is depicted in Figure 4.2. The second model only models the receiver tube since the constant inlet velocity boundary condition does not require any variable conditions at the tube inlet.

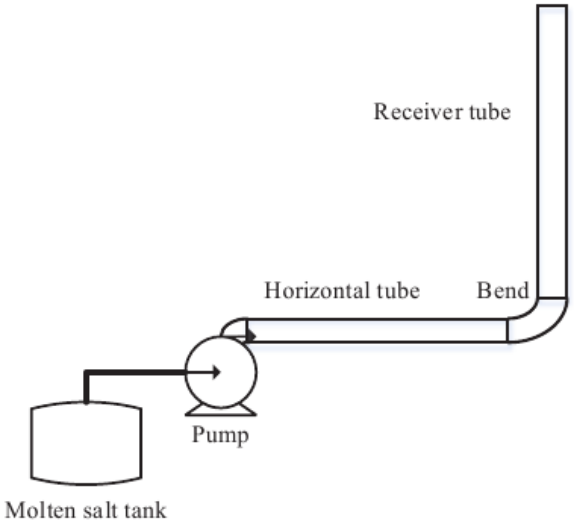

Figure 4.2: First validation model depiction (Liao et al., 2015)

The molten salt tank in Figure 4.2 is only included to help the reader better understand the configuration and is not explicitly modelled. The transient pressure response is tracked, but no temperatures are tracked in the horizontal section of the pipe or in the bend. For this section of pipe, the molten salt and steel tube temperatures are assumed to be accurately controlled by trace heating and only the pressure drop is calculated. For the first validation case model, the horizontal section of pipe is 3.25 m long and the vertical receiver tube is 3.5 m long. The receiver tube, bend and horizontal tube all have the same internal diameter of 15.8 mm and external diameter of 19 mm. The second model has the same receiver tube dimensions.

For both validation cases, 60 % $NaNO_3$-40 % KNO_3 Solar Salt is used, as is the case in the studies performed by Liao et al. (2015) and Xu et al. (2017). The molten salt entering the receiver is taken from the cold molten salt tank at a temperature of 575 K for the first validation case (Liao et al., 2015). In the second validation case, the molten salt enters the receiver at a variety of inlet temperatures and velocities at various initial receiver tube temperatures.

4.2 Modelling Methodology

As discussed in Section 3.2, the problem should be modelled using the simplest method possible, which provides the desired accuracy. For this study, it was decided to model the fluid flow as one-dimensional. This simplification can be made because by the time the molten salt reaches the receiver tube it has already travelled a long distance. By the time the molten salt reaches the receiver tubes, the entrance effects have dissipated. Hibiki & Ishii (2003) states that for cases when no extreme flow conditions are present, such as those that occur in entrance region flow, a one-dimensional flow approximation can be made. They further state that one-dimensional analyses should be avoided for high flow rates. Fortunately, the filling flow rate is relatively slow to prevent air entrapment. During the cold filling process simulated in this study, the receiver tube is not heated by

the solar field. If this were the case, the receiver tube would not experience equal heating effects on all sides. As a result, an axisymmetric model would not sufficiently describe the physics. If this were the case, a one-dimensional model would not be sufficient to model the problem. The receiver tube in this study can, however, be modelled axisymmetrically as no heating effects are considered. All this provides good cause to assume that the one-dimensional flow approximation will hold. If the results can be validated against a higher order model, the assumption that a one-dimensional flow analysis will sufficiently hold and a lot of computational effort can be saved.

Following on the decision to perform a one-dimensional analysis of the problem and considering the review of potential modelling tools discussed in Section 2.4, using MATLAB as a modelling tool seems to be a good choice. The author is already proficient in using MATLAB, which is why it is the preferred choice over FOTRAN or C. MATLAB also has the added advantage of having powerful user-friendly predefined functions that FORTRAN and C do not have.

It is also important to decide how time and distance will be incremented before starting to build the model. When modelling longer transient events, it may be advantageous to use adaptive time stepping to better model periods of rapid change. For this model, however, it was decided to use a fixed time step because the transients involved occur over a time period for which changes can be rapid at any point. For the spatial mesh, there are two choices: a fixed grid mesh or a variable grid mesh. These two mesh types are discussed in Section 3.2. After reviewing the studies conducted by Hirt & Nichols (1981) and Voile & Prakash (1987), the decision was made to use a variable mesh for the first validation case model to overcome the zero fluid flow condition problem that was also discussed in Section 3.2. For this case, the grid size is calculated as a product of the current velocity and time step. When using this approach, it is important to ensure convergence of the results. For the constant inlet velocity model, a fixed mesh approach was followed because the distance moved by the molten salt after each time step would be constant due to the constant inlet velocity.

4.3 Mathematical Modelling of the Receiver

In this section, the mathematics required to model the fluid flow and heat transfer characteristics of the system will be described. This section is divided into five parts. The first part encompasses the discussion and selection of appropriate property functions used to determine the thermal and physical properties of the HTF. The second part describes the sub-function used to calculate the velocity of the molten salt. The pressure drop in the receiver is also calculated in this sub-function. The third, fourth and fifth parts of this section describe the sub-functions used to evaluate the temperatures of the molten salt, the solid salt (when freezing has taken place) and the steel receiver tube. All relevant equations used, assumptions made and derivations required are documented. The relevant sample code is also provided in Appendix B, with the main receiver script given in Appendix B.1.

4.3.1 Property Functions

Two sets of property functions are required to model the system under consideration. The first set is for air. Property functions for air are readily available and little to no variation exists between sources. As has already been established in Section 2.1, Serrano-López et al. (2013) found a general scattering in results obtained from studies conducted to determine the property functions of molten salt. It is therefore important to take great care when selecting molten salt property functions. The following molten salt property functions are required to fully model the system: density, thermal conductivity, specific heat and dynamic viscosity. All other required properties can be derived from these. The property functions scripts for both the molten salt and the air are given in Appendix B.2 and Appendix B.3, respectively.

Density: According to Serrano-López et al. (2013), there is little deviation between the correlations proposed for the density of molten salt. Either the correlation proposed by Serrano-López et al. (2013) or Wu et al. (2012) can be used for Hitec^{TM} salt. These property functions are given by equations (4.1) and (4.2).

$$\rho = 2083.5 - 0.748(T - 273.15) \tag{4.1}$$

$$\rho = 2279.799 - 0.7324T \tag{4.2}$$

The molten salt temperature, T, is in Kelvin for equation (4.1) and equation (4.2). Similarly, the density of Solar Salt can be determined using equation (4.3) proposed by Serrano-López et al. (2013).

$$\rho = 2263.641 - 0.636T \tag{4.3}$$

Where the molten salt temperature is given in Kelvin.

Thermal Conductivity: Property functions for molten salt thermal conductivity vary significantly. Some functions, such as those proposed by Suárez et al. (2015) and Ferri et al. (2008), are linear and increase with respect to temperature, while Wu et al. (2012) found that the thermal conductivity decreases with temperature. Furthermore, Santini et al. (1984) proposes a non-linear function for which thermal conductivity increases with temperature. As a result, Serrano-López et al. (2013) suggests using constant values for the thermal conductivity of both Hitec^{TM} salt and Solar Salt. For this study, Hitec^{TM} salt is assumed to have a constant thermal conductivity of 0.48 W/m.K and the most accurate available Solar Salt thermal conductivity is a constant value of 0.45 W/m.K as suggested by Serrano-López et al. (2013). It is anticipated that conduction will not be as dominant as some other forms of heat transfer. A sensitivity analysis was performed to confirm that this prediction is correct. The thermal conductivity was both increased by 10 % and decreased by 10 %. The resulting error of the molten salt temperature at the receiver outlet after 5 s was found to be 0.18 % for a 10 % increase in thermal conductivity and 0.061 % for a 10 % decrease in thermal conductivity. The error made as a result of this constant thermal conductivity assumption was therefore deemed acceptable.

Specific Heat: Specific heat is another property for which significant variation is recorded. At some temperatures, the error between different specific heat property functions were as large as 23 % for Solar Salt and as large as 46 % for Hitec™ salt. Suárez et al. (2015), Serrano-López et al. (2013) and Ferri et al. (2008) suggest correlations for which the specific heat of Solar Salt linearly increases with temperature. Lu et al. (2013), Wu et al. (2012) and Serrano-López et al. (2013) all suggest assigning a constant specific heat for Hitec™ salt. Although both the linear correlations and the constant values vary between studies, the majority of studies indicate that the specific heat of Hitec™ salt should be described by a constant value and that the specific heat of Solar Salt should be described by a linearly increasing formula. Serrano-López et al. (2013) compared the results of several studies and suggests using an equation that falls in the middle of the range of results to minimise potential error. For this reason, the specific heat property functions proposed by Serrano-López et al. (2013) for both Hitec™ salt and Solar Salt were determined to be the most accurate. The specific heat of Hitec™ salt is 1560 J/kg.K and the specific heat of Solar Salt is given by equation (4.4).

$$c_p = 1396.044 + 0.172T \tag{4.4}$$

Where the molten salt temperature, T, is given in Kelvin.

Dynamic Viscosity: A very large scattering of results has been recorded for the dynamic viscosity of both Solar Salt and Hitec™ salt. Linear, exponential, third order polynomial and logarithmic functions have been proposed for the same property. The deviation between these property functions is large, making it difficult to select an appropriate equation. Correlations proposed by Lu et al. (2013), Wu et al. (2012) and Ferri et al. (2008) were compared to the correlations considered by Serrano-López et al. (2013). From this data set, it was determined that Ferri et al. (2008) proposed the best solution, which results in the least potential error when compared to the other correlations. Ferri et al. (2008) and Serrano-López et al. (2013) both proposed third order polynomial correlations, but the correlation proposed by Serrano-López et al. (2013) seems to lose accuracy at lower temperatures. The property function proposed by Ferri et al. (2008) was determine to be the most accurate and is given by equation (4.5).

$$\mu = 0.022714 - (1.200 \times 10^{-4})(T - 273.15) + (2.281 \times 10^{-7})(T - 273.15)^2 - (1.474 \times 10^{-10})(T - 273.15)^3 \tag{4.5}$$

The correlation suggested by Lu et al. (2013) seems to best describe the dynamic viscosity of Hitec™ salt. This correlation is given by equation (4.6).

$$\mu = 0.01538 - 0.000021T \tag{4.6}$$

The molten salt temperature, T, is in degrees Kelvin for equation (4.5) and equation (4.6).

Although the property functions proposed in this section are considered the most accurate options available, the molten salt properties proposed by Xu et al.

(2017) are used in this study. This is because the current study is validated against their study, which resulted in some confidence being established in these property functions. The proposed property functions suggested in this section are, however, also compared to the property functions used by Xu et al. (2017) to confirm that the property functions used by Xu et al. (2017) is sufficiently accurate. Note that there are some cases in this study for which different property functions were used. In these cases, this will be explicitly stated. The property functions proposed by Xu et al. (2017) are documented in Table 4.1.

Table 4.1: Solar salt properties used in current study (Xu et al. (2017)

Property	Function
ρ (kg/m^3)	2000
c_p (J/kg.K)	1510
μ (kg/m.s)	Equation (4.5)
k (W/m.K)	0.571

4.3.2 Pressure and Velocity Relations

The velocity and pressure sub-function scripts are given in Appendix B.4 and Appendix B.5 respectively. The pumping pressure, the pressure drop in the receiver and the molten salt velocity are all evaluated simultaneously in a system energy balance. To determine these three parameters, the molten salt phase must first be determined. This is done using equation (2.2), as proposed by Lu et al. (2013). The equation is repeated here for convenience.

$$f_l = \begin{cases} 1 \quad for\, T > T_l \\ (T - T_s)/(T_l - T_s) \quad for\, T_s \leq T \leq T_l \\ 0 \quad for \quad T < T_s \end{cases} \tag{2.2}$$

For this study, the Solar Salt liquidus temperature, T_L, is taken as 246 °C and the Solar Salt solidus temperature, T_S, is taken as 221 °C (Archimede, n.d.). According to Liao et al. (2015), the salt initially starts to solidify where it comes into contact with the cooler steel pipes. They also note that for low flow conditions the salt adheres to the insides of the tubes. For these reasons, it is assumed that the salt will start freezing at the internal diameter of the pipe and move uniformly towards the pipe centreline. In actuality, it is far more likely that some of the salt will form clumps, which will be swept along with the flow, re-melt and then freeze again later on in the tube. This is, however, a complicated condition to model, which is expected to add little value to the problem as a whole, especially considering that modelling of this behaviour is not well understood yet. For the purposes for this study, the assumption that the frozen salt will adhere to the tube walls is sufficient. In light of this assumption, the salt liquid fraction, f_l, is used to calculate the effective internal tube diameter, taking into account that some of the tube's internal area may be frozen. This cross-sectional area is then calculated using equation (4.7).

$$A_{cs\_f} = f_l \, \pi \left(\frac{d_{int}}{2}\right)^2 \tag{4.7}$$

A_{cs_f} is the internal cross-sectional area of the pipe, when accounting for freezing, and d_{int} is the internal diameter of the pipe.

Two methods for determining the velocity response through the pipe were used in this study. The first is for the variable inlet velocity assumption, whereby the inlet velocity is controlled by a characteristic pumping curve. The second is for the constant inlet velocity assumption for which there is no change in inlet velocity. For the second method, it will also be proven that no change in velocity occurs throughout the pipe.

First, the method for determining the inlet velocity for the variable inlet velocity assumption case will be described. Since the pumping pressure, receiver pressure drop and molten salt velocity all need to be calculated simultaneously, there are too many unknowns to solve the energy balance. To solve this problem, the velocity is calculated iteratively. An initial guess is made for the molten salt velocity. To ensure that the correct solution is not overlooked, the initial guess is set to a value just above the molten salt initial velocity at time zero. It is safe to assume that the velocity will never exceed this value. For the variable inlet velocity model, the initial inlet molten salt velocity is set to 3.25 m/s. The molten salt mass flow rate is then determined using this velocity and equation (4.8).

$$\dot{m} = \rho_{T_{ms}} \, v \, A_{cs\_f} \tag{4.8}$$

Where T_{ms} is the current molten salt temperature. Next, the Reynolds number is calculated using the standard Reynolds number formula given by equation (4.9).

$$Re = \frac{\frac{\dot{m}}{A_{cs\_f}} \, d_{int}}{\mu_{T_{ms}}} \tag{4.9}$$

The Moody friction factor used by Liao et al. (2015) is also used in this study. The correlation is given by equation (4.10).

$$f = \frac{0.3164}{Re^{0.25}} \tag{4.10}$$

This friction factor, commonly referred to as the Blasius friction factor, is used for fully developed turbulent flow in smooth pipes. The McAdams friction factor, given by equation (3.4), could have also been used, but the Blasius friction factor is used since the study done by Liao et al. (2015) will be used for validation. According to Mills & Ganesan (2015), the turbulent entrance length is typically below five times the pipe diameter for high Prandtl number oils and low Prandtl number liquid metals. Molten salt characteristics typically fall in between those of oil and liquid metal. As a result, it is safe to assume that the same entrance length is applicable. Using this relationship, it was found that the flow will become fully developed at 0.079 m into the pipe. This is a short entrance length compared to the 3.5 m length of the receiver tube. It can therefore be

approximated that the flow in the pipe will always be fully developed. For this study, when the constant inlet velocity assumption is used, the flow will always be turbulent with Reynolds numbers of 10^4 and higher. When the variable inlet velocity assumption is used, however, the flow may approach a zero velocity. For this case, the flow will become laminar and the standard Darcy friction factor of 64/Re is used.

There is, however, a problem in assuming that the pipe is smooth. When salt freezes on the pipe walls, a rough pipe assumption would be a more accurate one, but for the purposes of validation, equation (4.10) will have to be used. The Colebrook-White equation may be a better approximation for the friction factor when freezing takes place. This does, however, require the surface roughness of solid salt. To the author's knowledge, this roughness has not yet been investigated. As a result, the friction factor given in equation (4.10) is used in this study for both the horizontal and vertical sections of pipe. Note that this equation will fail if the Reynolds number is zero. This happens if the molten salt velocity reaches zero either due to a lack of pumping pressure or freezing up of the receiver. To prevent the program from crashing at this point, a small Reynolds number of one is assumed when it is calculated to be zero.

Now the various pressures in the system can be calculated and balanced. During filling, purge valves, such as those seen in Figure 4.1, are opened, which allows the air inside the pipes to be vented out freely. As a result, the air inside the pipes prior to filling causes no back pressure on the rest of the system. Any additional pressure head resulting from the molten salt level inside the storage tank is also neglected, as was the case for the study done by Liao et al. (2015). The pumping pressure for the variable inlet velocity case is the same as that used in the study conducted by Liao et al. (2015). It is a simple characteristic pumping curve that is only a function of the molten salt velocity. The pumping pressure is reflected in equation (4.11) (Liao et al., 2015).

$$P_{pu} = 105000 - 4000v^2 \tag{4.11}$$

The pressure drop in the horizontal section of tubing can be calculated using equation (4.12) (Liao et al., 2015).

$$P_H = f\,\frac{L_H}{2r_i}\frac{\rho_{T_{ms}}\,v^2}{2} \tag{4.12}$$

Where L_H is the length of the horizontal section of pipe and r_i is the internal radius of the pipe. The pressure drop in the pipe bend can also be calculated using equation (4.13).

$$P_B = \xi\,\frac{\rho_{T_{ms}}\,v^2}{2} \tag{4.13}$$

Where ξ is the local pressure loss coefficient. For this system, the local pressure loss coefficient is taken to be 0.29 (Liao et al., 2015). The pressure drop in the receiver is calculated using equation (4.14).

$$P_r = \frac{A_{cs}}{A_{cs_f}} f \frac{L_{re}}{2r_i} \frac{\rho_{T_{ms}} v^2}{2} + \rho_{T_{ms}} g L_{re} + \left[\frac{\left(\rho_{T_{ms}} v A_{cs}\right)_{in}^2}{\rho_{T_{ms}in}} - \frac{\left(\rho_{T_{ms}} v A_{cs}\right)_{out}^2}{\rho_{T_{ms}out}} \right] \quad (4.14)$$

Where L_{re} is the receiver length, g is the gravitational force and the subscripts in and out refer to the flow entering and exiting the current spatial cell. If no subscript is given, it may be assumed that the property is taken at the exit. The first term on the right-hand side of equation (4.14) describes the pressure loss as a result of friction and the second term describes the pressure loss due to the force resulting from the accumulating mass in the column of molten salt. The last terms take into account the pressure loss due to any change in acceleration in the cell. These two terms effectively take into account the pressure drop caused by the narrowing of the pipe's cross section if freezing takes place. Finally, the energy balance can be written in terms of pressure as seen in equation (4.15).

$$P_{pu} = P_H + P_B + P_r + \frac{1}{2}\rho_{T_{ms}} v^2 \quad (4.15)$$

Substituting equations (4.11) to(4.14) into equation (4.15) dividing both sides by v^2 and rearranging to make the molten salt velocity the subject, it is found that the new molten salt velocity is given by equation (4.16).

$$v_{new} = \sqrt{\frac{105000}{b}} \quad (4.16)$$

Where b is given by equation (4.17) as:

$$b = 4000 + f \frac{L_H}{2r_i} \frac{\rho_{T_{ms}}}{2} + \xi \frac{\rho_{T_{ms}}}{2} + \frac{A_{cs}}{A_{cs_f}} f \frac{L_{re}}{2r_i} \frac{\rho_{T_{ms}}}{2} + \frac{\rho_{T_{ms}} g L_{re}}{v^2} + \left[\frac{\left(\rho_{T_{ms}} v A_{cs}\right)_{in}^2}{\rho_{T_{ms}in} v^2} - \frac{\left(\rho_{T_{ms}} A_{cs}\right)_{out}^2}{\rho_{T_{ms}out}} \right] + \frac{1}{2}\rho_{T_{ms}} \quad (4.17)$$

The new velocity is then compared to the initial velocity guess. If the absolute value of the difference between the old and the new velocities divided by the new velocity is less than 0.1 %, the velocities have converged to a sufficiently accurate answer. Through iteration, the value of 0.1 % was found to be sufficiently small to result in accurate convergence consistently. If the velocities have not yet converged, the old velocity is decremented by 0.0001 m/s and the energy balance is solved again. A sufficiently, but not excessively, small decrementing value was determined by trial and error to ensure that the true velocity will always be found while minimizing computational expense. Once the final new velocity is calculated, the final pumping pressure and pressure drop in the receiver can also be calculated using equation (4.11) and equation (4.14) respectively. After some simulations were run, it was found that the velocity of the

molten salt does not always reach zero, instead it reaches a value close to zero. A condition was therefore established saying that if the velocity drops below 0.001 m/s, which is much lower than the initial inlet velocity, it is sufficiently low to be considered zero velocity.

For the case when the constant inlet velocity assumption is made, a simple mass balance can be solved to determine the velocity at any point along the tube. This mass balance can be seen in Figure 4.3.

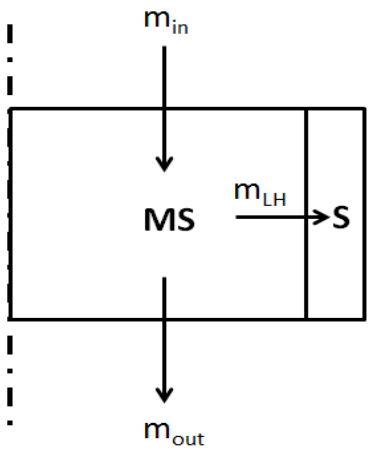

Figure 4.3: System mass balance

When no freezing takes place, the mass coming into the control volume is equal to the mass leaving the control volume. However, when freezing does take place, there is some mass of salt that remains in the control volume as seen in Figure 4.3. If the inlet velocity is constant, for each time step, a fixed mass of new salt needs to enter the pipe. Equation (4.18) is the mass balance for each spatial increment.

$$m_{in} = m_{out} + m_{LH} \tag{4.18}$$

Where m_{LH} is the mass that leaves the flow of molten salt and adheres to the pipe wall as solid salt. Equation (4.18) can be rewritten in terms of a rate of flow as seen in equation (4.19).

$$\dot{V}_{in}\,\rho_{in} = \dot{V}_{out}\,\rho_{out} + \dot{V}_{LH}\,\frac{\rho_{in} + \rho_{out}}{2} \tag{4.19}$$

Where $\dot{V}$ is the molten salt volume flow rate. Equation (4.19) can be further broken down into equation (4.20) so that the velocity at the control volume outlet may be calculated.

$$\begin{aligned} &v_{in}\,A_{cs\_f\_in}\,\rho_{in} = v_{out}\,A_{cs\_f\_out}\,\rho_{out} \\ &+\left(A_{cs\_f\_in} - A_{cs\_f\_out}\right)\,v_{out}\,\frac{\rho_{in} + \rho_{out}}{2} \end{aligned} \tag{4.20}$$

Since the density is constant in this study, equation (4.20) simply reduces to equation (4.21).

$$v_{out} = v_{in} \tag{4.21}$$

The result is that the velocity will be constant throughout the length of the receiver tube when using the constant inlet velocity and constant density assumptions.

4.3.3 Mathematical Model of the Heat Transfer Fluid

By evaluating similar studies and considering the goal of the current study, which deals with the transient evaluation of molten salt, it was determined that modelling the HTF without including two-phase flow would be an oversimplification. It was, however, decided that determining the microstructure and solid-liquid interface morphologies is not required for this problem. According to Alexiades (1992), the microstructure of the mushy zone has little effect on the overall freezing process. It then stands to reason that for the purposes of this study a more holistic view of freezing, such as the view taken by Liao et al. (2015), may be followed.

Sections 4.3.3, 4.3.4 and 4.3.5 describe the sub-functions used to evaluate the temperatures of the molten salt, the solid salt (if freezing has taken place) and the steel receiver tube, respectively. The heat transfer taking place between the three parts of the system is depicted in Figure 4.4 for the case when freezing takes place.

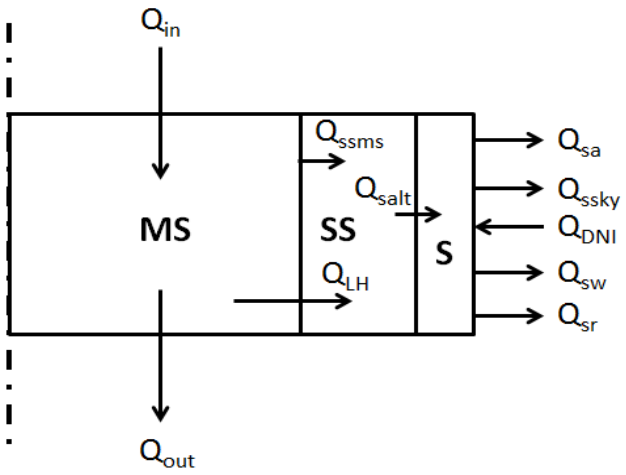

Figure 4.4: System heat transfer - with freezing

As seen in Figure 4.4, the receiver system is broken up into three parts, namely: the molten salt (MS); the solid salt (SS); and the steel receiver tube (S) for the case when freezing has taken place. If no freezing has taken place, the heat transfer is depicted by Figure 4.5.

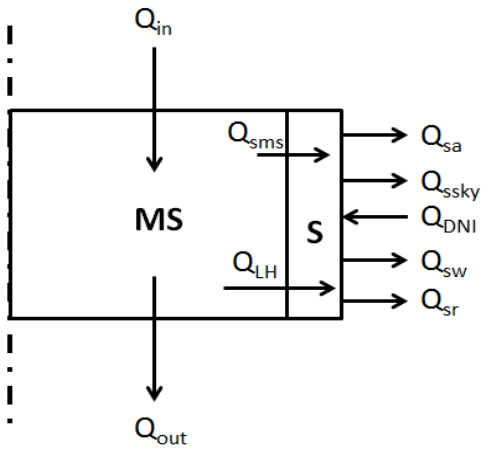

Figure 4.5: System heat transfer - without freezing

The receiver system is broken up into two parts when freezing has not occurred, as seen in Figure 4.5. The dashed lines indicates the centreline of the pipe, Q_{in} and Q_{out} is the heat transfer into and out of the control volume due to the flow of molten salt, Q_{LH} is the energy transfer due to a change in phase of the salt (this is zero when no phase change occurs), Q_{sa} is the heat transfer from the receiver tube to the air, Q_{ssky} is the radiation heat transfer from the receiver tube to the sky and surroundings, Q_{DNI} is the heat transfer from the heliostat field onto the receiver, Q_{sw} is the heat transfer from the receiver tube as a result of wind and Q_{sr} is the heat transfer from the receiver tube as a result of rain. Q_{ssms} is the heat transfer from the molten salt to the solid salt, Q_{sms} is the heat transfer from the molten salt to the steel receiver tube and Q_{salt} is the heat transfer from the solid salt to the steel. These parts are split up to determine each part's initial energy balance.

The first of the three parts seen in Figure 4.4 is the molten salt or HTF part. This part is isolated and depicted in Figure 4.6. The MATLAB script written for this part is given in Appendix B.6.

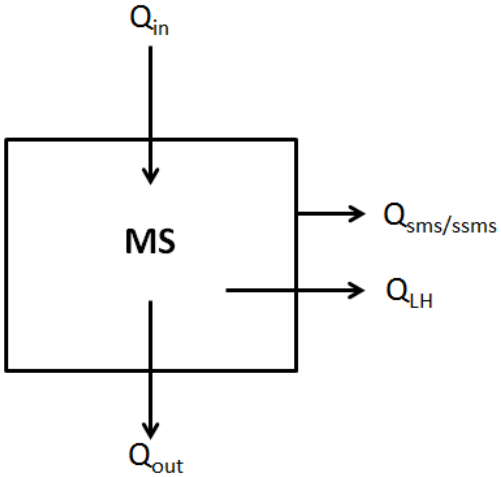

Figure 4.6: Molten salt heat transfer

As seen in Figure 4.6, four modes of heat transfer are taken into account for this part of the system. Q_{in} and Q_{out} are called the flow terms. These are the terms that transport heat into and out of the control volume by means of the molten salt flowing into and out of the cell. There will then either be a term Q_{sms} or a term Q_{ssms} present. If a layer of salt exists between the molten salt and the steel tube at the moment of analysis, Q_{ssms} will describe the heat transfer between the molten salt and the solid salt layer. If, however, no salt layer has formed, Q_{sms} describes the heat transfer between the molten salt and the steel receiver tube. Finally, Q_{LH} takes into account the energy gained or lost by the control volume due to a phase change of the salt. This term will only be non-zero if freezing has taken place or is about to take place. The value of Q_{LH} can either be positive or negative depending on whether latent stored energy is being released into the control volume causing a larger temperature change or whether latent energy is being stored and therefore results in a decreased temperature change. To write the initial energy balance of the molten salt block, each of the heat transfer terms need to be defined and calculated.

As with the pressure and velocity calculations discussed in Section 4.3.2, the initial step for calculating the new molten salt temperature is to determine the current phase of the molten salt and the corresponding effective internal tube area. Equation (2.2) and equation (2.4) are again used to determine the liquid fraction and equation (4.7) to determine the effective internal area of the pipe. For further details relating to these calculations refer to Section 4.3.2. If the liquid fraction is less than one, a solid salt layer has started to form on the inner wall of the receiver tube. In this case, a frozen salt layer sub function is introduced as is described in Section 4.3.4.

The only difference that the molten salt experiences between having and not having the solid salt layer is that the solid salt has a much rougher surface than the receiver pipe. As a result, the Colebrook-White equation should be used to calculate the friction factor when freezing takes place, rather than the Blasius friction factor equation given in equation (4.10). However, the surface roughness of the solid salt is unknown. This first needs to be investigated before the Colebrook-White equation can be used. As a result, equation (4.10) is used for both smooth and rough pipe conditions. Therefore, the fluid flow and heat transfer equations required to calculate the heat transfer between the molten salt and either the steel tube or the solid salt layer are similar. The heat transfer coefficient between the molten salt and the steel receiver tube or solid salt layer, $Q_{sms/ssms}$ seen in Figure 4.6, can be calculated. To do this the molten salt mass flow rate, Reynolds number and molten salt to steel receiver tube friction factor has to be calculated. This is done using equations (4.8), (4.9) and (4.10), as was the case for the pressure and velocity calculations. The Prandtl number of the molten salt can also be calculated from its definition using three of the existing property functions. The formula used to calculate the Prandtl number is given by equation (4.22).

$$Pr = \frac{c_p(T_{ms})\,\mu(T_{ms})}{k(T_{ms})} \tag{4.22}$$

According to Mills & Ganesan (2015), the Nusselt number for fully developed forced flow in tubes and ducts for Reynolds number between 1500 and 10^6 is accurately represented by equation (4.23).

$$Nu = \frac{\left(\frac{f}{8}\right)(Re - 1000)\,Pr}{1 + 12.7\left(\frac{f}{8}\right)^{\frac{1}{2}}\left(Pr^{\frac{2}{3}} - 1\right)} \tag{4.23}$$

It is expected that the Reynolds number will never exceed the upper limit of equation (4.23). It is, however, likely that the Reynolds number will drop below the lower limit of equation (4.23) when the molten salt velocity approaches zero. When this is the case and the Reynolds number drops below 1500, White & Corfield (2006) proposes an alternative correlation for determining the Nusselt number. This correlation is given by equations (4.24) and (4.25) and is valid for laminar incompressible flow in pipes.

$$x^* = \frac{L_r}{d_{int}\,Re\,Pr} \tag{4.24}$$

$$Nu = 1.076\,x^{*-\frac{1}{3}} - 1.064 \tag{4.25}$$

If either the correlations proposed by Mills & Ganesan (2015) or White & Corfield (2006) yields a result below 4.363, Mills & Ganesan (2015) suggests using a Nusselt number of 4.363, which has analytically been determined to be the lower Nusselt number limit for thermally fully developed flow with constant heat flux. Although the heat flux from the inside of the tube is not constant, the heat flux from the outside is close to constant when taking into account that the temperature differential between the wind, rain and air, and the tube wall temperature varies only marginally relative to the size of this temperature differential. The constant wall temperature condition is a worse approximation, as the tube wall starts at a temperature as low as ambient and then heats to hundreds of degrees Celsius. In this study, the constant heat flux assumption is, therefore, preferred over the constant wall temperature assumption whenever the Nusselt number falls below 4.363. Note that a constant heat flux on the system is never assumed, as a temperature differential will always be used to calculate the heat loss to the environment. It is simply a constant heat flux assumption that is used to calculate the lower limit Nusselt number of 4.363. This Nusselt number is then further used to calculate the variable heat flux in the system. Once the Nusselt number has been calculated, the heat transfer coefficient between the steel or solid salt and the molten salt can simply be calculated using equation (4.26).

$$h_{sms} = Nu\,\frac{k(T_{ms})}{d_{int}}$$
$$h_{ssms} = Nu\,\frac{k(T_{ms})}{d_{ints}} \tag{4.26}$$

Where h_{sms} is the heat transfer coefficient between the steel (s) and the molten salt (ms), h_{ssms} is the heat transfer coefficient between the solid salt (ss) and the

molten salt (ms) and d_{ints} is the internal diameter of the frozen salt wall. The internal diameter of the frozen salt wall is given by equation (4.27).

$$d_{ints} = \sqrt{f_l}\, d_{int} \tag{4.27}$$

The thermal resistance that exists between the steel or the solid salt and the molten salt is then given by equation (4.28).

$$R_{sms} = \frac{1}{h_{sms}\, A_{int}}$$
$$R_{ssms} = \frac{1}{h_{ssms}\, A_{int}} \tag{4.28}$$

Where R_{sms} is the resistance between the steel and the molten salt, R_{ssms} is the resistance between the solid salt and the molten salt and A_{int} is the internal circumferential area of the pipe or frozen salt layer.

The latent heat of fusion of Solar Salt is given by Archimede (n.d.) as 161 kJ/kg and the latent heat of fusion of Hitec^{TM} salt is given by Lu et al. (2013) as 59 kJ/kg. This is the amount of energy that needs to be overcome or is released when the salt mixture changes from a liquid to a solid or a solid to a liquid. For most pure substances, such as water, there is no temperature change while the substance undergoes phase change and all available energy is dedicated to overcoming the latent heat of fusion. For most impure substances, such as salt mixtures, the phase change takes place over a range of temperatures, as was discussed in Section 3.2. When the molten salt enters the mushy region, a portion of the energy goes towards overcoming the latent heat of fusion, while the remaining energy still causes a temperature change. As a result, the rate of temperature change decreases. Similarly, if the molten salt is melting again, any incoming energy is divided between melting the frozen salt and increasing the salt temperature, resulting in a decrease in the rate of temperature change. $Q_{LH,}$ from Figure 4.6, is the rate of energy change due to latent heat, which occurs during a single time step, and can be calculated using equation (4.29).

$$\dot{Q}_{LH} = \frac{\frac{L_h\, \rho_{T_{ms}}}{\Delta t}}{f_{l_k} - f_{l_{k-1}}} \tag{4.29}$$

Where $\dot{Q}_{LH}$ is the rate of energy change during the time step due to latent energy, L_h is the specific latent heat of fusion, Δt is the time step and the subscript k refers to the current iteration in time. Note that the change in liquid fraction is representative of the change in volume between the two time steps. Equation (4.30) is then simply the latent heat of fusion rewritten in terms of a rate of energy change between two time steps for which a phase change has occurred.

Furthermore, the axial convective heat transfer or flow terms between the current molten salt spatial increment i and its two bordering spatial increments $i-1$ and $i+1$, given as Q_{in} and Q_{out} in Figure 4.6, is taken into account in an energy balance. This energy balance is solved to determine the new molten salt temperature. According to Yan et al. (1989), axial conduction in the molten salt can be neglected as it is relatively insignificant. This was further investigated to

confirm that this assumption is valid. According to Hartnett et al. (1998), the Peclet number, defined as the heat transported by convection divided by the heat transported by conduction, can be used to determine whether axial conduction may be neglected. Hartnett et al. (1998) proposes testing whether the Peclet number is below 100 as a conservative test for whether axial conduction should be included. The Peclet number was calculated for several scenarios and was found to be well above 100 in each case. It was, therefore, decided to neglect axial conduction in this study.

In the previously mentioned energy balance, each spatial increment is sufficiently small so that a lumped thermal capacity model approach may be applied to each spatial increment (Mills & Ganesan, 2015). For this approach, each element is assumed to be sufficiently small so that the temperature in the cell can be assumed to be uniform. Using this assumption, the energy balance is taken and derived into a form whereby the new molten salt temperature can be calculated using a computer. Note that k still refers to the current time step and i still refers to the current spatial cell. For the case where no freezing has taken place and the molten salt is in direct contact with the receiver tube wall, the molten salt initial system energy balance can be written as indicated by equation (4.30).

$$\frac{m_{ms}\, c_{p_{ms\,T_{ms}}} \left[T_{ms}{}_{k}^{\,i} - T_{ms}{}_{k-1}^{\,i}\right]}{\Delta t} = \dot{m}\, c_{p_{ms\,T_{ms}}} \left[T_{ms}{}_{k-1}^{\,i-1} - T_{ms}{}_{k-1}^{\,i}\right]$$
$$-\dot{m}\, c_{p_{ms\,T_{ms}}} \left[T_{ms}{}_{k-1}^{\,i} - T_{ms}{}_{k-1}^{\,i+1}\right] + \frac{T_{s}{}_{k-1}^{\,i-1} - T_{ms}{}_{k-1}^{\,i}}{R_{sms}} + \dot{Q}_{LH} \tag{4.30}$$

Where m_{ms} is the mass of the molten salt for the current cell and T_s is the temperature of the steel receiver tube. The term on the left-hand side of equation (4.30) represents the energy change that occurs in the cell during the current time step for the current spatial increment. This is approximated as the rate of energy change that occurs in the cell during the current time step for the previous spatial increment. This will result in some small error, but is required when using the central differencing method used here. The first term on the right-hand side of equation (4.30) is the energy flow rate into the current cell (Q_{in} in Figure 4.6) and the second term on the right-hand side is the energy flow rate out of the current cell (Q_{out} in Figure 4.6). The third term on the right-hand side defines the heat transfer rate between the steel and the molten salt (Q_{sms} in Figure 4.6) and the fourth term is the energy transfer rate due to latent heat (Q_{LH} in Figure 4.6). Next, both sides of equation (4.30) are multiplied by dt to obtain equation (4.31).

$$m_{ms}\; c_{p_{ms\,T_{ms}}} dT_{ms}{}^{i}(t) = \dot{m}\; c_{p_{ms\,T_{ms}}} \left[T_{ms}{}_{k-1}^{\,i-1} - T_{ms}{}_{k-1}^{\,i}\right]dt$$
$$-\dot{m}\, c_{p_{ms\,T_{ms}}} \left[T_{ms}{}_{k-1}^{\,i} - T_{ms}{}_{k-1}^{\,i+1}\right]dt + \frac{T_{ms}{}_{k-1}^{\,i-1} - T_{ms}{}_{k-1}^{\,i}}{R_{sms}} dt + \dot{Q}dt \tag{4.31}$$

Then, equation (4.31) is rearranged to suit the needs of the final solution and similar terms are grouped. The result is given by equation (4.32).

$$\frac{d\left(T_{ms_k}^{\ i} - T_{s_{k-1}}^{\ i}\right)}{T_{ms_{k-1}}^{\ i} - T_{s_{k-1}}^{\ i-1}} = -\left[\frac{\left[T_{ms_{k-1}}^{\ i-1} - T_{ms_{k-1}}^{\ i}\right]}{T_{ms_{k-1}}^{\ i} - T_{s_{k-1}}^{\ i-1}} - \frac{\left[T_{ms_{k-1}}^{\ i} - T_{ms_{k-1}}^{\ i+1}\right]}{T_{ms_{k-1}}^{\ i} - T_{s_{k-1}}^{\ i-1}}\right] dt$$
$$-\left[\frac{1}{R_{sms}} + \frac{\dot{Q}}{m_{ms}\ c_{p_{ms_{T_{ms}}}}\left(T_{ms_{k-1}}^{\ i} - T_{s_{k-1}}^{\ i-1}\right)}\right] dt \tag{4.32}$$

Next, a parameter b is introduced and defined by (4.33) as:

$$b = \frac{\left[T_{ms_{k-1}}^{\ i-1} - T_{ms_{k-1}}^{\ i}\right]}{T_{ms_{k-1}}^{\ i} - T_{s_{k-1}}^{\ i-1}} - \frac{\left[T_{ms_{k-1}}^{\ i} - T_{ms_{k-1}}^{\ i+1}\right]}{T_{ms_{k-1}}^{\ i} - T_{s_{k-1}}^{\ i-1}} + \frac{1}{R_{sms}}$$
$$+\frac{\dot{Q}}{m_{ms}\ c_{p_{ms_{T_{ms}}}}\left(T_{ms_{k-1}}^{\ i} - T_{s_{k-1}}^{\ i-1}\right)} \tag{4.33}$$

Note that b is the negative of the term preceding dt in equation (4.32). Make $T_{ms_k}^{\ i-1}$ the subject of the formula, by integrating equation (4.32) as seen in equation (4.34).

$$\int_0^T \frac{1}{T_{ms_{k-1}}^{\ i} - T_{s_{k-1}}^{\ i-1}} d\left(T_{ms_k}^{\ i} - T_{s_{k-1}}^{\ i}\right) = \int_0^t (-b) dt \tag{4.34}$$

Performing the integration shown in equation (4.34) yields equation (4.35).

$$\left(T_{ms_k}^{\ i} - T_{s_{k-1}}^{\ i}\right)\ ln\left(T_{ms_{k-1}}^{\ i} - T_{s_{k-1}}^{\ i-1}\right) = -bt \tag{4.35}$$

Rearrange equation (4.35) to the final form of the derivation, as equation (4.36).

$$T_{ms_k}^{\ i} = \left(T_{ms_{k-1}}^{\ i} - T_{s_{k-1}}^{\ i-1}\right)e^{-bt} + T_{s_{k-1}}^{\ i} \tag{4.36}$$

Note that equations (4.31) and (4.32) have $i+1$ terms. For most spatial increments, these equations are easily applied, but for a few steps no $i+1$ term exists. This occurs when the current spatial increment is the last molten salt spatial increment at the molten salt-air interface. It is then approximated that the molten salt-air interface is insulated, a valid assumption since the thermal conductivity and specific heat capacity of air are much smaller than that of molten salt.

When freezing has begun and the molten salt is no longer in contact with the receiver tube, but rather in contact with the solid salt, the initial system energy balance from the perspective of the molten salt can be written as indicated by equation (4.37). Equation (4.37) is very similar to equation (4.31), with only two changes. The first change is that the steel receiver tube temperatures in equation (4.31) are all replaced with the salt's solidification temperature, T_S. The second change is that the resistance between the steel and the molten salt is replaced with the resistance between the solid salt and the molten salt.

$$\frac{m_{ms}\, c_{p_{ms_{T_{ms}}}} \left[T_{ms_k}^{\ i} - T_{ms_{k-1}}^{\ i}\right]}{\Delta t} = \dot{m}\, c_{p_{ms_{T_{ms}}}} \left[T_{ms_{k-1}}^{\ i-1} - T_{ms_{k-1}}^{\ i}\right]$$
$$-\dot{m}\, c_{p_{ms_{T_{ms}}}} \left[T_{ms_{k-1}}^{\ i} - T_{ms_{k-1}}^{\ i+1}\right] + \frac{T_S - T_{ms_{k-1}}^{\ i}}{R_{ssms}} + \dot{Q} \tag{4.37}$$

In the same way that equation (4.31) was derived into the form seen in equation (4.36), equation (4.37) was also derived into equation (4.38).

$$T_{ms_k}^{\ i} = \left(T_{ms_{k-1}}^{\ i} - T_S\right) e^{-bt} + T_S \tag{4.38}$$

Where b is now defined by equation (4.39).

$$b = \frac{\left[T_{ms_{k-1}}^{\ i-1} - T_{ms_{k-1}}^{\ i}\right]}{T_{ms_{k-1}}^{\ i} - T_S} - \frac{\left[T_{ms_{k-1}}^{\ i} - T_{ms_{k-1}}^{\ i+1}\right]}{T_{ms_{k-1}}^{\ i} - T_S} + \frac{1}{R_{ssms}} + \frac{1}{R_{salt}}$$
$$+ \frac{Q}{m_{ms}\ c_{p_{ms_{T_{ms}}}} \left(T_{ms_{k-1}}^{\ i} - T_S\right)} \tag{4.39}$$

Note that equation (4.39) includes the term Q that contains information about the liquid fraction at the current time, according to equation (4.29). It would then seem that the solution is no longer explicit. The information about the current time step is, however, obtained at a previous distance step, which is why the explicit nature of the equation is preserved.

To confirm that all the mathematical manipulations were done correctly, the problem was also solved implicitly. To do this, equations (4.31) and (4.37) were solved iteratively by first guessing a value for T_{ms} and then iterating until convergence was obtained. The results of the implicit method matched the results of the explicit method used in equation (4.36) and (4.38). This suggests that the mathematical manipulations were done correctly and that the implicit method was coded correctly. Either solution method can be used for this problem. The implicit method requires fewer time steps, but more computational effort per time step. The stability of an explicit method is usually the area of concern, but as stated before, the results from the implicit and explicit methods compare well. As a rule of thumb for explicit methods, the time step should be equal to the smallest cell size divided by the velocity. This condition is met for the time step and spatial increments used in this study. As a result, stability should not be a problem and it was thus decided to employ the explicit method in this study as an alternative to the implicit method that is typically used in CFD and related fields.

4.3.4 Mathematical Model of the Frozen Salt Layer

The solid salt sub-function script is provided in Appendix B.7. If this sub-function results in a change in temperature, it means that a phase change has taken place. The second of the three parts depicted in Figure 4.4 is the solid salt layer. This part is isolated and depicted in Figure 4.7.

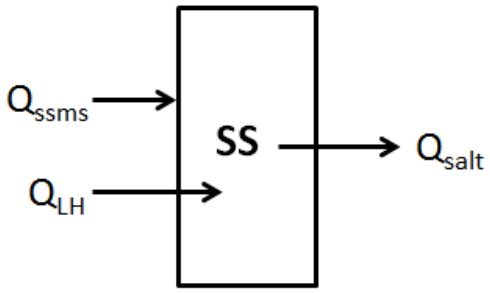

Figure 4.7: Solid salt heat transfer

For the solid salt control volume, three modes of heat transfer are taken into account as seen in Figure 4.7. Q_{ssms} and Q_{LH} are the same terms as defined in Section 4.3.3. Q_{salt} is the heat transfer between the solid salt and the steel receiver tube. The latent energy transfer, Q_{LH}, into the solid salt control volume will result in a phase change in the salt. This phase change will, in turn, result in an increase in the mass of the solid salt control volume being analysed. Since the model is one-dimensional the total energy in the control volume will then also increase. The energy balance must, therefore, include the effect of this increase in mass, determined using the system mass balance. The assumption is made that there will be negligible interfacial resistance between the outer solid salt wall and the inner receiver tube wall. The filling process occurs at low velocities, which in turn results in a negligible amount of air entrapment. With no air present in the molten salt mixture prior to freezing, there can be no air trapped in between the solid salt and receiver tube. For this reason, the assumption that there is too little air in the system to cause significant interfacial resistance is warranted. It follows that the temperature of the solid salt at its external diameter and the temperature of the steel at the internal receiver tube diameter are the same. If this is the case, the only heat transfer taking place between the inner diameter of the frozen salt and the inner diameter of the solid salt is the conduction heat loss through the solid salt. As a result, the term Q_{salt} describes only the conductive radial heat transfer though the solid salt layer.

As was the case in Section 4.3.2 and Section 4.3.3, equations (2.2) and (2.4) are again used to determine the liquid fraction and equation (4.7) to determine the effective internal area of the pipe taking into account the frozen salt in the pipe. For further details relating to these calculations see Section 4.3.2.

To calculate the heat transfer coefficient between the molten salt and the solid salt layer (Q_{ssms} in Figure 4.7), the molten salt mass flow rate, Reynolds number and molten salt to steel receiver tube friction factor first have to be calculated. This is done using equations (4.8), (4.9) and (4.10) as was the case for the pressure and velocity calculations. The Prandtl and Nusselt numbers are then calculated using equation (4.22) to equation (4.25). Once the Nusselt number has been calculated, the heat transfer coefficient between the solid salt and the molten salt can be calculated using equation (4.26). Next, the thermal resistance that exists between the solid salt and the molten salt is again calculated using equation (4.28). This resistance can then be used to calculate the heat transfer rate between the liquid and solid salt. This can be done using equation (4.40).

$$\dot{Q}_{ssms} = \frac{1}{R_{ssms}} (T_{ss} - T_{ms}) \tag{4.40}$$

Where T_{ss} is the solid salt temperature.

Next, the latent heat energy change (Q_{LH} in Figure 4.7) is calculated using equation (4.29). The thermal resistance due to the radial conductance in the solid salt, R_{salt}, (the resistance required to determine Q_{ssms} in Figure 4.7) is calculated using equation (4.41), as proposed by Mills & Ganesan (2015).

$$R_{salt} = \frac{ln\left(\frac{d_{int}}{d_{ints}}\right)}{2\pi\, k_{ms\ T_S} dz} \tag{4.41}$$

Once all the above parameters are known, the initial system energy balance from the perspective of the solid salt can be written as indicated by equation (4.42).

$$\frac{m_{ss}\, c_{p_{ss_{T_{ss}}}} \left[T_{ss}{}^{i}_{k} - T_{ss}{}^{i}_{k-1}\right]}{\Delta t} = \frac{T_{ms}{}^{i-1}_{k-1} - T_{ss}{}^{i}_{k-1}}{R_{ssms}} + \frac{T_{s}{}^{i-1}_{k-1} - T_{ss}{}^{i}_{k-1}}{R_{salt}} + \dot{Q}_{LH} \tag{4.42}$$

Where m_{ss} is the mass of the solid salt in the current control volume that can be calculated using equation (4.43).

$$m_{ss} = \left[\pi\left(\frac{d_{int}}{2}\right)^2 - \pi\left(\frac{d_{ints}}{2}\right)^2\right] dz\, \rho_{ms}(T_{ss}) \tag{4.43}$$

The term on the left-hand side of equation (4.42) represents the energy change that occurs in the cell during the current time step for the current spatial increment. As was the case for the salt, this is approximated as the rate of energy change that occurs in the cell during the current time step for the previous spatial increment. This approximation will result in some small error, which is deemed acceptable to reduce computational effort. The first term on the right-hand side of equation (4.42) represents the heat transfer rate between the solid and liquid salt (Q_{ssms} in Figure 4.7). The second term represents the heat transfer rate between the steel tube and the solid salt, which is equal to the radial conduction energy transfer rate through the solid salt (Q_{salt} in Figure 4.7). The last term on the right-hand side of equation (4.42) is the latent heat term (Q_{LH} in Figure 4.7). Similar mathematical manipulations are performed as was done in Section 4.3.3. Firstly, both sides of equation (4.43) are multiplied by the time step to obtain equation (4.44).

$$\begin{aligned} m_{ss}\, c_{p_{ss_{T_{ss}}}} \left[T_{ss}{}^{i}_{k} - T_{ss}{}^{i}_{k-1}\right] &= \frac{T_{ms}{}^{i-1}_{k-1} - T_{ss}{}^{i}_{k-1}}{R_{ssms}} dt \\ &+ \frac{T_{s}{}^{i-1}_{k-1} - T_{ss}{}^{i}_{k-1}}{R_{salt}} dt + \dot{Q} dt \end{aligned} \tag{4.44}$$

Next, equation (4.44) is rearranged to suit the needs of the final solution and similar terms are grouped. The result is given by equation (4.45).

$$\frac{d\left({T_{ss}}_k^i - {T_s}_{k-1}^i\right)}{{T_{ss}}_{k-1}^i - {T_s}_{k-1}^{i-1}} = -\left[\frac{1}{R_{ssms}} + \frac{1}{R_{salt}} + \frac{\dot{Q}}{m_{ss}\, {c_p}_{ss_{T_{ss}}}\left({T_{ms}}_{k-1}^i - {T_s}_{k-1}^{i-1}\right)}\right] dt \tag{4.45}$$

Next, a parameter b is introduced and defined by equation (4.46) as:

$$b = \frac{1}{R_{ssms}} + \frac{1}{R_{salt}} + \frac{\dot{Q}}{m_{ss}\, {c_p}_{ss_{T_{ss}}}\left({T_{ms}}_{k-1}^i - {T_s}_{k-1}^{i-1}\right)} \tag{4.46}$$

Note that b is the negative of the term preceding dt in equation (4.45). To make ${T_{ss}}_k^{i-1}$ the subject of the formula, equation (4.45) should be integrated as seen in equation (4.47).

$$\int_0^T \frac{1}{{T_{ss}}_{k-1}^i - {T_s}_{k-1}^{i-1}}\, d\left({T_{ss}}_k^i - {T_s}_{k-1}^i\right) = \int_0^t (-b)dt \tag{4.47}$$

Performing the integration shown in equation (4.47) yields equation (4.48).

$$\left({T_{ss}}_k^i - {T_s}_{k-1}^i\right) ln\left({T_{ss}}_{k-1}^i - {T_s}_{k-1}^{i-1}\right) = -bt \tag{4.48}$$

By rearranging equation (4.48), the final form of the derivation can be written as equation (4.49).

$${T_{ss}}_k^i = \left({T_{ss}}_{k-1}^i - {T_s}_{k-1}^{i-1}\right)e^{-bt} + {T_s}_{k-1}^i \tag{4.49}$$

Equation (4.49) can now be used to calculate the new solid salt temperature explicitly.

4.3.5 Mathematical Model of the Receiver Tube

Finally, the third of the three parts depicted in Figure 4.4 is the steel receiver tube. This part is isolated and depicted in Figure 4.8. The MATLAB script for this sub-function is given in Appendix B.8.

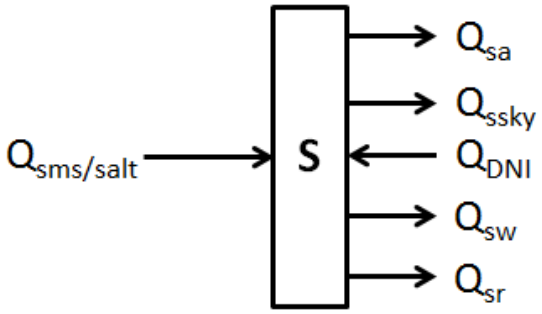

Figure 4.8: Steel receiver tube heat transfer

From Figure 4.8, it can be seen that either the heat transfer term Q_{sms} or Q_{salt} will be present depending on whether freezing has taken place. Q_{salt} will be used if freezing has occurred, otherwise Q_{salt} will be used. These two terms are still defined as in Sections 4.3.3 and 4.3.4. Q_{sa}, Q_{ssky}, Q_{DNI}, Q_{sw} and Q_{sr} are all defined in Section 4.3.

Again, the first step in determining the new receiver tube temperature is to determine the current phase of the molten salt and the corresponding effective internal tube area, as was done in Section 4.3.2, Section 4.3.3 and Section 4.3.4. Equations (2.2) and (2.3) again used to determine the liquid fraction and equation (4.7) to determine the effective internal area of the pipe taking into account potential frozen salt in the pipe. For further details relating to these calculations see Section 4.3.2.

It was initially assumed that radiation heat transfer would exist between the receiver tubes. The significance of the number of tubes in the receiver panel was investigated. To do this, the user should input a number of unique receiver tubes, which the program then uses to calculated the radiation heat transfer between those tubes. The heat transfer coefficients between the tubes were calculated by first determining the shape factors according to the procedures described by Falcone (1986). The heat transfer between the tubes was taken into account in the overall system energy balance, but little to no temperature difference was recorded between the tubes when the solar field is offline. From these results it was determined that it is sufficient to only consider one receiver tube, rather than an entire receiver panel. Refer to Appendix A to see how the heat transfer coefficients and thermal resistance between the receiver tubes were calculated.

As was the case for the HTF, if there is no frozen salt in the pipe, the heat transfer coefficient between the molten salt and the steel receiver tube has to be calculated. To do this the molten salt mass flow rate, Reynolds number and molten salt to steel pipe friction factor are again calculated using equations (4.8), (4.9) and (4.10). The Prandtl number is also calculated again using equation (4.22). To calculate the thermal resistance between the steel receiver tube and the molten salt, the same approach that was taken in Section 4.3.3 was followed again and equations (4.23) to (4.28) are applied to obtain the resistance value. From the resistance value, the heat transfer rate between the steel receiver tube and the molten salt (Q_{sms} in Figure 4.8) can be determined by equation (4.50).

$$\dot{Q}_{sms} = \frac{T_{s_{k-1}}^{\ i} - T_{ms_k}^{\ i}}{R_{sms}} \tag{4.50}$$

If, however, salt has started to freeze on the walls of the pipe, the thermal resistance between the steel receiver tube and the solid salt, R_{salt}, is calculated using equation (4.41). The heat transfer rate between the receiver tube and the solid salt (Q_{salt} in Figure 4.8) can then be calculated using equation (4.51).

$$\dot{Q}_{salt} = \frac{T_{s_{k-1}}^{\ i} - T_{ss_k}^{\ i}}{R_{salt}} \tag{4.51}$$

The convective heat transfer coefficient between the outer surface of the steel tube and the air (used to obtain Q_{sa} in Figure 4.8) has to be determined. The method proposed by Mills & Ganesan (2015) is followed to determine this coefficient. First the mean temperature is calculated using equation (4.52).

$$T_{mean} = \frac{T_a + T_{s_{k-1}}^{i}}{2} \tag{4.52}$$

Where T_a is the ambient air temperature. A value, β, is then defined as the inverse of T_{mean} as shown in equation (4.53).

$$\beta = \frac{1}{T_{mean}} \tag{4.53}$$

According to Mills & Ganesan (2015), the Rayleigh number is then determined for external natural flow over a vertical cylinder using equation (4.54).

$$Ra = \frac{\beta \left(T_{s_{k-1}}^{i} - T_a\right) g \, {d_{ext}}^3}{{\upsilon_{air}}_{T_{mean}}^{\,2} \, Pr_{air_{T_{mean}}}} \tag{4.54}$$

Where Ra is the Rayleigh number, d_{ext} is the external diameter of the tube, υ_{air} is the kinematic viscosity of the air and Pr_{air} is the Prandtl number of the air. Note that the air temperature, T_a, which is in contact with the tube, will not be constant. Forced convection will cause the air to move upwards along the heated tube in a similar way to what is expected in a cooling tower. As a result, the air in contact with the tube will be hotter at the top of the tube than at the bottom. This is, however, a complex problem to simulate accurately as cooler cross wind air and heated air driven vertically by natural convection need to be considered. The interfaces and mixing between these air streams will also have to be considered. Due to the complexity of this problem, an assumption is made that the air temperature is fixed. This fixed value is lower than the actual variable air temperature at any point making the assumption a conservative one, as a lower air temperature will result in more rapid freezing of the salt inside the tube.

Once the Rayleigh number is known, Mills & Ganesan (2015) proposes an equation to determine the Nusselt number for external natural flow over a vertical cylinder. This correlation is given by equation (4.55).

$$Nu = 0.36 + \frac{0.518 Ra^{\frac{1}{4}}}{\left[1 + \left(\frac{0.559}{Pr_{air_{T_{mean}}}}\right)^{\frac{9}{16}}\right]^{\frac{4}{9}}} \tag{4.55}$$

The heat transfer coefficient can then simply be calculated using equation (4.56).

$$h_{sa} = Nu \, \frac{k_{air_{T_{mean}}}}{d_{ext}} \tag{4.56}$$

Where h_{sa} is the heat transfer coefficient between the steel (s) and the air (a) and k_{air} is the thermal conductivity of air. Once this is calculated, the thermal resistance that exists between the steel and the air can be obtained by equation (4.57).

$$R_{sa} = \frac{1}{h_{sa}\, A_{ext}} \tag{4.57}$$

Where R_{sa} is the thermal resistance between the steel receiver tube and the air, and A_{ext} is the external circumferential area of the receiver tube.

The radiation heat transfer coefficient between the steel receiver tube and the sky (used to obtain Q_{ssky} in Figure 4.8) is determined using equation (4.58) (Mills & Ganesan, 2015).

$$h_{ssky} = \varepsilon_s\, F_{ssky}\, \sigma \left[\left(T_{s_{k-1}}^{\,i}\right)^2 + T_a{}^2\right]\left(T_{s_{k-1}}^{\,i} + T_a\right) \tag{4.58}$$

Where h_{ssky} is the heat transfer coefficient between the steel receiver tube and the sky, and ε_s is the steel coating emissivity value. Note that for this study, the sky observed by the receiver is just the air close to the receiver, but is referred to as sky to make the distinction between radiation and convection. Ambrosini et al. (2011) conducted experiments at the Sandia National Laboratories to determine the absorptivity and emissivity of common central receiver collector coatings. Pyromark High Temperature paint is the most commonly used coating and has an emissivity of about 0.88, which is the value used in the current study (Ambrosini et al., 2011). F_{ssky} is the shape factor between the steel receiver tube and the sky, and is given a value of one since the entire tube is in full view of the sky. The Stephan-Boltzmann constant, σ, has a value of 5.67×10^{-8} W/m^{2}K^4. The resistance between the steel tube and the sky is then given by equation (4.59).

$$R_{ssky} = \frac{1}{h_{ssky}\, A_{ext}} \tag{4.59}$$

Where R_{ssky} is the resistance between the steel receiver tube and the sky. For the validation cases, no DNI, wind or rain is included. Later simulations, however, do consider the heat transfer effects of these three conditions. The heat transfer rate from the sun incident on the receiver tube (Q_{DNI} in Figure 4.8) is calculated using equation (4.60).

$$\dot{Q}_{DNI} = C\, DNI\, A_{ext} \tag{4.60}$$

Where C is the solar concentration ratio defined as the effective heliostat aperture area over the effective area of the receiver and DNI is the direct normal irradiance from the sun and is measured in W/m^2.

The heat transfer resulting from wind passing over the receiver tubes is treated as a forced convection problem. Mills & Ganesan (2015) proposes a method for determining the heat transfer coefficient due to forced convection over a vertical

cylinder. First the Reynolds number of the wind needs to be calculated using equation (4.61).

$$Re_w = \frac{v_{wind}\, d_{ext}}{v_{air\,T_{mean}}} \tag{4.61}$$

Where v_{wind} is the velocity of the wind. Association (n.d.) provides classifications of different wind speeds. It was decided to use a wind speed of 103 km/h, which is the lower limit of the wind speeds expected in a storm (Association, n.d.). It is more likely that there will be a single cloud rather that a storm during filling operation. This being said, the receiver can be filled within one to two seconds. In this timeframe, a single strong gust may reach the wind speed mentioned. Although technically possible, evaluating such a high wind speed is done more out of curiosity. If the Reynolds number obtained by equation (4.61) is less than 104, Mills & Ganesan (2015) suggests using equation (4.62) to calculate the Nusselt number.

$$Nu = 0.3 + \frac{0.62 Re^{\frac{1}{2}}\, Pr_{air\,T_{mean}}^{\frac{1}{3}}}{\left[1 + \left(\frac{0.4}{Pr_{air\,T_{mean}}}\right)^{\frac{2}{3}}\right]^{\frac{1}{4}}} \tag{4.62}$$

If the Reynolds number falls between 2×10^4 and 4×10^5, equation (4.63) should be used to determine the Nusselt number (Mills & Ganesan, 2015).

$$Nu = 0.3 + \frac{0.62 Re^{\frac{1}{2}}\, Pr_{air\,T_{mean}}^{\frac{1}{3}}}{\left[1 + \left(\frac{0.4}{Pr_{air\,T_{mean}}}\right)^{\frac{2}{3}}\right]^{\frac{1}{4}}} \left[1 + \left(\frac{Re}{282000}\right)^{\frac{1}{2}}\right] \tag{4.63}$$

Otherwise, if the Reynolds number falls between 4×10^5 and 5×10^6, equation (4.64) should be used to calculate the Nusselt number.

$$Nu = 0.3 + \frac{0.62 Re^{\frac{1}{2}}\, Pr_{air\,T_{mean}}^{\frac{1}{3}}}{\left[1 + \left(\frac{0.4}{Pr_{air\,T_{mean}}}\right)^{\frac{2}{3}}\right]^{\frac{1}{4}}} \left[1 + \left(\frac{Re}{282000}\right)^{\frac{5}{8}}\right]^{\frac{4}{5}} \tag{4.64}$$

From the Nusselt number, the heat transfer coefficient due to the wind flowing over the steel receiver tube (used to obtain Q_{sw} in Figure 4.8) can then be obtained by using equation (4.65).

$$h_{sw} = Nu \frac{k_{air_{T_{mean}}}}{d_{ext}} \tag{4.65}$$

This heat transfer coefficient can then be used to determine the resistance between the steel receiver tube and the wind. This resistance is calculated using equation (4.66).

$$R_{sw} = \frac{1}{h_{sw}\, A_{ext}} \tag{4.66}$$

Some potential ways of modelling rain falling on the receiver tube was discussed in Section 3.3. Two approaches were considered, one by Jafari (2014) and one by Wendelstorf et al. (2008). After reviewing both studies, it was determined that for this study the simulation of rain is too small a part of the model to simulate it in as much detail as Jafari (2014) did. Jafari (2014) performed a drop wise analysis, which would take too much computing power, while Wendelstorf et al. (2008) proposed simpler equations by which to solve the problem. To calculate the heat transfer coefficient between the steel receiver tube and the rain, the temperature differential between the two is first defined, as is done by equation (4.67).

$$dT = T_{s_{k-1}}^{i} - T_{rain} \tag{4.67}$$

Where T_{rain} is the rain temperature set to a value of 5 °C for this study. The rain intensity is determined by using equation (4.68).

$$V_{rain} = \frac{\left(\frac{Rain_{depth}}{1000}\ (1)\ (1)\right)\ (1000)}{(60)\ (60)} \tag{4.68}$$

Where the rain intensity V_{rain} is given in kg/m^{2}s and the depth of the rain that falls in an hour, $Rain_{depth}$, is given in mm/hr. According to USGS (2016), 50 mm per hour or more of rain will fall during a heavy shower. 50 mm/h of rain was therefore chosen as an input to the model. Wendelstorf et al. (2008) proposes a heat transfer coefficient correlation that is only dependent on the rain intensity and the temperature differential defined by equation (4.67). This correlation is given by equation (4.69) (Wendelstorf et al., 2008).

$$h_{sr} = (190 \pm 25) + tanh\left(\frac{V_{rain}}{8}\right)\left(140 \pm 4V_{rain}\left[1 - \frac{V_{rain}\, dT}{72000 \pm 3500}\right] + 3.26 \pm 0.16dT^2\left\{1 - tanh\left(\frac{dT}{128 \pm 1.6}\right)\right\}\right) \tag{4.69}$$

Where h is the heat transfer coefficient between the cooling spray and the wall, ΔT is the temperature difference between the cooling spray and the wall and V_s is the wetting intensity of the spray. The $\pm$ symbols are there to indicate the 95 %-confidence intervals from the experimental data. For this study, the worst-case scenario is evaluated. For this reason, the symbols were chosen so that the heat transfer coefficient would be the highest it can be. This is done by always selecting the plus operator. From this heat transfer coefficient, the resistance

between the steel receiver pipe and the rain (used to obtain Q_{sr} in Figure 4.8) can be calculated using equation (4.70).

$$R_{sr} = \frac{1}{h_{sr}\, A_{ext}} \tag{4.70}$$

As was the case for the HTF, each receiver steel tube spatial increment is sufficiently small that a lumped thermal capacity model approach may be applied to it (Mills & Ganesan, 2015). An energy balance is constructed for the receiver tube and then manipulated into a form whereby a computer can calculate the new receiver tube temperature. The ambient air, rain and sky temperatures are assumed to be equal and expressed as the ambient air temperature, T_a, to simplify the mathematics. This assumption is reasonable because the difference between the air, rain and sky temperatures is small relative to the difference between the steel and air, rain or sky temperature. For the case when no frozen salt is present on the walls of the tube, the energy balance is given by equation (4.71).

$$\begin{aligned} \frac{m_s\, c_{p_{s_{T_s}}} \left[T_{s_k}^{\,i} - T_{s_{k-1}}^{\,i}\right]}{\Delta t} &= \dot{Q}_{sms} + \frac{T_{s_{k-1}}^{\,i-1} - T_a}{R_{sa}} + \frac{T_{s_{k-1}}^{\,i-1} - T_a}{R_{ssky}} \\ +\dot{Q}_{DNI} + \frac{T_{s_{k-1}}^{\,i-1} - T_a}{R_{sw}} &+ \frac{T_{s_{k-1}}^{\,i-1} - T_a}{R_{sr}} \end{aligned} \tag{4.71}$$

Where m_s is the mass of the steel in the current cell. The term on the left-hand side of equation (4.71) represents the energy change that occurs in the steel cell during the current time step for the current spatial increment. This is approximated as the rate of energy change that occurs in the cell during the current time step for the previous spatial increment. This will result in some small error, which is deemed acceptable to reduce computational effort. The first term on the right-hand side of equation (4.71) is the rate of heat transfer from the steel to the molten salt (Q_{sms} in Figure 4.8). The second and third terms on the right-hand side of equation (4.71) are the rate of energy transfer from the steel to the air and sky respectively (Q_{sa} and Q_{ssky} in Figure 4.8). The fourth term is the incoming energy due to solar irradiance (Q_{DNI} in Figure 4.8). Finally, the fifth and sixth terms represent the heat transfer rates due to wind and rain respectively (Q_{sw} and Q_{sr} in Figure 4.8). Next, both sides of equation (4.71) are multiplied by the time step to obtain equation (4.72).

$$\begin{aligned} m_s\, c_{p_{s_{T_s}}}\, dT_s^{\,i}(t) &= \dot{Q}_{sms}dt + \frac{T_{s_{k-1}}^{\,i-1} - T_a}{R_{sa}}dt + \frac{T_{s_{k-1}}^{\,i-1} - T_a}{R_{ssky}}dt \\ +\dot{Q}_{DNI}dt + \frac{T_{s_{k-1}}^{\,i-1} - T_a}{R_{sw}}dt &+ \frac{T_{s_{k-1}}^{\,i-1} - T_a}{R_{sr}}dt \end{aligned} \tag{4.72}$$

After that, equation (4.72) is rearranged to suit the needs of the final solution and similar terms are grouped. The result is given by equation (4.73).

$$\frac{d\left[T_{s_k}^{\ i} - T_a\right]}{T_{s_{k-1}}^{\ i-1} - T_a} = -\left[\frac{\dot{Q}_{sms}}{m_s\, c_{p_{s_{T_s}}}\left(T_{s_{k-1}}^{\ i-1} - T_a\right)} + \frac{1}{m_s\, c_{p_s}\, R_{sa}} + \frac{1}{m_s\, c_{p_s}\, R_{ssky}} + \frac{\dot{Q}_{DNI}}{m_s\ c_{p_{s_{T_s}}}\left(T_{s_{k-1}}^{\ i-1} - T_a\right)} + \frac{1}{m_s\, c_{p_{s_{T_s}}}\, R_{sw}} + \frac{1}{m_s\ c_{p_{s_{T_s}}}\, R_{sr}}\right] dt \tag{4.73}$$

Next, a parameter b is introduced and defined by equation (4.74) as:

$$b = \frac{\dot{Q}_{sms}}{m_s\, c_{p_{s_{T_s}}}\left(T_{s_{k-1}}^{\ i-1} - T_a\right)} + \frac{1}{m_s\ c_{p_{s_{T_s}}}\, R_{sa}} + \frac{1}{m_s\, c_{p_{s_{T_s}}}\, R_{ssky}} + \frac{\dot{Q}_{DNI}}{m_s\, c_{p_{s_{T_s}}}\left(T_{s_{k-1}}^{\ i-1} - T_a\right)} + \frac{1}{m_s\, c_{p_{s_{T_s}}}\, R_{sw}} + \frac{1}{m_s\, c_{p_{s_{T_s}}}\, R_{sr}} \tag{4.74}$$

Where b is the negative of the terms preceding dt in equation (4.73). To make $T_{s_k}^{\ i-1}$ the subject of the formula, equation (4.73) is integrated, as seen in equation (4.75).

$$\int_0^t \frac{1}{T_{s_{k-1}}^{\ i-1} - T_a} d\left(T_{s_k}^{\ i} - T_a\right) = \int_0^t (-b) dt \tag{4.75}$$

Performing the integration shown in equation (4.75) yields equation (4.76).

$$\left(T_{s_k}^{\ i} - T_a\right)\, ln\left(T_{s_{k-1}}^{\ i-1} - T_a\right) = -bt \tag{4.76}$$

Equation (4.76) is rearranged to the final form of the derivation, as seen in equation (4.77).

$$T_{s_k}^{\ i} = \left(T_{s_{k-1}}^{\ i-1} - T_a\right) e^{-bt} + T_a \tag{4.77}$$

Whenever the molten salt has not yet reached the $i+1^{\text{th}}$ term, the initial receiver temperature should be used. This is accurate for the assumption that no axial conduction takes place in the steel receiver tube as suggested by Yan et al. (1989).

Similarly, for the case when freezing has taken place on the internal walls of the tube, equation (4.77) is again used to calculate the new receiver tube temperature. The only difference is that, during the derivation of equation (4.77), the heat transfer rate between the steel tube and the molten salt, $\dot{Q}_{sms}$, is replaced by the heat transfer between the steel receiver tube and the solid salt, $\dot{Q}_{salt}$, defined in equation (4.51).

CHAPTER 5: VERIFICATION AND VALIDATION

Once the model has been built, it needs to be verified and validated to give it credibility. A combined time step and spatial increment verification of the model was conducted as well as a two-part validation.

5.1 Verification

To obtain accurate results, the time step and spatial increment should typically be chosen so that the molten salt passes through each spatial increment in one or more time steps. The molten salt should not pass through more than one spatial increment in one time step. In this section, a time step and spatial increment will be determined for which the solution is independent of these two parameters.

The verification test case was performed under the following conditions:

1) A constant inlet velocity of 2 m/s
2) An inlet molten salt temperature of 273 °C
3) An initial surroundings and receiver tube temperature of 20 °C
4) Plotted 4.2 s after filling is initiated
5) No wind, rain or DNI

Several time step and spatial increment combinations were considered. The results obtained from three combinations shown in Figure 5.1 are sufficient to verify the model. These three combinations are dt = 0.002 s and dz = 0.004 m (combination 1), dt = 0.001 s and dz = 0.002 m (combination 2) and dt = 0.0005 s and dz = 0.001 m (combination 3). In the legend of Figure 5.1, these combinations are referred to only by their time step values.

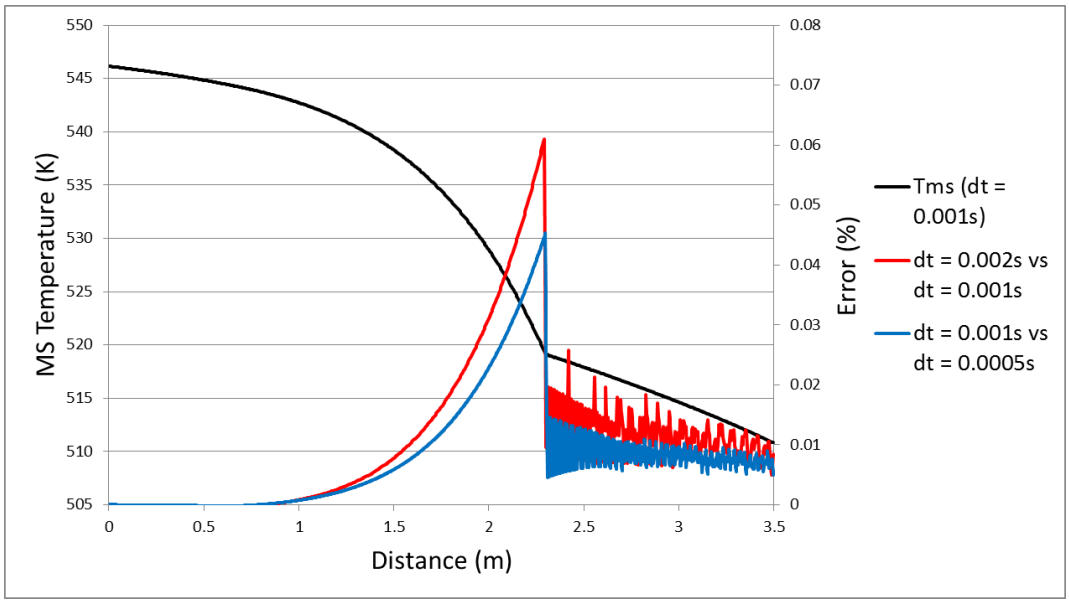

Figure 5.1: Relative error between different time steps and spatial increments

The molten salt temperature profile for the conditions described and the time step and spatial increment combination 2 is shown in Figure 5.1 as a black line. The error that exists between combination 1 and combination 2 is plotted in red, while the error that exists between combination 2 and combination 3 is plotted in blue. The maximum error that exists between combination 1 and combination 2 is 0.0610 % and the maximum error that exists between combination 2 and combination 3 is 0.0453 %. Both maximum errors occur at a receiver filling length of 2.29 m, which is where the molten salt temperature drops below the liquidus temperature and the salt's latent heat of fusion reduces the rate at which the molten salt's temperature decreases. Both error profiles are sufficiently small over the entire receiver length to indicate that combination 2 and combination 3 are both accurate enough. Furthermore, the difference between the two error profiles is sufficiently small to indicate that combination 2 may be used. As a result, the model has been validated for dt = 0.001 s and dz = 0.002 m or combination 2. Note, however, that there is some accumulated error present while the molten salt temperature is above the liquidus temperature. Error accumulation is typical of the explicit method used in this model. Care should, therefore, be taken if the maximum receiver length is increased and the temperature never drops below the liquidus temperature, as this may result in excessive errors close to the receiver's maximum length. The verification is, however, more than sufficient for the scenarios considered in this study.

5.2 Validation

Ideally the model should be validated against experimental data rather than other numerical models that may also contain errors. Experimental data is, unfortunately not yet available. As a result the model is validated against two numerical studies. For the first part, characteristic point curves produced by the model built in this study are validated against the study conducted by Liao et al. (2015). Characteristic point curves are property profiles produced under a single set of conditions. An example would be to plot molten salt temperature versus time at a certain distance for one initial receiver tube temperature. As was the case for the study conducted by Liao et al. (2015), a characteristic pumping curve, given by equation (4.11), was used to calculate the inlet velocity. Liao et al. (2015) performed simulations at three initial receiver tube temperatures: T_s = 445 K for which no freezing took place, T_s = 345 K for which partial freezing took place and T_s = 295 K for which complete freezing of the salt in the pipe took place. Note that the Solar Salt properties proposed by Liao et al. (2015) are used for this first validation. Validating against these results will show that the model can produce the correct characteristic trends.

Walker et al. (2003) defines uncertainty as *"any departure from the unachievable ideal of complete determinism"*. At least two types of significant uncertainty defined by Walker et al. (2003) are present in the problem modelled in this study namely: "*absence of knowledge"* and *"unreliability"*. As discussed in Section 4.3.2, there is a complete absence of knowledge regarding the surface roughness of solid salt. In Section 2.1, it was established that significant uncertainty arose from unreliable molten salt property functions. Therefore, it can be said that significant uncertainty is inherently present in the problem. According to Senge & Forrester (1980), it is more important to consider trends for the model

validation of such a problem than the errors between the curves. It is likely that some error between the results obtained by this study and the study conducted by Liao et al. (2015) will exist as the model built by Liao et al. (2015) is a two-dimensional model and this study's model is one-dimensional. Since neither model will be able to predict the true receiver physics exactly, the error between them should simply be small enough to be able to use the results for initial receiver design and operation.

First the pressure along the receiver tube was plotted against receiver length for an initial receiver tube temperature of 445 K at 1.75 s. The resultant pressure profiles for the current study as well as the study performed by Liao et al. (2015) are plotted in Figure 5.2.

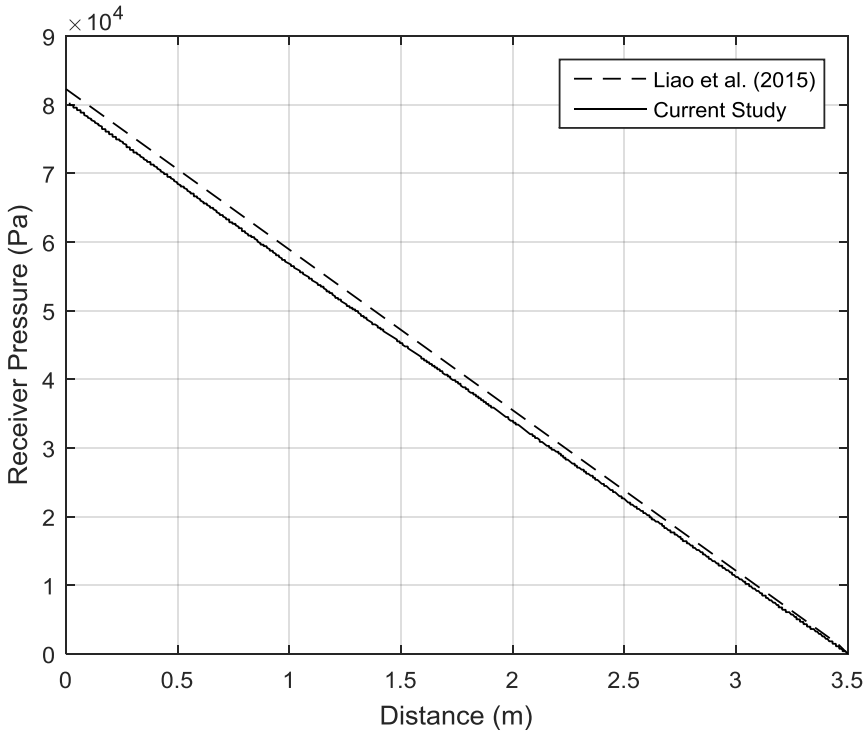

Figure 5.2: Receiver pressure drop versus distance (T_{ms_inlet} = 445 K, t = 1.75 s)

The pressure profiles shown in Figure 5.2 are similar in both their magnitude along the length of the receiver and the trends they follow. Both trends are linear, start at a similar value and decrease to zero at the end of the receiver tube. The pressure plotted is gauge pressure, which is why it decreases to zero at the end of the receiver tube at the moment when the tube is only just filled with salt at 1.75 s. The salt at the end of the tube is subjected to atmospheric pressure or 0 Pa gauge.

The molten salt temperature profiles versus distance for an initial receiver tube temperature of 445 K at 1.75 s for the current study and the study performed by Liao et al. (2015) can be seen in Figure 5.3.

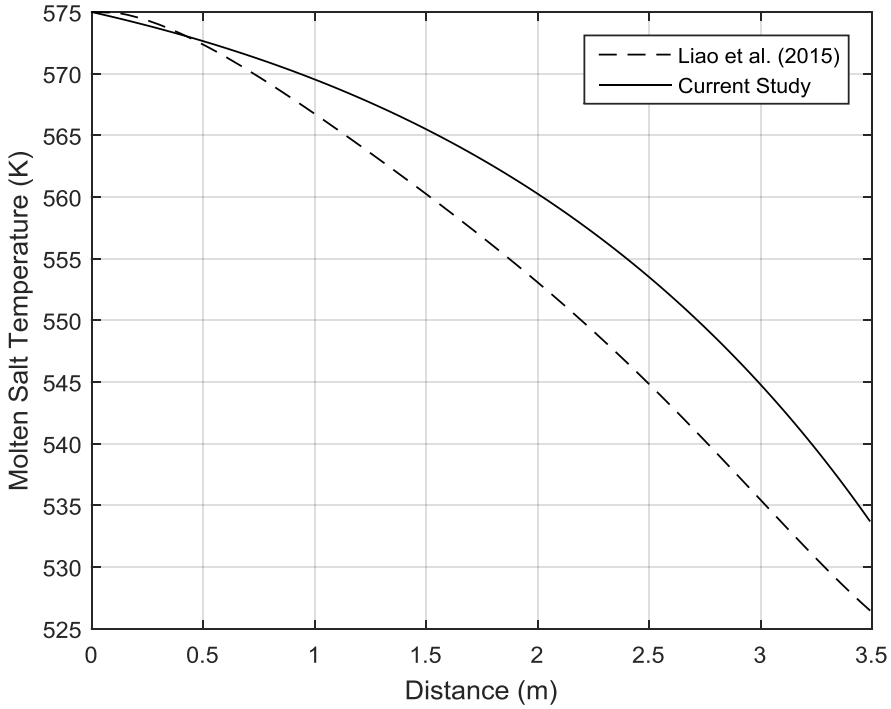

Figure 5.3: Molten salt temperature versus distance (T_{ms_inlet} = 445 K, t = 1.75 s)

Although the error between the curves shown in Figure 5.3 is larger, the trends are again similar. In both cases, the molten salt temperature decreases parabolically. The error is likely due to a loss of information resulting from the one-dimensional assumption. Although the temperature difference observed in Figure 5.3 is large, the time it takes for my model to predict the same temperature is small. The operator, which constantly monitors the plant and decides when to fill or drain the receiver, will likely not be able to respond to an error of this small magnitude as the current model predicts the same temperature as the model built by Liao et al. (2015) about 0.25 s later.

Next, the pressure drop across the receiver length is plotted against time for an initial receiver tube temperature of 295 K. The receiver pressure drop is defined as the pressure differential between the inlet of the receiver tube and the tube exit. The pressure drops obtained from the current study and from the study performed by Liao et al. (2015) are both shown in Figure 5.4.

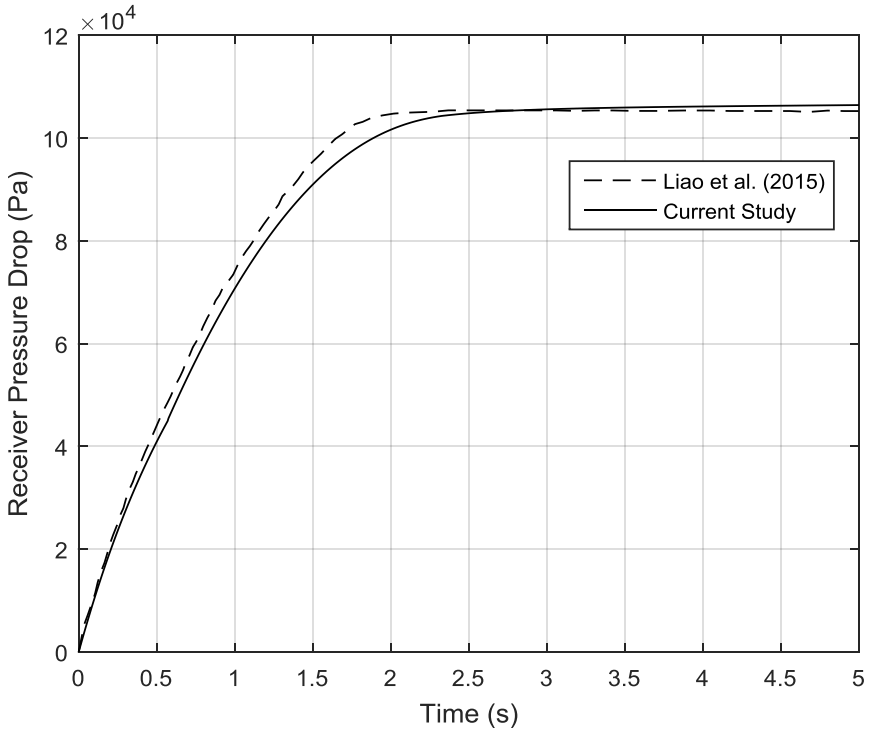

Figure 5.4: Receiver pressure drop versus time (T_{ms} = 295 K)

From Figure 5.4 it can be seen that the two pressure profiles follow the same trend and are also similar in magnitude. The largest error exists at 1.75 s, which is when the receiver tube is completely filled according to Liao et al. (2015). The model presented in this study predicts that the receiver will only be fully filled at about 2 s. As a result, the model presented in the current study predicts that the pressure drop will level out later than the model presented by Liao et al. (2015) suggests. The reason that the pressure drop reaches a near constant value once the receiver tube is fully filled is because the magnitudes of the friction and gravity pressure loss terms, shown in equation (4.14), are highly dependent on the filled length of the receiver. When that filled length reaches its maximum value, it stands to reason that the rate of pressure drop across the receiver tube length will greatly decrease. This will result in the pressure drop levelling out as seen in Figure 5.4. If the receiver pressure drop at 1.75 s for the study performed by Liao et al. (2015) is compared to the receiver pressure drop at 2 s for the current study, it can be seen that these values are nearly equal. Based on these findings, it is clear that the receiver pressure drop profiles correspond well. However, the velocity responses should be compared under these conditions since there is some difference between the predicted filling times.

Under these same conditions, the molten salt velocity at the pipe inlet is plotted against time for both studies. The resulting profiles can be seen in Figure 5.5.

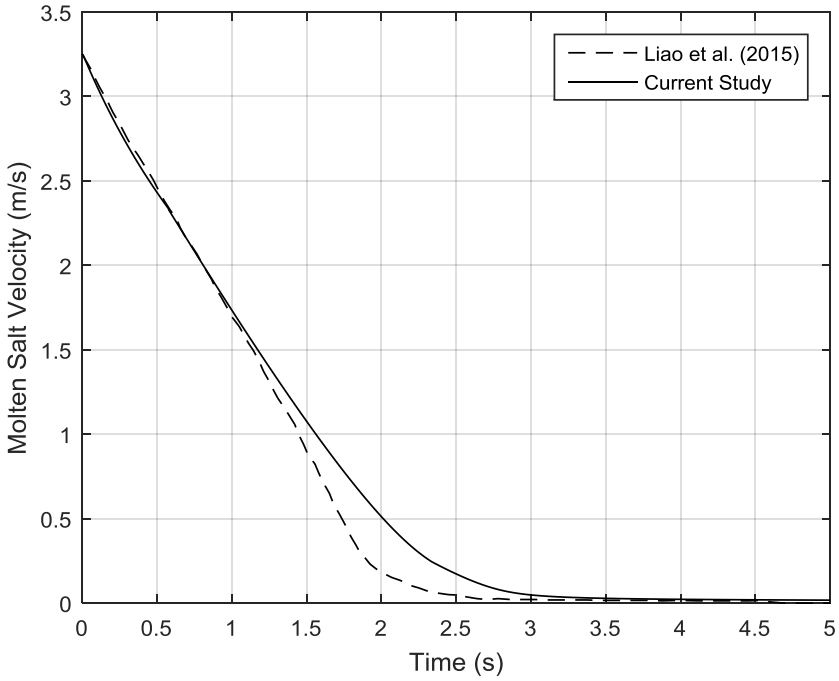

Figure 5.5: Molten salt velocity versus time (T_{ms_inlet} = 295 K, z = 0 m)

The two trends seen in Figure 5.5 are again similar, but some difference does exist between the two trends from about t = 1.4 s to about t = 1.8 s. Within this interval, Liao et al. (2015) predicts a sharper, piecewise linear decrease in velocity. They do not explain this sudden sharper decrease in velocity. If, however, their curve followed the trend from 0 s to 1.4 s over the 1.4 s to 1.8 s interval, their trend would be almost identical to the one proposed by this study. The difference is, however, likely due to Liao et al. (2015) using CFD, which explicitly models the mushy zone as a porous medium. Although the model presented in this study makes use of equation (2.2) to describe the mushy zone, it is not explicitly modelled. The difference in fill time can be explained by the slightly lower velocity predicted by the model proposed in the current study between t = 0 s and t = 0.6 s. Although the underestimating error over this interval is far smaller than the overestimation error between t = 1 s and t = 1.75 s, the underestimating error has a larger impact due to the higher velocity at which it occurs. This difference is, however, not so large as to discredit either model.

Based on the results presented in Figure 5.2 to Figure 5.5 as well as the accompanying findings, the point validation of the model presented in the current study may be considered a success. The next step is to validate the model's response to changes in initial conditions.

This second form of validation was done against the study conducted by Xu et al. (2017). For this validation, the constant inlet velocity assumption is made, as was the case for the study by Xu et al. (2017). Xu et al. (2017) ran several simulations to determine the critical velocity at which the molten salt only just does not fully freeze shut the receiver pipe for a variety of initial receiver tube temperatures and

inlet molten salt temperatures. This type of validation will show that the model reacts to change in the correct way. As motivated previously, it is more important to consider trends for the model validation than the errors between the curves.

It is easier to determine the critical inlet molten salt temperature for various initial receiver tube temperatures at different velocities than vice versa due to the way the model presented in this study is built. The results obtained by Xu et al. (2017) are, therefore, represented in a way so that it is more easily comparable with the results obtained by the model built in this study. The results obtained by Xu et al. (2017) are plotted in Figure 5.6. The results obtained from the model presented in this study are plotted in Figure 5.7.

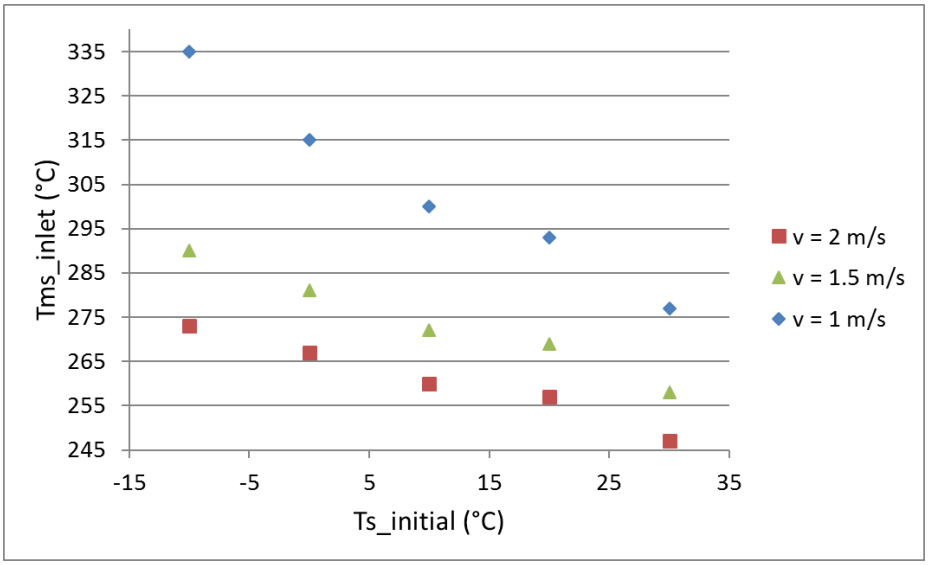

Figure 5.6: Critical inlet molten salt temperatures for different initial receiver tube temperatures at different velocities (Xu et al. (2017)

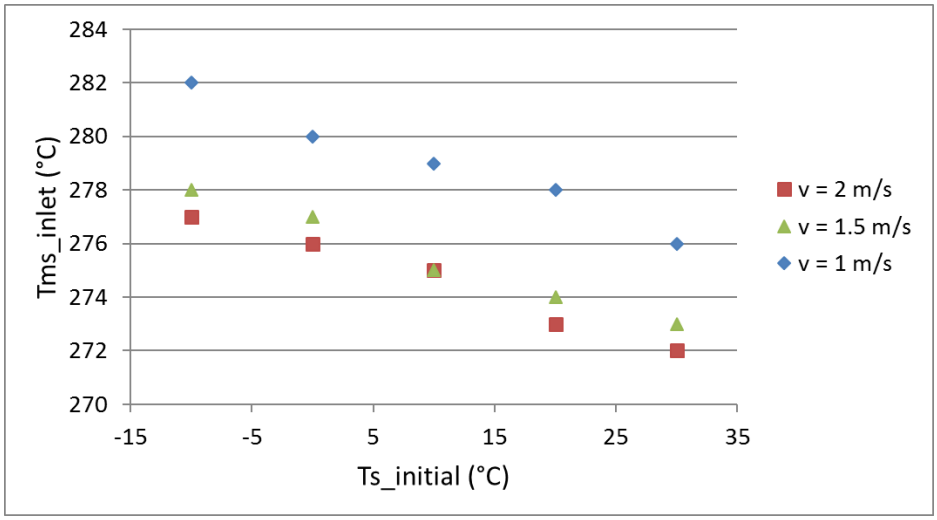

Figure 5.7: Critical inlet molten salt temperatures for different initial receiver tube temperatures at different velocities (current study data)

At first glance, it can be seen that the trends in Figure 5.6 and Figure 5.7 are similar. Upon closer inspection of the y-axis, it can be seen that Xu et al. (2017) predicts a far wider inlet molten salt temperature range than the model presented in this study does. The conclusion that can be drawn from this is that both models respond to change in the same way, but the model proposed by Xu et al. (2017) predicts that the system is far more sensitive to change than the model proposed in the current study does. The trends have, however, been shown to correspond well, which is the more important factor to consider. The biggest difference is that Xu et al. (2017) can model the molten salt, mushy zone and solid salt in the radial direction at any location along the pipe axis, whereas the current model can only model the salt as being in one of those three states at any one location along the pipe axis. It is encouraging to see how well this reduced physics model performed as compared to the CFD models built by previous authors taking into account that the CFD models take several days to run a simulation, which the current model takes about one hour to perform.

From all the results discussed in this section, it was seen that some difference, small or large, does exist between the validation case results and the results obtained from this study. These errors can be due to any number of reasons, for example: the model presented in this study is one-dimensional while the validation case models are both multi-dimensional; the model presented in this study calculates heat transfer coefficients between different elements, while both validation case models assume a constant heat transfer coefficient; and the model built by Xu et al. (2017) uses a time step of only 0.05 s, which by their own admission may be too large and requires further investigation, while the time step the model presented in this study uses was verified in Section 5.1. Even though errors ranging from 0 % to about 15 % do exist, the trends for the validation case and the current model corresponded well. As a result, it was determined that the model is sufficiently validated and can be used with confidence for the rest of the study.

CHAPTER 6: RESULTS

Once validated, the model can be used to further investigate the cold filling method. To understand how the molten salt responds during the cold filling process, the characteristic molten salt trends are plotted and explained for a single set of test conditions. Next, an analysis of the system's reaction during cold filling is determined if the system is subjected to strong wind and heavy rain. The effect of the receiver pipe size on the cold filling process is also investigated. Finally, the effect that using a different salt mixture as well as using different property functions for the same salt mixture has on the cold filling process is examined.

6.1 Molten Salt Characteristics

The molten salt characteristics are evaluated at an inlet molten salt temperature of 280 °C, an initial receiver tube temperature of 20 °C and an inlet velocity of 2 m/s. The same molten salt properties shown in Table 4.1 are used for all test cases unless stated otherwise.

The first plot, seen in Figure 6.1, is the liquid fraction of the salt plotted over the length of the receiver at 1.75 s. 1.75 s was chosen as it is the time at which the receiver is fully filled.

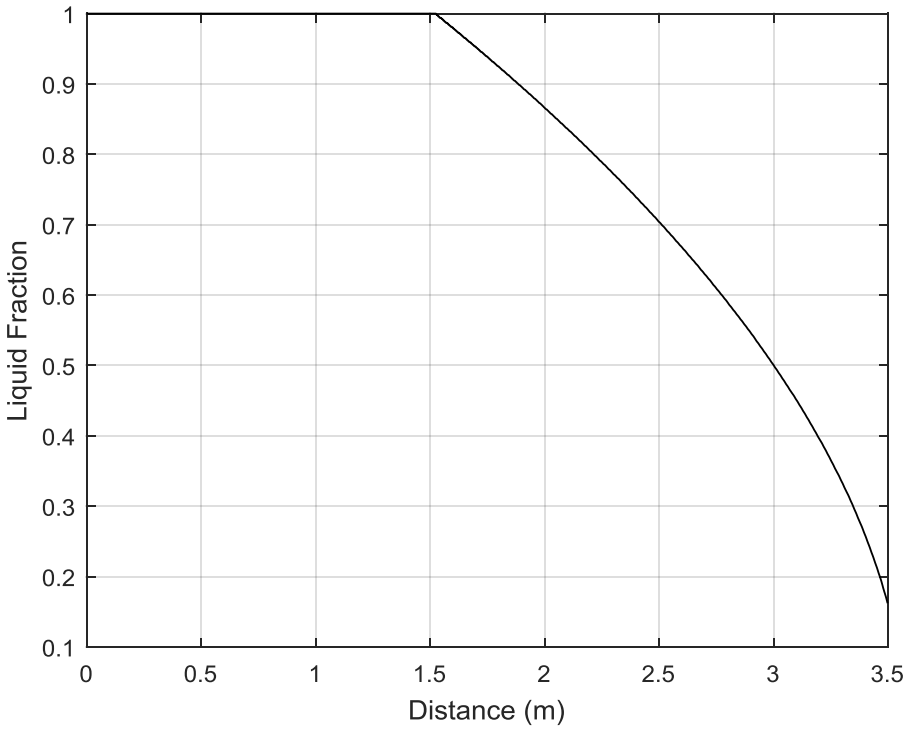

Figure 6.1: Test case - liquid fraction versus distance (*t* = 1.75 s)

It has been determined that the liquid fraction is always at its lowest at the maximum receiver length when the receiver is fully filled for the first time. Based on this observation and the results seen in Figure 6.1, it can then be said that partial freezing occurs for this test case, with a minimum liquid fraction of about 0.16.

The liquid fraction is plotted against time at five distances along the receiver as seen in Figure 6.2. This plot is generated to observe the development of the frozen salt profile within the pipe.

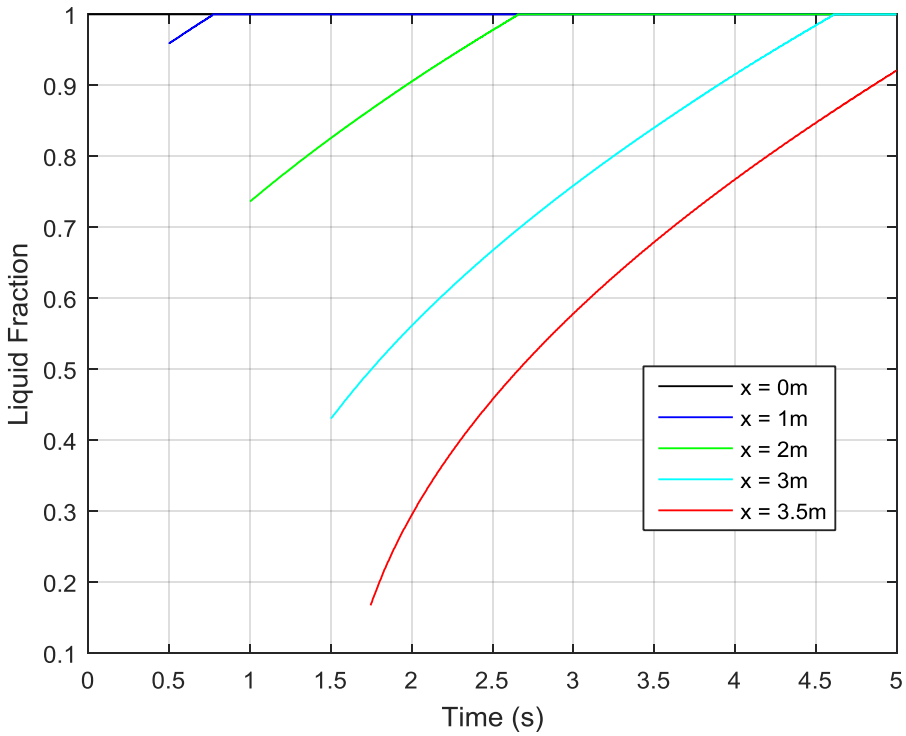

Figure 6.2: Test case - liquid fraction versus time for five distances

Notice again that the maximum amount of freezing takes place at 1.75 s and at 3.5 m, as seen in Figure 6.2. This is to be expected as there are no external variable heating or cooling sources. The molten salt that enters the pipe in the first spatial increment will be subjected to the harshest cooling effects as it comes into contact with the receiver tube when it is at its lowest temperature. This molten salt cell will come into contact with the receiver tube at its initial temperature at each new time step as well, which is why it must be at the system's lowest temperature at the time when it reaches the maximum receiver length. Each new spatial increment of molten salt will come into contact with the receiver tube, which is at a slightly higher temperature than it was when the previous molten salt cell came into contact with it, resulting in remelting of the salt and therefore a slightly higher liquid fraction. This causes the increasing trends seen in Figure 6.2.

The molten salt temperature response versus distance at five different times is shown in Figure 6.3. From Figure 6.3, the molten salt temperature profiles as well as the way in which these temperature profiles evolve over time can be investigated.

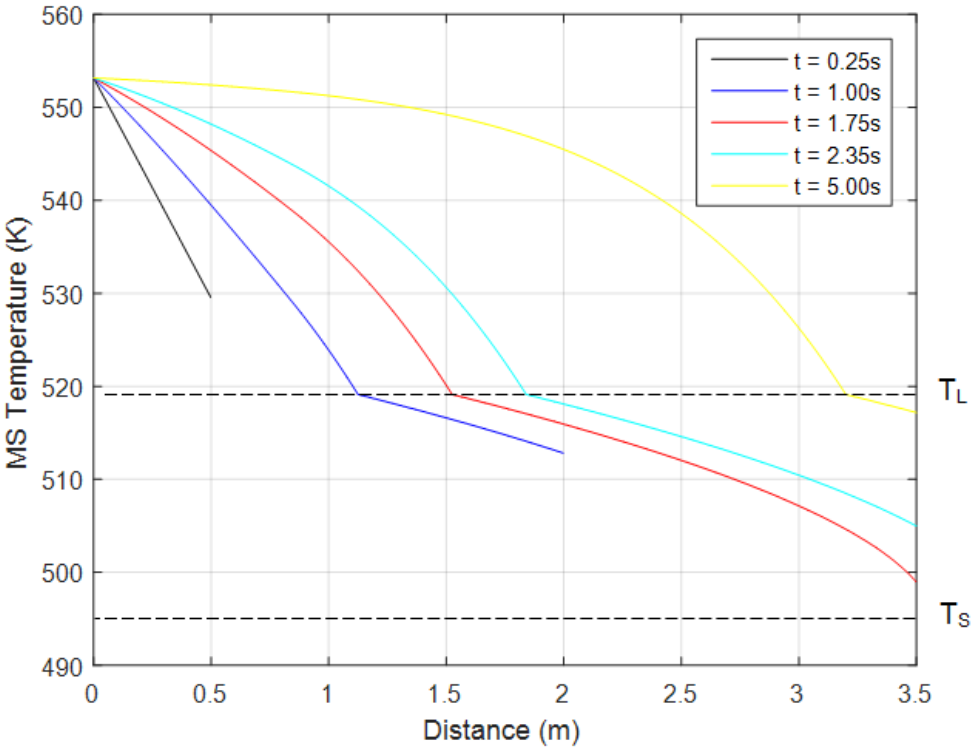

Figure 6.3: Test case - molten salt temperature versus distance at different times

Considering any one of the five curves in Figure 6.3, a decreasing temperature profile can be observed. As explained previously, the temperature decreases with distance along the pipe due to the heat it loses from heating the receiver pipe. Considering all five curves in Figure 6.3, it can be seen how the molten salt temperature profiles evolve with time. Until the receiver is fully filled at 1.75 s, each new curve has a lower minimum molten salt temperature. However, each new curve only drops below the previous curve's minimum temperature further down the pipe. Once the pipe has been fully filled, the minimum molten salt temperature for each new curve starts to increase again. This is because at this point there are no longer any new sections of unheated receiver tube to decrease the temperature of the molten salt at its leading edge. When the molten salt temperature drops below the liquidus temperature of 246 °C (519.15 K), as is the case for four of the curves seen in Figure 6.3, the rate of temperature change suddenly decreases. It is in this mushy zone temperature band, between the liquidus and solidus temperatures, that latent energy is stored as freezing takes place. When freezing takes place in the mushy zone, some energy is transferred so that the molten salt temperature decreases, while the rest is stored as latent energy in the solid salt. It is this latent energy storage that causes the sudden change in the temperature profiles seen in Figure 6.3.

The response of the molten salt over time at five locations along the pipe is recorded in Figure 6.4. The temperature response over distance and time is contrasted between Figure 6.3 and Figure 6.4.

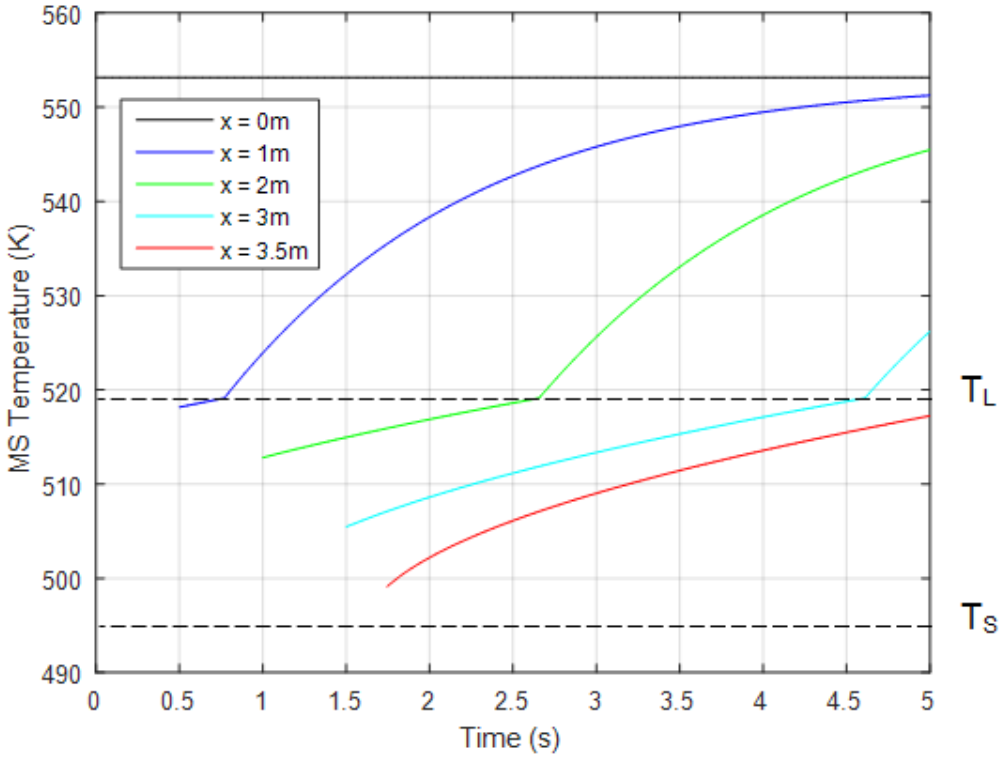

Figure 6.4: Test case - molten salt temperature versus time for five distances

While the molten salt temperature decreases with distance, it increases with time, as seen in Figure 6.4. The molten salt temperature at the receiver inlet, indicated with a black line in Figure 6.4, remains constant as it is one of the problem boundary conditions. The rest of the curves show how the molten salt reaches each specific location in a partially frozen state for the first time. The molten salt temperature increases over time at each location as new hotter molten salt reaches the same point. The effects of the molten salt latent heat of fusion can again be seen in the mushy zone as the salt in the pipe thaws. Notice that the molten salt temperature at the maximum receiver length is still below the liquidus temperature after the 5 s of real time that this simulation was run for.

The last characteristic curves investigated in this sub-section show the relationship between the molten salt temperature and the receiver tube temperature. The molten salt and receiver tube temperatures at the receiver inlet are plotted against time, as seen in Figure 6.5.

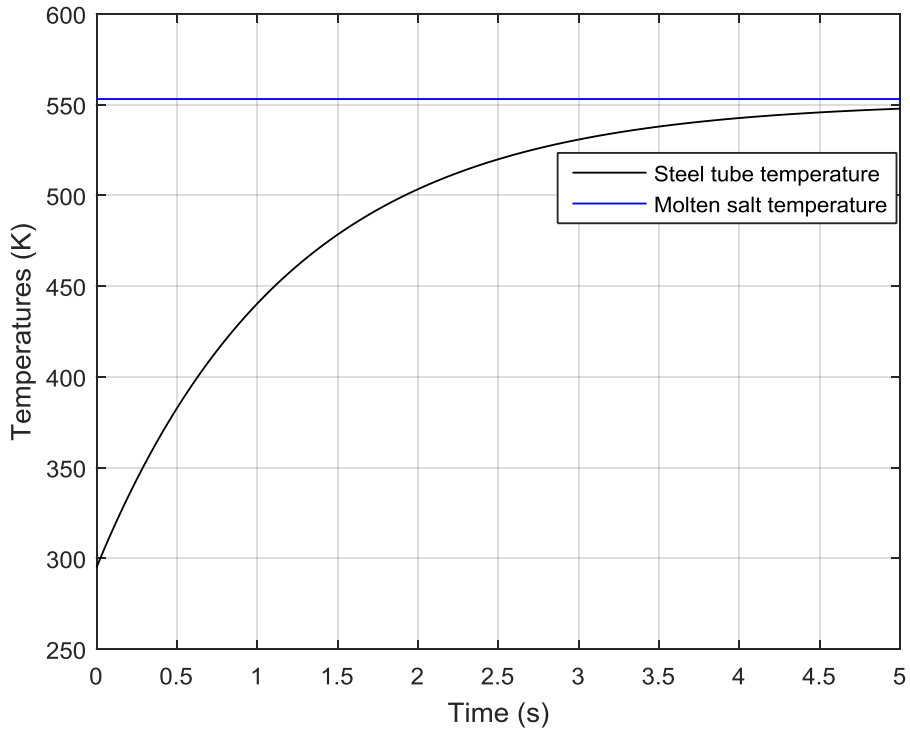

Figure 6.5: Test case - molten salt and receiver tube temperatures versus time

The inlet molten salt temperature is set to a constant value, as seen in Figure 6.5. The steel receiver tube is then heated by the molten salt over time until the receiver temperature profile forms an asymptote to the molten salt temperature. The asymptote forms as the temperature difference between the receiver tube and the molten salt decreases and so too the heat transfer between them. The receiver tube temperature profile seen in Figure 6.5 is, therefore, intuitively typical of this situation.

6.2 Extreme Weather Analysis

The effects of a sudden down pour of rain coupled with strong wind just as the cold filling process is initiated is investigated as a potential worst-case scenario. It is unlikely that the plant operator will be caught off guard by such extreme weather conditions, as a result this analysis is one performed out of curiosity.

For this analysis, five cases are investigated under the same initial conditions. The five cases include subjecting the system to rain, strong wind, a combination of rain and strong wind, a low DNI case as well as a case where no external cooling effects are present. The five cases were all simulated for an inlet molten salt temperature of 276 °C, an inlet molten salt velocity of 2 m/s and an initial receiver tube temperature of 20 °C. The inlet velocity and initial receiver tube temperature are typical conditions as obtained from previous studies and were kept constant from the test case described in Section 6.1. The minimum inlet

molten salt temperature for which full freezing of the receiver pipe does not occur for the combined rain and wind case was found to be 276 °C under these conditions.

As discussed in Section 4.3.5, the wind speed in this study was chosen to be 103 km/h (Association, n.d.) and the rain intensity is calculated from a rainfall of 50 mm/h (USGS, 2016). At wind speeds this high the heliostats would all move into their stowed positions and thus no filling would be initiated. There can, however, be a large difference in wind speed between ground level and 150 m above the ground, where the receiver would typically be located. Note also that the filling process only takes 1.75 s at an initial velocity of 2 m/s. In this timeframe a single strong gust may reach the wind speed for which this scenario is investigated. As a result, although unlikely, the described situation is a possibility. Although tested, no variation in wind speed and rain intensity was documented in this study as it adds little value to the problem evaluation. It is highly unlikely that an operator would fill the receiver just before a downpour of rain. Evaluating different wind speeds would be of interest, but the interaction between wind blowing around a single tube and wind blowing around an entire receiver is very different. As a result, using this model for such an evaluation would not add much value. Figure 6.6 is a comparison between the steel receiver tube temperatures for the no external cooling and external cooling cases. Figure 6.7 show a comparison between the molten salt temperature profiles for the no external cooling and external cooling cases.

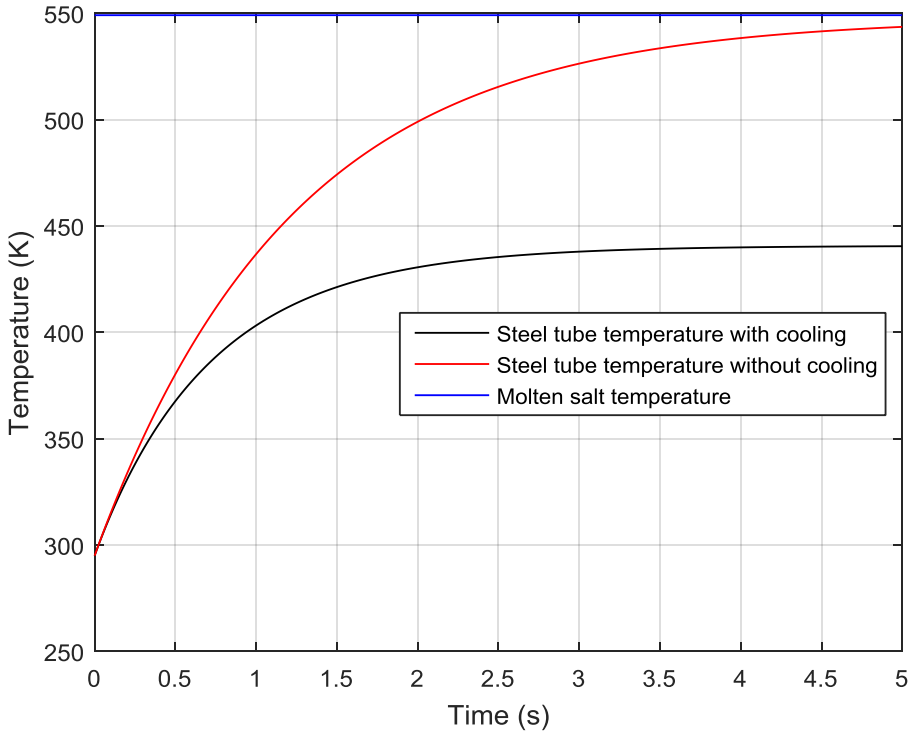

Figure 6.6: Extreme weather - molten salt and receiver tube temperatures versus time

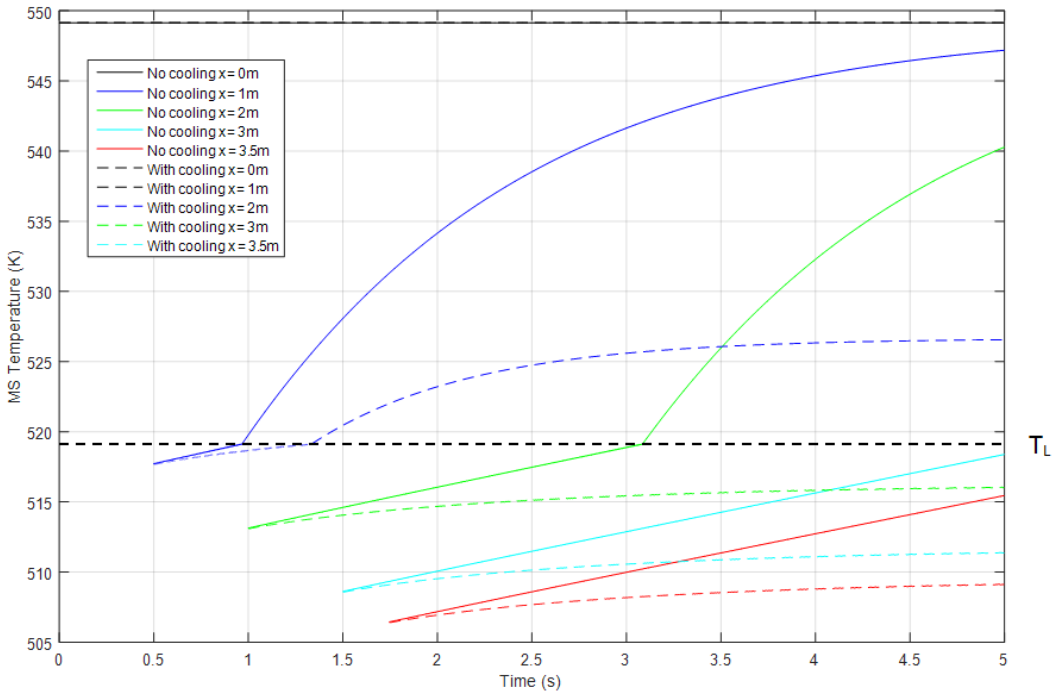

Figure 6.7: Extreme weather - molten salt temperature versus time for five distances

Both receiver tube temperatures in Figure 6.6 are at a near equilibrium temperature at 5 s. For the case when no external cooling is included, the receiver tube reaches a temperature close to that of the molten salt (which temperature is constant due to the constant inlet molten salt boundary condition) it is in contact with. For the combined rain and wind case, however, there is a temperature difference of about 210 °C as a result of the heat transfer from the receiver tube under these conditions. If the receiver is operated under these extreme conditions for a long time, this large temperature difference may result in excessive thermal stress. Note that the internal wall of the receiver tube will constantly be heated causing it to expand, while the outer wall is constantly cooled causing it to contract. This will inevitably result in severe strain in the receiver tube. Further investigation into the extent of this thermal stress is required. Until proven to be safe, cold filling under these conditions should be avoided to prevent receiver tube failure.

The temperature profiles for the cooling and no cooling cases seen in Figure 6.7 start at similar points, but the temperatures in the no cooling cases increase much more than those in the cooling cases. It is especially important to consider the molten salt temperature at the outlet of the receiver pipe as this determines the energy available to the rest of the system. Although the temperature at 3.5 m and 5 s for the no cooling case is only about 10 °C higher than the same temperature seen for the cooling cases, the trends of the 3.5 m profile for the cooling case is a concern. It seems that the 3.5 m no cooling trend will exit the mushy zone, if given a little more time, but the 3.5 m trend for the cooling case seems to have reached a near equilibrium temperature. The molten salt exiting

the receiver will therefore always be in the mushy zone. This means that it will always provide significantly less energy to the rest of the system. It can therefore be said that the receiver (not taking into account the rest of the plant) can be operated during times of rain and wind, but its efficiency will be greatly reduced.

The low DNI case was done at a DNI of 50 W/m^2 and a solar field concentration ratio of 600. The results revealed little deviation from the case without any external heat flux and is therefore not documented. The case for which only wind was considered and the case for which only rain was considered were also simulated separately. The wind was found to be the dominant cooling effect resulting in graphs similar to those for combined wind and rain. Although not as dominant, the rain also resulted in lower outlet molten salt temperatures and increased freezing over the receiver length. The graphs produced by these two cases are not included here as they are similar to those already documented in this sub-section.

From Figure 6.6 and Figure 6.7 and the accompanying discussion it can be concluded that, although full freezing of the receiver during windy and rainy conditions is avoidable under certain conditions, the receiver should not be operated during these times to prevent receiver tube failure. Further investigation into the receiver tube stress and strain may, however, yield results that contradict this statement.

6.3 Pipe Size Analysis

An analysis is done to determine the effects that changing the internal pipe diameter has on the cold filling characteristics. The internal diameter of the pipe is decreased by 10 % and 20 % and also increased by 10 % and 20 % relative to the test case scenario. The five internal diameters tested are then 12.64 mm, 14.22 mm, 15.80 mm, 17.38 mm and 18.96 mm. The wall thickness is maintained for these simulations by adjusting the outer pipe diameters accordingly. A thinker tube wall may be required, but would not affect the heat transfer analysis due to the relatively high thermal conductivity of the steel. The critical inlet molten salt temperature for which the receiver tube just does not fully freeze is determined for each case. The molten salt outlet temperature at the maximum receiver length of 3.5 m at a time of 5 s is also determined. This combination will provide an indication of the effectiveness of the filling procedure for each pipe diameter. The internal pipe areas are also plotted for comparison with these two temperatures since the pipe area is a more useful comparison than the pipe diameter. Second order trend lines are included for each of the result sets to provide a better visual comparison of how a change in internal area affects the two temperatures. The resulting graph can be seen in Figure 6.8.

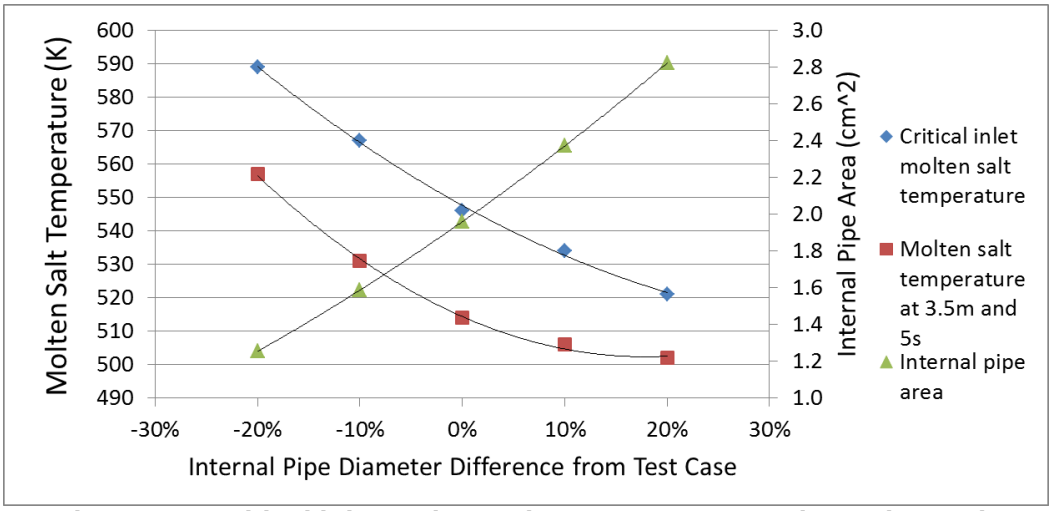

Figure 6.8: Critical inlet molten salt temperatures, outlet molten salt temperatures and internal pipe areas with trend lines for five different internal pipe diameters

From Figure 6.8 it can be seen that as the internal pipe area increases, the critical inlet temperature and the outlet temperature at 5 s both decrease. The outlet temperature is expected to decrease as the inlet temperature is decreased, which means that the internal pipe area does not necessarily affect the outlet temperature directly. By considering the trends, however, it can be seen that the outlet temperature trendline seems to start levelling out earlier than the inlet temperature trendline. It can, thus, be said that the outlet molten salt temperature will become independent of the internal pipe area if the internal pipe area is large enough. This is an indication that the internal pipe area has a direct effect on the outlet pipe temperature. The effect is that a large internal pipe diameter will result in a higher outlet molten salt temperature for a specific inlet temperature. From these observations, it can be concluded that a large internal area will improve the cold filling characteristics by increasing the outlet molten salt temperature. This is because the volume of salt in the pipe increases by a third order, while the pipe circumferential area is only increased by a second order. As a result, increasing the internal pipe area will result in more energy being carried through the pipe relative to the heat lost to the environment, resulting in a higher outlet temperature.

From Figure 6.8, it can also be seen that the critical inlet molten salt temperature decreases at a similar rate to the rate at which the internal pipe area increases. This can be said by noting that the gradients of these two properties' trend lines are similar, but negatives of one another. The minimum required inlet molten salt temperature can, thus, be lowered by increasing the internal pipe diameter. The effect of increasing the internal pipe diameter on the critical inlet molten salt temperature does, however, decrease due to the second order nature of the trends. Increasing the area of a small pipe will result in a large decrease in critical inlet molten salt temperature, but increasing the area of a large pipe will result in only a small decrease in critical inlet molten salt temperature. From these observations, it can be concluded that a large internal pipe diameter will improve

the cold filling characteristics by decreasing the critical inlet molten salt temperature.

Even though a large internal pipe diameter will result in favourable cold filling characteristics, the system as a whole should still be taken into consideration. If the internal pipe diameter is increased, the molten salt in the pipe will not be heated by the solar field to a temperature as high as it would have for a smaller diameter pipe. The advantages of increasing the internal pipe diameter for the cold filling characteristics also diminish as the internal area is increased. The relationship between the internal pipe diameter and cold filling characteristics should, therefore, not be treated in isolation. The relationship between the internal diameter and the outlet molten salt temperature while the solar field is active should also be considered, while also taking into account how these changes will affect the whole plant's efficiency. In the past, only the amount of salt passed to the outlet of the receiver panel and the temperature at the outlet were considered as thermal optimization parameters to determine the receiver pipe sizes. If cold filling is considered as an operating method for a new plant, the effects of pipe size on the cold filling characteristics should also be considered as an optimization parameter during the receiver design.

6.4 Salt Type and Property Function Analysis

The effect that choosing a different salt mixture has on the cold filling characteristics is investigated in this section. Furthermore, the Solar Salt properties proposed by Xu et al. (2017) that was used in this study will be compared to a compilation of property functions that were determined to be the best Solar Salt property functions available in literature.

6.4.1 Solar Salt and Hitec™ Salt Comparison

Hitec™ salt is investigated in terms of cold filling as a potential alternative HTF for central receiver plants instead of the more widely used Solar Salt. The Hitec™ salt properties used in this study are given in Section 4.3.1 and summarised in Table 6.1. All the temperatures given in Table 6.1 are in Kelvin. The solidus and liquidus temperature of Hitec™ salt is given by Lu et al. (2013) as 410 K and 415 K respectively. Lu et al. (2013) also states that the latent heat of fusion of Hitec™ salt is 59 kJ/kg.

Table 6.1: Hitec™ salt properties suggested in this study

Property	Function	Reference
ρ (kg/m^3)	$2356.65 - 0.748T$	(Serrano-López et al., 2013)
c_p (J/kg.K)	1560	(Serrano-López et al., 2013)
μ (kg/m.s)	$0.01538 - 0.000021T$	(Lu et al., 2013)
k (W/m.K)	0.48	(Serrano-López et al., 2013)

To compare the two salt mixtures, the molten salt temperature is plotted over the receiver length for five time steps. This temperature response is plotted in Figure

6.9 for Solar Salt and in Figure 6.10 for Hitec™ salt. Both graphs are generated using the same test case initial and boundary conditions described in Section 6.1.

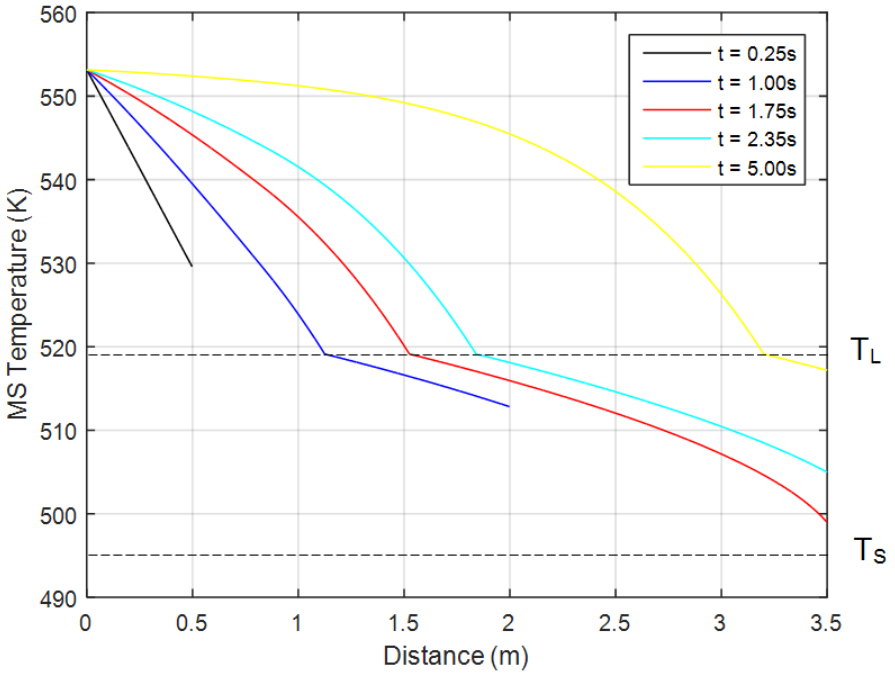

Figure 6.9: Solar Salt - molten salt temperature versus distance at different times

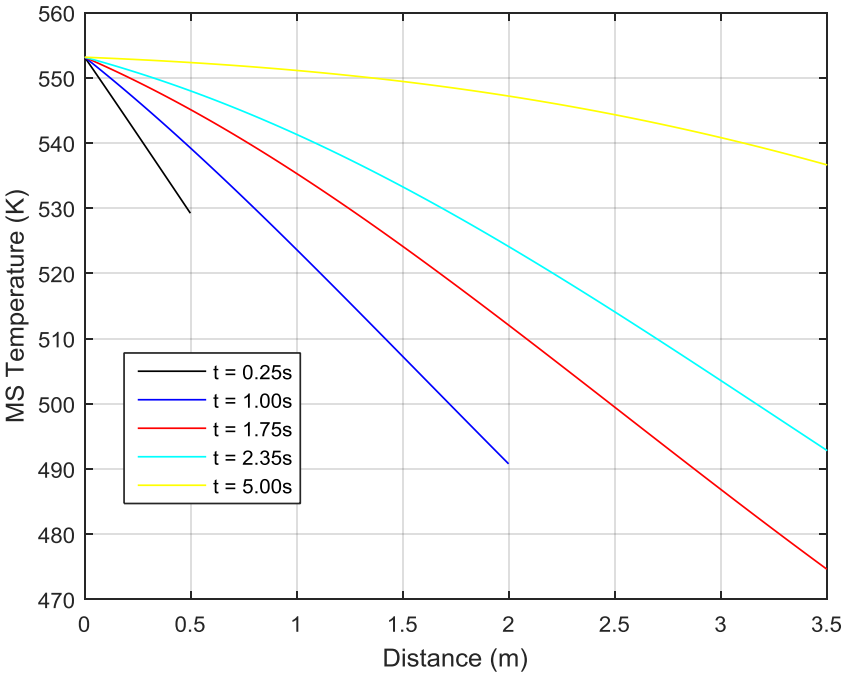

Figure 6.10: Hitec™ - molten salt temperature versus distance at different times

From Figure 6.9 it can be seen that under these test case conditions the Solar Salt partially freezes during the filling process. The Hitec™ salt, however, is still about 60 K above its liquidus temperature at its coldest point as seen in Figure 6.10. Furthermore, the Hitec™ salt reaches the receiver outlet after 5 s at a temperature of about 536 K, while the Solar Salt exits the receiver at a temperature of about 518 K at the same time. From this it can be concluded that Hitec™ salt has superior cold filling characteristics. It is, however, important to note that Hitec™ salt is significantly more expensive than Solar Salt at almost double the price, as seen in Table 2.2. Furthermore, as seen in Table 2.1, Hitec™ salt has an upper operating temperature of only 535 °C, which is 65 °C lower than the upper operating temperature of Solar Salt. Depending on the specific central receiver plant, an upper operating temperature of 535 °C may not be high enough and would then result in a Rankine efficiency loss if Hitec™ salt is used. The cold filling advantages that Hitec™ salt hold should be compared to the advantage of having the higher upper operating temperature, and thus higher potential Rankine efficiency, that Solar Salt can provide. Furthermore, the cost benefit ratio of using the more expensive Hitec™ salt should also be considered.

6.4.2 Solar Salt Property Function Comparison

The properties proposed by Xu et al. (2017) were used for the constant inlet molten salt velocity assumption validation. A review of the currently available Solar Salt properties was done in Section 2.1 and based on this review recommendations were made in Section 4.3.1 as to which Solar Salt property functions are most accurate. The Solar Salt properties used by Xu et al. (2017) and those suggested in Section 4.3.1 are compared to determine how more accurate property functions will affect the cold filling characteristic results obtained in this study. The property functions proposed by Xu et al. (2017) are documented in Table 4.1. The property functions suggested in Section 4.3.1 are summarised in Table 6.2.

Table 6.2: Solar Salt property functions suggested in this study

Property	Function	Reference
ρ (kg/m^3)	$2263.641 - 0.636T$	(Serrano-López et al., 2013)
c_p (J/kg.K)	$1396.044 + 0.172T$	(Serrano-López et al., 2013)
μ (kg/m.s)	$0.022714 - (1.200 \times 10^{-4}) + (2.281 \times 10^{-7})(T - 273.15)^2 - (1.474 \times 10^{-10})(T - 273.15)^3$	(Ferri et al., 2008)
k (W/m.K)	0.45	(Serrano-López et al., 2013)

All temperatures in Table 6.2 are given in Kelvin. Note that the density and specific heat property functions shown in Table 6.2 are no longer assumed to be constant values. The variable density is, however, not taken into account when

solving the mass balance used to calculate the inlet molten salt velocity as described in Section 4.3.2. This will result in some error, which is deemed acceptable for the purposes of this comparison. If used to predict operating conditions, variable density should be taken into account in the mass balance.

The molten salt temperature is plotted against time for five distances along the receiver length under the same conditions for both sets of property functions. The initial and boundary conditions are the same as for the test case described in Section 6.1. The resulting graph can be seen in Figure 6.11.

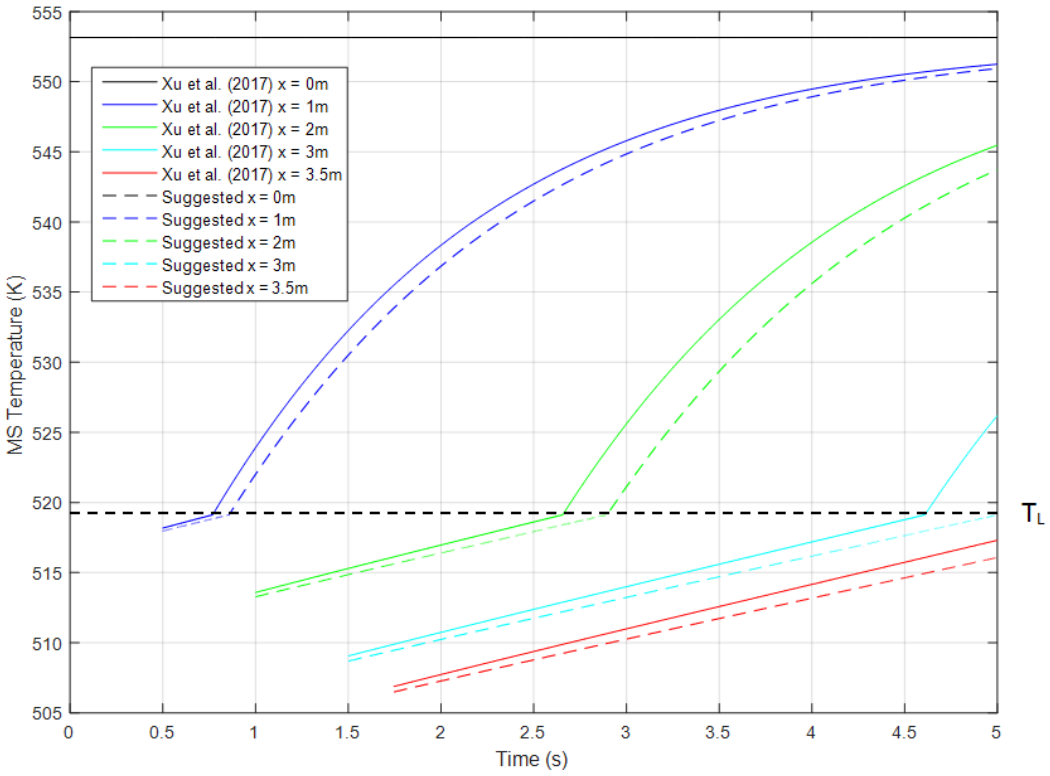

Figure 6.11: Solar Salt property comparison - molten salt temperature versus time for five distances

The results for the two property functions sets seen in Figure 6.11 are similar. Taking the point at which x = 3 m and t = 5 s as an example, the difference between the molten salt temperatures for the two property function sets is only about 0.3 %. The difference between the values obtained from the two sets of property functions are as follows: 0 % difference between viscosities, 1.70 % difference between specific heats, 21.19 % difference between thermal conductivities and 22.83 % difference between densities. With the exception of the viscosities, these differences are considerably higher than the difference in molten salt temperature. This suggests that using more accurate property functions has some effect on the results, but not so large as to discredit the use of the property functions used in this study and by Xu et al. (2017). It can also be said that the error made by assuming a constant molten salt density and constant specific heat is acceptable. By comparing the property function sets, it can be

seen that the temperatures after 5 s at the various locations along the receiver tube vary only marginally between the two graphs in most cases. At this time, it is only at 3 m where a temperature difference of more than two degrees exists between the two graphs. This larger temperature difference of about 6 K is as a result of the molten salt temperature just reaching the liquidus temperature in suggested property function set, while it exceeded the liquidus temperature 0.4 s earlier for the Xu et al. (2017) property function set resulting in a sudden increase in the temperature rate of change. It can be concluded that the properties used by Xu et al. (2017) is sufficiently accurate to model the problem with.

CHAPTER 7: CONCLUSIONS

The goal of this study was to develop a one-dimensional model capable of simulating the characteristic response of molten salt during the cold filling of a vertical receiver tube. The objectives of this study were, therefore, to select an appropriate modelling platform and develop a model that can be used for the investigation of important molten salt characteristics under various conditions. The model's credibility was then proven through verification and a two-part validation. Once proven to be credible, the model was used to investigate the molten salt characteristics, the system's response under extreme weather conditions and how changing the receiver tube size affects the cold filling characteristics, as well as evaluating the system response when using a different salt mixture and using the same salt mixture, but with different property functions.

The model was developed using MATLAB. After reviewing the available literature, it was decided to model the system using a one-dimensional flow approximation. This was later validated against two multi-dimensional models to prove the validity of this assumption. A holistic view of freezing was assumed for which the molten salt flow morphology did not need to be calculated at each point of partial freezing. Instead, a simpler method of tracking only the liquid fraction was implemented, as was done in previous studies. Previous studies have always assumed a constant heat transfer coefficient between the molten salt and the receiver tube. In this study, generally acceptable heat transfer correlations were used to calculate these heat transfer coefficients at each point. Furthermore, a worst-case scenario was considered in which the system was subjected to rain and wind during the filling process. Since, to the author's knowledge, no correlations exist for describing rain on a hot pipe; the rain was modelled using spray water cooling correlations proposed by Wendelstorf et al. (2008).

A combined time step and spatial increment verification of the model was done. A time step of 0.001 s and a spatial increment of 0.002 m were found to give sufficient accuracy. A two-part validation of the model was also conducted. The characteristic point curves produced by the model were validated against the study conducted by Liao et al. (2015) and the model's response to change was validated against the work done by Xu et al. (2017). Although some error exists between the results produced by the current study and the study done by Liao et al. (2015), the trends are similar. Therefore, it can be said that the characteristic point curves are validated. The current model and the model built by Xu et al. (2017) respond to change in the same way, but the model proposed by Xu et al. (2017) predicts that the system is far more sensitive to change than the model proposed in the current study. The trends correspond well, however, which is a more important factor to consider than point-to-point accuracy.

The responses of the molten salt temperature and liquid fraction as well as the receiver tube temperature were evaluated for a test case scenario. From the test case, it was determined that the molten salt temperature decreases with distance along the receiver tube and increases with time.

It was found that cold filling is possible during periods of heavy rain and strong wind. It was, however, noted that cold filling during these conditions will likely result in excessive stress and strain in the receiver tubes. The receiver efficiency will also greatly decrease under these conditions. From these results, it can be concluded that cold filling during extreme weather conditions may not result in receiver failure if the plant operator responds in time, but it should still be avoided to prevent damage to the receiver tubes.

The critical molten salt temperatures and receiver outlet temperatures were determined for five internal pipe diameters. From this analysis, it was found that increasing the internal receiver tube area results in a lower critical molten salt temperature and a higher molten salt temperature at the receiver outlet. These are both favourable cold filling responses. It was, however, also noted that a larger internal receiver area will result in a lower outlet temperature when the receiver is being heated by the solar field. If cold filling is considered as a filling method for a new plant, a new receiver tube size optimisation, which takes the cold filling response into account, should be done.

The cold filling characteristics of Solar Salt and Hitec^{TM} salt were compared. It was found that, under the same test case conditions, Hitec^{TM} salt does not freeze, while partial freezing occurs in the Solar Salt. Furthermore, Hitec^{TM} salt exited the receiver tube at a significantly higher temperature than the Solar Salt. Hitec^{TM} salt clearly has better cold filling characteristics than Solar Salt due to its lower freezing temperature. It was, however, noted that Hitec^{TM} salt has a significantly lower upper operating temperature than Solar Salt and is almost twice as expensive. A plant specific analysis is therefore required to determine which salt type would be better.

A comparison between the Solar Salt properties proposed by Xu et al. (2017) and those suggested in this study was also done. It was found that the error between the results is small. Therefore, it can be concluded that assuming a constant density and specific heat capacity are valid assumptions.

The model was determined to be sufficiently accurate for the purposes of the investigations conducted in this study. The results further the understanding of cold filling and highlights areas of potential receiver design and operational improvements. The good results obtained using this one-dimensional model as compared to two-dimensional and three-dimensional models indicates that it would be possible to use his model to perform many design calculations using simple models such as this one, which will save time and money.

CHAPTER 8: FUTURE WORK

The validation done in this study is sufficient for the investigations performed in this study and has been proven to be credible enough to be used for initial receiver design. Further validation against experimental or existing plant data is, however, required before these results can be used to improve on operational strategies of real plants. It would also seem that a one-dimensional model would be sufficient for initial receiver design, but a more complex two- or three-dimensional model may be required for operational improvements. Furthermore, the equations used to model the mushy zone do not accurately describe the physics and, therefore, requires further attention.

All models to date, including the current model, have assumed either a constant inlet velocity or an inlet velocity controlled by a single polynomial pumping curve. Neither of these assumptions are accurate representations of the physics. If a constant inlet velocity is assumed, it results in a constant velocity throughout the receiver tube length. It is more likely that the reduced cross-sectional area due to freezing will result in a back pressure, which in turn will result in a decrease in the inlet velocity. This phenomenon is somewhat captured by assuming a variable inlet velocity controlled by a pumping curve. The whole flow regime cannot, however, be described by a single pumping curve. The inlet velocity should be controlled by variable pumping and resistance characteristics, which receive feedback from the system regarding the current flow regime.

From the extreme weather analysis done in Section 6.2, it was noted that heavy rain and strong wind may cause excessive stress and strain in the receiver tube walls. Although this scenario is arguably not as important to consider as the receiver will likely not be operated under these harsh conditions, it can still be investigated further. A draining simulation coupled with a stress and strain analysis on the receiver tubes may, however, be of some significance. In such a study, the extent of the damage that extreme weather will cause as well as the required response time to avoid damage to the receiver tubes could be determined.

During receiver tube design, the current pipe size thermal optimisation only takes into account the amount of heat delivered to the rest of the system during periods where the receiver is being heated by the solar field. If, however, cold filling is considered as a start-up strategy for a new plant, it may be worthwhile including the receiver cold filling characteristics as an additional optimisation objective. An interesting project may be to write a multi-objective optimisation function to determine the optimum receiver pipe size for a specific plant.

Solar Salt is currently the most widely used molten salt mixture in central receiver plants. If, however, cold filling is considered as a start-up strategy for a new plant, Hitec^{TM} salt may be worth considering as Hitec^{TM} salt has far superior cold filling characteristics to Solar Salt. The trade-off is that Hitec^{TM} salt is more expensive than Solar Salt and its upper operating temperature is significantly lower than that of Solar Salt. The lower upper operating temperature is of particular concern as this may greatly reduce the plant's Rankine efficiency. It may be of some benefit to investigate these trade-offs.

APPENDIX A: MULTIPLE TUBE CALCULATIONS

The significance of the number of tubes in the receiver panel was investigated. To do this, the program accepted a number of unique receiver tubes (four unique tubes are shown in Figure A.1) and calculated the radiation heat transfer between those tubes. Each unique tube defined four tubes, which all experience the same temperature profile. Symmetry was used to reduce the computational effort of calculating each tube's temperature response. An example schematic of a receiver layout with four unique tubes can be seen in Figure A.1. Alternatively, the tubes could be set up in a staggered pattern for increased thermal absorption. For the scenarios considered in this study, heating from the solar field is not considered. As a result, the effect of using a staggered layout is negligible, especially considering that the effects of the thermal radiation between the tubes proved to be insignificant.

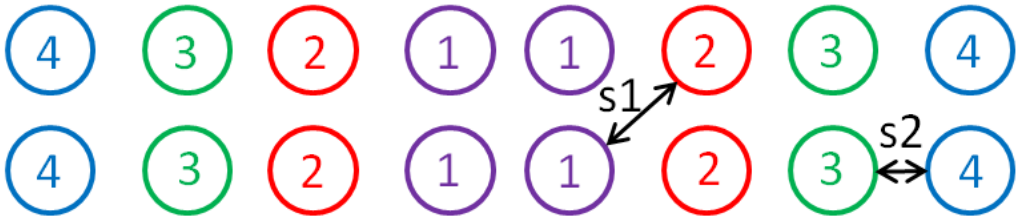

Figure A.1: Multiple tube receiver layout

For the case displayed in Figure A.1, tubes one to three are referred to as the inner tubes. They are the tubes that experience heat transfer to and from five other tubes around them. Tube 4 is referred to as the outer tube and only experience heat transfer to and from 3 other tubes around itself. In the general case, tubes one to n-1 are the inner tubes and tube n is the outer tube, with n being the total number of unique tubes. Note that in practice, the receiver will consist of a number of receiver panels arranged in a circular layout. If this is the case, no outer tubes will exist. Either the top or the bottom row of tubes will be more exposed to the environment, while the other row of tubes will be more exposed to the inside of the receiver tower.

To calculate the heat transfer coefficients between the tubes, the shape factors must first be determined. Mills & Ganesan (2015) suggests a method of determining the shape factor between long adjacent parallel cylinders of equal diameter. According to Falcone (1986), the distance between the tubes labelled s_1 in Figure A.1 is typically defined by equation (A.1).

$$s_1 = 0.1 d_{ext} \tag{A.1}$$

Following the method proposed by Mills & Ganesan (2015), the shape factor between all perpendicular tubes can be determined using equation (A.2) and equation (A.3).

$$X_1 = 1 + \frac{s_1}{d_{ext}} \tag{A.2}$$

$$F_1 = \frac{1}{\pi}\left[(X_1{}^2 - 1)^{\frac{1}{2}} + sin^{-1}\left(\frac{1}{X_1}\right) - X_1\right] \tag{A.3}$$

Since s_1 is known, the distance between tubes that are at 45° to each other can be calculated. This distance is labelled s_2 on Figure A.1 and calculated by equation (A.4).

$$s_2 = \sqrt{2\left(s_1 + d_{ext}{}^2\right)} - d_{ext} \tag{A.4}$$

Equation (A.5) and equation (A.6) are then used to calculate the shape factor between the tubes that are at 45° to each other.

$$X_2 = 1 + \frac{s_2}{d_{ext}} \tag{A.5}$$

$$F_2 = \frac{1}{\pi}\left[(X_2{}^2 - 1)^{\frac{1}{2}} + sin^{-1}\left(\frac{1}{X_2}\right) - X_2\right] \tag{A.6}$$

Now that the shape factors are known, the heat transfer coefficients for five different cases can be determined. The heat transfer coefficient between the current tube and the tube immediately to its left is given by equation (A.7).

$$h_1 = \varepsilon_s F_1 \sigma \left(T_s^{n2} + T_s^{n-1^2}\right)\left(T_s^n + T_s^{n-1}\right) \tag{A.7}$$

Where n indicates the tube number as labelled in Figure A.1. The heat transfer coefficient between the current tube and the tube immediately to its right is given by equation (A.8).

$$h_2 = \varepsilon_s F_1 \sigma \left(T_s^{n2} + T_s^{n+1^2}\right)\left(T_s^n + T_s^{n+1}\right) \tag{A.8}$$

The heat transfer coefficient between the current tube and the tube next to it in the other row is given by equation (A.9).

$$h_3 = \varepsilon_s F_1 \sigma\left(T_s^{n2} + T_s^{n2}\right)\left(T_s^n + T_s^n\right) \tag{A.9}$$

The heat transfer coefficient between the current tube and the tube left of it in the other row is given by equation (A.10).

$$h_4 = \varepsilon_s F_2 \sigma \left(T_s^{n2} + T_s^{n-1^2}\right)\left(T_s^n + T_s^{n-1}\right) \tag{A.10}$$

The heat transfer coefficient between the current tube and the tube right of it in the other row is given by equation (A.11).

$$h_5 = \varepsilon_s F_2 \sigma \left({T_s^n}^2 + {T_s^{n+1}}^2 \right) (T_s^n + T_s^{n+1}) \quad \text{(A.11)}$$

The resistances for each of these five heat transfer coefficients can then be calculated by equation (A.12) to equation (A.16) respectively.

$$R_1 = \frac{1}{2A_1 h_1} \quad \text{(A.12)}$$

$$R_2 = \frac{1}{2A_1 h_2} \quad \text{(A.13)}$$

$$R_3 = \frac{1}{2A_1 h_3} \quad \text{(A.14)}$$

$$R_4 = \frac{1}{2A_2 h_4} \quad \text{(A.15)}$$

$$R_5 = \frac{1}{2A_2 h_5} \quad \text{(A.16)}$$

Where A_1 is the unobstructed area that two perpendicular tubes can see of one another and A_2 is the unobstructed area that two tubes at 45° can see of one another.

APPENDIX B: MATLAB CODE

The code given in this Appendix is a sample for a simulation with the constant inlet velocity assumption and no external cooling or heating effects. For this case, the inlet molten salt temperature is 280 °C, the initial receiver tube temperature is 20 °C, the inlet velocity is 2 m/s and the standard internal pipe diameter of 0.0158 mm is used. Some of the result print-out-functions are included as well. Note that the velocity script given in Appendix B.4 is for the variable inlet velocity controlled by a pumping curve. The velocity script for the constant inlet molten salt velocity will simply maintain the velocity at the inlet velocity until full freezing of the pipe occurs.

MATLAB version R2015a (8.5.0.197613) was used in this study.

B.1 Main Script

```
%Main function for the receiver

%Initialise time loop counter
k = 2;

%Initialise time (s)
t(k) = 0;

%Time increments (s)
dt = 0.001;

%Time stopping condition (s)
t_end = 5;

%Gravity (m^2/s)
g = 9.81;

%Ambient temperature (K)
Ta = 20 + 273.15;

%Distance increments (m)
dz = 0.002;

%Receiver tube height (m)
Lmax = 3.5;

%Increment receiver length
Lr(1) = 0;
L_steps = ((t_end/dt)+2);
for ls = 1:L_steps
    Lr(ls+1) = Lr(ls) + dz;
end

%Receiver tube external diameter (m)
d_ext = 0.019;
```

```
%Receiver tube internal diameter (m)
d_int = 0.0158;

%Initial molten salt (MS) velocity (m/s)
v{1}(1) = 2;

%Initial receiver pressure drop (Pa)
P_r(1) = 0;

%Initial steel receiver tube temperature (K)
Ts{1}(1) = 295;
%Ts{1}(1) = 388.71;

%Initial MS temperature (K)
%Tms{1}(1) = 575;
Tms{1}(1) = 280+273.15;

%Initial solid salt temperature (K)
Tss{1}(1) = 0;

%Initial liquid fraction
f_liquid{1}(1) = 1;

%Initialize the temperature trackers outside receiver length
Tms_track{1}(1) = 0;
Tss_track{1}(1) = 0;
Ts_track{1}(1) = 0;

%Initialize the filled length closest to Lmax
Lmax_hold = 0;

%START OF TIME LOOP

%Initialize the time after the first time step
t(2) = dt;

while t(k) < t_end
%while k < 440
    %Initialise distance loop counter
    i = 1;

    %Initialise distance iteration loop counter
    iter(1) = 1;

    %Initialise receiver length
    Lr(i) = 0;

    %Initial velocity update
    v{k}(i) = v{1}(1);

    %Initialise length step tracker counter
    count1 = 2;

    %START OF DISTANCE LOOP
```

```
    while Lr(iter) <= v{1}(1)*t(k) %&& Lr(iter) <= Lmax   %Stop
when the receiver increments reach its current filled length

        if dz ~= 0
            %Update MS temperature
            if Lr(iter) <= Lmax
                if iter == 1
                    Tms{k}(1) = Tms{1}(1);
                    f_liquid{k}(1) = 1;
                else
                        if iter <= length(Tms{k})
                            if iter+1 <= length(Tms{k-1})
                                [Tms{k}(iter),  f_liquid{k}(iter),
b{k}(iter),   v_curr{k}(iter),   Lr_curr{k}(iter),   b1{k}(iter),
b2{k}(iter), b3{k}(iter)] = MSt(Ts{k-1}(iter), Tms{k-1}(iter-1),
Tms{k-1}(iter), Tms{k-1}(iter+1), v{k}(iter-1), dz, dt, d_int,
Lr(k));
                            else
                                [Tms{k}(iter),  f_liquid{k}(iter),
b{k}(iter),   v_curr{k}(iter),   Lr_curr{k}(iter),   b1{k}(iter),
b2{k}(iter), b3{k}(iter)] = MSt(Ts{k-1}(iter), Tms{k-1}(iter-1),
Tms{k-1}(iter), 0, v{k}(iter-1), dz, dt, d_int, Lr(k));
                            end
                        else
                            if Lr(iter) ~= Lmax_hold && Lmax_hold
== 0
                                if iter == 2
                                    if iter+1 <= length(Tms{k-1})
                                       [Tms{k}(iter),
f_liquid{k}(iter), b{k}(iter), v_curr{k}(iter), Lr_curr{k}(iter),
b1{k}(iter),  b2{k}(iter),  b3{k}(iter)]  =  MSt(Ts{k-1}(iter-1),
Tms{k-1}(iter-1), Tms{k-1}(iter-1), Tms{k-1}(iter+1), v{k}(iter-
1), dz, dt, d_int, Lr(k));
                                    else
                                        [Tms{k}(iter),
f_liquid{k}(iter), b{k}(iter), v_curr{k}(iter), Lr_curr{k}(iter),
b1{k}(iter),  b2{k}(iter),  b3{k}(iter)]  =  MSt(Ts{k-1}(iter-1),
Tms{k-1}(iter-1),  Tms{k-1}(iter-1),  0,  v{k}(iter-1),  dz,  dt,
d_int, Lr(k));
                                    end
                                else
                                    if iter+1 <= length(Tms{k-1})
                                        [Tms{k}(iter),
f_liquid{k}(iter), b{k}(iter), v_curr{k}(iter), Lr_curr{k}(iter),
b1{k}(iter),  b2{k}(iter),  b3{k}(iter)]  =  MSt(Ts{k-1}(iter-1),
Tms{k-1}(iter-2), Tms{k-1}(iter-1), Tms{k-1}(iter+1), v{k}(iter-
1), dz, dt, d_int, Lr(k));
                                    else
                                        [Tms{k}(iter),
f_liquid{k}(iter), b{k}(iter), v_curr{k}(iter), Lr_curr{k}(iter),
b1{k}(iter),  b2{k}(iter),  b3{k}(iter)]  =  MSt(Ts{k-1}(iter-1),
Tms{k-1}(iter-2),  Tms{k-1}(iter-1),  0,  v{k}(iter-1),  dz,  dt,
d_int, Lr(k));
                                    end
                                end
                            else
```

```
                                if iter == 2
                                    [Tms{k}(iter),
f_liquid{k}(iter), b{k}(iter), v_curr{k}(iter), Lr_curr{k}(iter),
b1{k}(iter),  b2{k}(iter),  b3{k}(iter)]  =  MSt(Ts{k-1}(iter-1),
Tms{k-1}(iter-1),     Tms{k-1}(iter-1),     Tms_track{k-1}(iter-1),
v{k}(iter-1), dz, dt, d_int, Lr(k));
                                else
                                    [Tms{k}(iter),
f_liquid{k}(iter), b{k}(iter), v_curr{k}(iter), Lr_curr{k}(iter),
b1{k}(iter),  b2{k}(iter),  b3{k}(iter)]  =  MSt(Ts{k-1}(iter-1),
Tms{k-1}(iter-2),     Tms{k-1}(iter-1),     Tms_track{k-1}(iter-1),
v{k}(iter-1), dz, dt, d_int, Lr(k));
                                end
                            end
                        end
                    end
                    Tms_track{k}(iter) = 0;
                else
                    if iter > length(Tms_track{k})
                        if iter == length(Tms{k}) + 1
                            [Tms_track{k}(iter), f_liquid{k}(iter)] =
MSt(Ts{k-1}(iter-1),    Tms{k-1}(iter-2),    Tms{k-1}(iter-1),    0,
v{k}(iter-1), dz, dt, d_int, Lr(k));
                        else
                            if iter == length(Tms{k}) + 2
                                [Tms_track{k}(iter),
f_liquid{k}(iter)]    =    MSt(Ts{k-1}(iter-2),    Tms{k-1}(iter-2),
Tms_track{k-1}(iter-1), 0, v{k}(iter-1), dz, dt, d_int, Lr(k));
                            else
                                [Tms_track{k}(iter),
f_liquid{k}(iter)]    =    MSt(Ts_track{k-1}(iter-1),    Tms_track{k-
1}(iter-2),  Tms_track{k-1}(iter-1),  0,  v{k}(iter-1),  dz,  dt,
d_int, Lr(k));
                            end
                        end
                    else
                        if iter+1 <= length(Tms_track{k-1})
                            [Tms_track{k}(iter), f_liquid{k}(iter)] =
MSt(Ts_track{k-1}(iter),    Tms_track{k-1}(iter-1),    Tms_track{k-
1}(iter),  Tms_track{k-1}(iter+1),  v{k}(iter-1),  dz,  dt,  d_int,
Lr(k));
                        else
                            [Tms_track{k}(iter), f_liquid{k}(iter)] =
MSt(Ts_track{k-1}(iter),    Tms_track{k-1}(iter-1),    Tms_track{k-
1}(iter), 0, v{k}(iter-1), dz, dt, d_int, Lr(k));
                        end
                    end
                end


                if f_liquid{k}(iter) < 1
                    %Update solid salt temperature
                    if Lr(iter) <= Lmax
                        if iter <= length(Tss{k})
```

```
                        Tss{k}(iter)  =  SS(Tss{k-1}(iter),  Ts{k-
1}(iter), Tms{k-1}(iter-1), Tms{k-1}(iter), v{k}(iter-1), dz, dt,
d_int, Lr(k));
                    else
                        if iter == 2
                            Tss{k}(iter)  =  SS(Tss{k-1}(iter-1),
Ts{k-1}(iter-1), Tms{k-1}(iter-1), Tms{k-1}(iter-1), v{k}(iter-1),
dz, dt, d_int, Lr(k));
                        else
                            Tss{k}(iter)  =  SS(Tss{k-1}(iter-1),
Ts{k-1}(iter-1), Tms{k-1}(iter-2), Tms{k-1}(iter-1), v{k}(iter-1),
dz, dt, d_int, Lr(k));
                        end
                    end
                    Tss_track{k}(iter) = 0;
                else
                    if iter == length(Tss{k}) + 1
                        Tss_track{k}(iter) = SS(Tss{k-1}(iter-1),
Ts{k-1}(iter-1), Tms{k-1}(iter-2), Tms{k-1}(iter-1), v{k}(iter-1),
dz, dt, d_int, Lr(k));
                    else
                        if iter == length(Tss{k}) + 2
                            Tss_track{k}(iter) = SS(Tss{k-1}(iter-
2),  Ts{k-1}(iter-2),  Tms{k-1}(iter-2),  Tms_track{k-1}(iter-1),
v{k}(iter-1), dz, dt, d_int, Lr(k));
                        else
                            Tss_track{k}(iter)  =  SS(Tss_track{k-
1}(iter-1),     Ts_track{k-1}(iter-1),     Tms_track{k-1}(iter-2),
Tms_track{k-1}(iter-1), v{k}(iter-1), dz, dt, d_int, Lr(k));
                        end
                    end
                end
            else
                if Lr(iter) <= Lmax
                    Tss{k}(iter) = 0;
                    Tss_track{k}(iter) = 0;
                else
                    Tss_track{k}(iter) = 0;
                end
            end

            %Update steel receiver tube temperature
            if Lr(iter) <= Lmax
                if iter <= length(Ts{k-1})
                    if iter == 1
                        Ts{k}(iter)  =  Steelt(Ta,  Ts{k-1}(iter),
Tms{k}(iter),  Tss{k}(iter),  dz,  v{k-1}(iter),  dt,  d_ext,  d_int,
Lr(k));
                    else
                        Ts{k}(iter)  =  Steelt(Ta,  Ts{k-1}(iter),
Tms{k}(iter),  Tss{k}(iter),  dz,  v{k}(iter-1),  dt,  d_ext,  d_int,
Lr(k));
                    end
                else
```

```
                    Ts{k}(iter)   =   Steelt(Ta,   Ts{k-1}(iter-1),
Tms{k}(iter),  Tss{k}(iter),  dz,  v{k}(iter-1),  dt,  d_ext,  d_int,
Lr(k));
                end
                Ts_track{k}(iter) = 0;
            else
                if iter == length(Ts{k}) + 1
                    Ts_track{k}(iter)  =  Steelt(Ta,  Ts{k-1}(iter-
1), Tms_track{k}(iter), Tss_track{k}(iter), dz, v{k}(iter-1), dt,
d_ext, d_int, Lr(k));
                else
                    if iter == length(Ts{k}) + 2
                        Ts_track{k}(iter)   =   Steelt(Ta,   Tss{k-
1}(iter-2), Ts{k-1}(iter-2), Tss_track{k}(iter), dz, v{k}(iter-1),
dt, d_ext, d_int, Lr(k));
                    else
                        Ts_track{k}(iter) = Steelt(Ta, Ts_track{k-
1}(iter-1), Tms_track{k}(iter), Tss_track{k}(iter), dz, v{k}(iter-
1), dt, d_ext, d_int, Lr(k));
                    end
                end
            end

            %Update the MS velocity
            i_length = length(Tms{k});
            i_length2 = length(Tms_track{k});

            if iter == 1
                if v{k-1}(iter) == 0
                    v{k}(iter) = 0;
                    FREEZE{k}(iter) = 1;
                else
                    FREEZE{k}(iter) = 0;
                end
            else
                if v{k}(iter-1) == 0
                    v{k}(iter) = 0;
                    FREEZE{k}(iter) = 1;
                else
                    FREEZE{k}(iter) = 0;
                end
            end

            if FREEZE{k}(iter) == 1
                v{k}(iter) = 0;
            else
                if iter-2 > 0
                    if Tms_track{k}(i_length2) == 0
                        v{k}(iter)  =  Velocity(Tms{k}(i_length-1),
Tms{k}(i_length), v{k}(iter-1), d_int, Lr(k));
                    else
                        if Tms_track{k}(i_length2-1) == 0
                            v{k}(iter) = Velocity(Tms{k}(i_length-
1), Tms_track{k}(i_length2), v{k}(iter-1), d_int, Lr(k));
                        else
```

```
                            v{k}(iter)                                  =
Velocity(Tms_track{k}(i_length2-1),       Tms_track{k}(i_length2),
v{k}(iter-1), d_int, Lr(k));
                        end
                    end
                else
                    if iter == 1
                        v{k}(iter)   =   Velocity(Tms{k}(i_length),
Tms{k}(i_length), v{k-1}(iter), d_int, Lr(k));
                    else
                        v{k}(iter)   =   Velocity(Tms{k}(i_length),
Tms{k}(i_length), v{k}(iter-1), d_int, Lr(k));
                    end
                end

                if v{k}(iter) < 0.02
                    v{k}(iter) = 0;                    %Velocity is
small enough to be approximated as zero
                end
            end

            if iter <= length(Ts{k})
                if Ts{k}(iter) > Tms{1}(1)
                    Ts{k}(iter)
                end
            end

            %Define the filled length closest to Lmax
            if Lr(iter+1) > Lmax
                Lmax_hold = Lr(iter);
            end

            %Increment distance loop counters
            i = i+1;
            iter = iter+1;
        else
            %Increment distance loop counter
            i = i+1;
        end
    end

    %Update the pressure drop in the receiver
    if Tms_track{k}(i_length2) == 0
        P_r(k) = PressureR(Tms{k}(i_length), v{k}(iter-1), d_int,
max(Lr));
    else
        P_r(k) = PressureR(Tms_track{k}(i_length2), v{k}(iter-1),
d_int, max(Lr));
    end

    %Increment time
    t(k+1) = t(k) + dt;

    %Increment time loop counter
    k = k + 1
end
```

```
toc

%Number of time steps per distance step
dtdz = ((Lmax/v{1}(1))/dt)/(Lmax/dz)


%RESULTS


%Plot the receiver filled length vs time
figure
FT = Lmax/v{1}(1);
FTdt = FT/dt;
ZZ = FTdt/dtdz;
for i = 1:ZZ+1
    t_Temp(i) = t(1+(dtdz*(i-1)));
end
plot(t_Temp, Lr(1:length(t_Temp)), 'k-')
title('Receiver Filled Length vs Time')
xlabel('Time (s)')
ylabel('Receiver Filled Length (m)')
grid

%Plot the MS temperature versus time at 0m
for i=1:length(t)-1
    T_MS(i) = Tms{i}(1);
end
figure
plot(t(1:length(t)-1), T_MS,'k-')
title('Molten Salt Temperature vs Time (x=0m)')
xlabel('Time (s)')
ylabel('Molten Salt Temperature (K)')
grid

%Plot the steel receiver tube temperature versus time at 0m
for i=1:length(t)-1
    T_S(i) = Ts{i}(1);
end
figure
plot(t(1:length(t)-1), T_S,'k-')
title('Steel Receiver Tube Temperature vs Time (x=0m)')
xlabel('Time (s)')
ylabel('Steel Receiver Tube Temperature (K)')
grid

%Plot the steel receiver tube and molten salt temperatures versus
time at 0m
figure
plot(t(1:length(t)-1), T_S,'k-')
hold on
plot(t(1:length(t)-1), T_MS,'b-')
legend('Steel tube temperature', 'Molten salt temperature')
%title('Compare Steel Receiver Tube and Molten Salt Temperature vs
Time (x=0m)')
xlabel('Time (s)')
```

```
ylabel('Temperatures (K)')
grid

%Plot liquid fraction versus distance at t = 1.75s
t1 = 1.75/dt;
L1 = length(v{t1});
figure
plot(Lr(1:L1), f_liquid{t1}(1:L1),'k-')
%title('Liquid Fraction vs Distance (t=1.75s)')
xlabel('Distance (m)')
ylabel('Liquid Fraction')
grid

%Plot MS temperature vs time at different distances
yy = find(Lr >= 0, 1);
for i=1:length(t)-1
    if yy > size(Tms{i})
        T_MS(i) = Tms{1}(1);
    else
        T_MS(i) = Tms{i}(yy);
    end
end
figure
plot(t(yy:length(t)-2), T_MS(yy:length(t)-2),'k-')
%title('MS Temperature vs Time at different distances')
xlabel('Time (s)')
ylabel('MS Temperature (K)')
grid
hold on
if max(Lr) >= 1
    yy = find(Lr >= 1, 1);
    for i=1:length(t)-1
        if yy > size(Tms{i})
            T_MS(i) = Tms{1}(1);
        else
            T_MS(i) = Tms{i}(yy);
        end
    end
    if min(T_MS) == 0
        zz = max(find(T_MS==0)) + 1;
    else
        zz = 0;
    end
    pp = max(yy, zz);
    if pp == zz
        disp('Freezes at 1m')
    end
    plot(t(pp:length(t)-2), T_MS(pp:length(t)-2),'b-')
    hold on
end
if max(Lr) >= 2
    yy = find(Lr >= 2, 1);
    for i=1:length(t)-1
        if yy > size(Tms{i})
            T_MS(i) = Tms{1}(1);
        else
```

```
            T_MS(i) = Tms{i}(yy);
        end
    end
    if min(T_MS) == 0
        zz = max(find(T_MS==0)) + 1;
    else
        zz = 0;
    end
    pp = max(yy, zz);
    if pp == zz
        disp('Freezes at 2m')
    end
    plot(t(pp:length(t)-2), T_MS(pp:length(t)-2),'g-')
    hold on
end
if max(Lr) >= 3
    yy = find(Lr >= 3, 1);
    for i=1:length(t)-1
        if yy > size(Tms{i})
            T_MS(i) = Tms{1}(1);
        else
            T_MS(i) = Tms{i}(yy);
        end
    end
    if min(T_MS) == 0
        zz = max(find(T_MS==0)) + 1;
    else
        zz = 0;
    end
    pp = max(yy, zz);
    if pp == zz
        disp('Freezes at 3m')
    end
    plot(t(pp:length(t)-2), T_MS(pp:length(t)-2),'c-')
    hold on
end
if max(Lr) >= 3.49
    yy = find(Lr >= 3.49, 1);
    for i=1:length(t)-1
        if yy > size(Tms{i})
            T_MS(i) = Tms{1}(1);
        else
            T_MS(i) = Tms{i}(yy);
        end
    end
    if min(T_MS) == 0
        zz = max(find(T_MS==0)) + 1;
    else
        zz = 0;
    end
    pp = max(yy, zz);
    if pp == zz
        disp('Freezes at 3.5m')
    end
    plot(t(pp:length(t)-2), T_MS(pp:length(t)-2),'r-')
end
```

```
legend('x = 0m', 'x = 1m', 'x = 2m', 'x = 3m', 'x = 3.5m')

%Plot liquid fraction vs time at different distances
yy = find(Lr >= 0, 1);
for i=1:length(t)-1
    if yy > size(f_liquid{i})
        f_Liquid(i) = f_liquid{1}(1);
    else
        f_Liquid(i) = f_liquid{i}(yy);
    end
end
figure
plot(t(1:length(t)-2), f_Liquid(1:length(t)-2),'k-')
%title('Liquid Fraction vs Time at different distances')
xlabel('Time (s)')
ylabel('Liquid Fraction')
grid
hold on
if max(Lr) >= 1
    yy = find(Lr >= 1, 1);
    for i=1:length(t)-1
        if yy > size(f_liquid{i})
            f_Liquid(i) = f_liquid{1}(1);
        else
            f_Liquid(i) = f_liquid{i}(yy);
        end
    end
    nn = find(f_Liquid < 1, 1);
    plot(t(nn:length(t)-2), f_Liquid(nn:length(t)-2),'b-')
    hold on
end
if max(Lr) >= 2
    yy = find(Lr >= 2, 1);
    for i=1:length(t)-1
        if yy > size(f_liquid{i})
            f_Liquid(i) = f_liquid{1}(1);
        else
            f_Liquid(i) = f_liquid{i}(yy);
        end
    end
    nn = find(f_Liquid < 1, 1);
    plot(t(nn:length(t)-2), f_Liquid(nn:length(t)-2),'g-')
    hold on
end
if max(Lr) >= 3
    yy = find(Lr >= 3, 1);
    for i=1:length(t)-1
        if yy > size(f_liquid{i})
            f_Liquid(i) = f_liquid{1}(1);
        else
            f_Liquid(i) = f_liquid{i}(yy);
        end
    end
    nn = find(f_Liquid < 1, 1);
    plot(t(nn:length(t)-2), f_Liquid(nn:length(t)-2),'c-')
    hold on
```

```
end
if max(Lr) >= 3.49
    yy = find(Lr >= 3.49, 1);
    for i=1:length(t)-1
        if yy > size(f_liquid{i})
            f_Liquid(i) = f_liquid{1}(1);
        else
            f_Liquid(i) = f_liquid{i}(yy);
        end
    end
    nn = find(f_Liquid < 1, 1);
    plot(t(nn:length(t)-2), f_Liquid(nn:length(t)-2),'r-')
end
legend('x = 0m', 'x = 1m', 'x = 2m', 'x = 3m', 'x = 3.5m')

%Plot molten salt temperature vs distance at different times
t3 = 0.25/dt;
L3 = length(Tms{t3});
if min(Tms{t3}) == 0
    zz = min(find(Tms{t3}==0)) - 1;
else
    zz = L3+1;
end
pp = min(L3, zz);
if pp == zz
    disp('Freezes at 0.25s')
end
figure
plot(Lr(1:pp), Tms{t3}(1:pp),'k-')
%title('Molten Salt Temperature vs Distance')
xlabel('Distance (m)')
ylabel('MS Temperature (K)')
grid
hold on
t4 = 1/dt;
L4 = length(Tms{t4});
if min(Tms{t4}) == 0
    zz = min(find(Tms{t4}==0)) - 1;
else
    zz = L4+1;
end
pp = min(L4, zz);
if pp == zz
    disp('Freezes at 1.00s')
end
plot(Lr(1:pp), Tms{t4}(1:pp),'b-')
hold on
t5 = 1.75/dt;
L5 = length(Tms{t5});
if min(Tms{t5}) == 0
    zz = min(find(Tms{t5}==0)) - 1;
else
    zz = L5+1;
end
pp = min(L5, zz);
if pp == zz
```

```
    disp('Freezes at 1.75s')
end
plot(Lr(1:pp), Tms{t5}(1:pp),'r-')
hold on
t6 = 2.35/dt;
L6 = length(Tms{t6});
if min(Tms{t6}) == 0
    zz = min(find(Tms{t6}==0)) - 1;
else
    zz = L6+1;
end
pp = min(L6, zz);
if pp == zz
    disp('Freezes at 2.35s')
end
plot(Lr(1:pp), Tms{t6}(1:pp),'c-')
hold on
t7 = 5/dt;
L7 = length(Tms{t7});
if min(Tms{t7}) == 0
    zz = min(find(Tms{t7}==0)) - 1;
else
    zz = L7+1;
end
pp = min(L7, zz);
if pp == zz
    disp('Freezes at 5.00s')
end
plot(Lr(1:pp), Tms{t7}(1:pp),'y-')
hold on
legend('t = 0.25s', 't = 1.00s', 't = 1.75s', 't = 2.35s', 't =
5.00s')

%Plot steel receiver tube temperature and molten salt temperature
vs time at x=1m
xx = find(Lr >= 1, 1);
for i=1:length(t)-1
    if xx > size(Ts{i})
        T_S(i) = Ts{1}(1);
    else
        T_S(i) = Ts{i}(xx);
    end
end
figure
plot(t(1:length(t)-2), T_S(1:length(t)-2),'k-')
hold on
yy = find(Lr >= 1, 1);
for i=1:length(t)-1
    if yy > size(Tms{i})
        T_MS(i) = Tms{1}(1);
    else
        T_MS(i) = Tms{i}(yy);
    end
end
plot(t(1:length(t)-2), T_MS(1:length(t)-2),'b-')
```

```
%title('Steel Receiver Tube Temperature and MS Temperature vs Time
(x=1m)')
xlabel('Time (s)')
ylabel('Temperature (K)')
grid
legend('Steel Receiver Tube Temperature', 'MS Temperature')
```

B.2 Molten Salt Property Function Scripts

```
%Specific heat of molten salt
function y = cpMS(T)
%y = 1396 + 0.172*T;         %(Suárez et al. 2015)

y = 1510;                   %(Xu et al. 2013) VALIDATION

%y = 1.424*1000;             %(Wu et al. 2012)

%y = 0.98*1396.044 + 0.172*T;     %(Serrano-López et al., 2013)
SOLAR SALT (Best)

%y = 1560;                   %(Serrano-López et al., 2013) Hitec

%T = T - 273.15;
%y = 1443 + 0.172*T;         %(Ferri et al., 2008) SOLAR SALT
end

%Thermal conductivity of molten salt
function y = kMS(T)
%y = 0.3911 + 0.00019*T;        %(Suárez et al. 2015)

y = 0.571;                    %(Xu et al. 2013) VALIDATION

%T = T - 273.15;
%y = 0.586 - 0.00064*T;        %(Wu et al. 2012)

%y = 0.45;        %(Serrano-López et al., 2013) SOLAR SALT (Best)

%y = 0.48;        %(Serrano-López et al., 2013) Hitec

%y = 0.571;        %(Liao et al., 2014) Hitec

%y = 0.78 + ((-1.25*(10^-3))*T) + ((1.6*(10^-6))*(T^2));
%(Santini et al., 1984) Hitec

%T = T - 273.15;
%y = 0.443 + (1.9*(10^-4))*T;      %(Ferri et al., 2008) SOLAR SALT
end

%Density of molten salt
function y = rhoMS(T)
%y = 2263.6 - 0.636*T;        %(Suárez et al., 2015)

%y = 1940 + 40*f_s;           %(Lu et al., 2013)
```

```
%y = 1940;                    %(Lu et al. 2013) VALIDATION

y = 2000;                    %(Xu et al. 2016) VALIDATION

%T = T - 273.15;
%y = 2083.5 - 0.748*T;        %(Wu et al., 2012)      Hitec

%y = 2263.641 -0.636*T;       %(Serrano-López et al., 2013) SOLAR
SALT (Best)

%y = 2279.799 - 0.7324*T;     %(Serrano-López et al., 2013) Hitec

%T = T - 273.15;
%y = 2090 - 0.636*T;          %(Ferri et al., 2008) SOLAR SALT
end

%Dynamic viscosity of molten salt
function y = uMS(T)
%y = (-0.000021*T) + 0.01538;                %(Lu et al. 2013)
VALIDATION

%T = T - 273.15;
%y = (-0.2149*exp(-T/57.05)) + 0.0017;       %(Wu et al. 2012)

%T = T - 273.15;
%y = 0.075439 - ((2.77*(10^-4))*T) + ((3.49*(10^-7))*(T^2)) -
((1.474*(10^-10))*(T^3));  %(Serrano-López et al., 2013) SOLAR
SALT

%T = T - 273.15;
%y = exp(-4.343 - 2.0143*(log(T) - 5.011));  %(Serrano-López et
al., 2013) Hitec

T = T - 273.15;
y = 0.022714 - (1.2*(10^-4)*T) + (2.281*(10^-7)*(T^2)) -
(1.474*(10^-10)*(T^3));        %(Xu et al. 2016) VALIDATION

% T = T - 273.15;
% y = 0.95*0.022714 - (1.2*(10^-4)*T) + (2.281*(10^-7)*(T^2)) -
(1.474*(10^-10)*(T^3));        %(Ferri et al., 2008) SOLAR SALT
(Best)
end
```

B.3 Air Property Function Scripts

```
%Thermal conductivity of air
function y = kAIR(T)
% T = T - 273.15;
% y = 0.00007186*T + 0.02423182;          %(Best)

y = 0.0242;                   %(Lu et al. 2013) VALIDATION
end

%Prandtl Number for air
```

```
function y = PrAIR(T)
T = T - 273.15;
y = -0.0000000000000239*(T^6) + 0.0000000000133714*(T^5) -
0.0000000027046608*(T^4) + 0.0000002374617563*(T^3) -
0.0000088907148026*(T^2) + 0.0000123339100639*T +
0.7149615390269160; %(Best)
end

%Kinematic Viscosity of Air
function y = vAIR(T)
T = T - 273.15;
y = 0.00009237*(T^2) + 0.08861772*T + 13.28419580;
y = y*(10^-6);                                          %(Best)
end
```

B.4 Velocity Sub-function Script

```
%Velocity sub-function
function [v_new, b, b1, b2, b3, b4, b5, Tms_prev, Tms_curr, Lr] =
Velocity(Tms_prev, Tms_curr, v, d_int, Lr)
%Gravity
g = 9.81;

%Molten Salt Liquidus Temperature
T_L = 246 + 273.15;

%Molten Salt Solidus Temperature
T_S = 221 + 273.15;

%Length of horizontal section of pipe (m)
Lh = 3.25;

%Molten salt phase
if Tms_curr > T_L
    f_liquid = 1;
else if Tms_curr >= T_S && Tms_curr <= T_L
        f_liquid = (Tms_curr - T_S)/(T_L - T_S);
    else
        f_liquid = 0;
    end
end

%Previous molten salt phase
if Tms_prev > T_L
    f_liquid_prev = 1;
else if Tms_prev >= T_S && Tms_prev <= T_L
        f_liquid_prev = (Tms_prev - T_S)/(T_L - T_S);
    else
        f_liquid_prev = 0;
    end
end

%Receiver tube cross sectional area (m^2)
A_cs = f_liquid*pi*(d_int/2)^2;
```

```
%Receiver tube previous cross sectional area (m^2)
A_cs_prev = f_liquid_prev*pi*(d_int/2)^2;

%Receiver tube cross sectional area with no freezing (m^2)
A_cs1 = pi*(d_int/2)^2;

A_cs2 = A_cs1*1;
    v_temp = 3.5;
    v_new = 0;
    while v_temp > 0 && (abs(v_new - v_temp))/v_new > 0.001
        %The molten salt (MS) mass flow rate (kg/s)
        m_dot = rhoMS(Tms_curr)*v_temp*A_cs;

        %Reynolds number
        Re = ((m_dot/A_cs)*d_int)/uMS(Tms_curr);

        %Horizontal section friction factor
        if Re ~= 0
            f_h = 0.3164/(Re^0.25);
        else
            Re_temp = 1;
            f_h = 0.3164/(Re_temp^0.25);
        end

        % %Receiver tube friction factor
        if Re ~= 0
            f_r = 0.3164/(Re^0.25);
        else
            Re_temp = 1;
            f_r = 0.3164/(Re_temp^0.25);
        end

        %Local pressure loss coefficient
        zeta = 0.29;                        %(Liao et al., 2015)

        %Pressure balance to find the new velocity (m/s)
        b = 4000 + (f_h*(Lh/d_int)*(rhoMS(Tms_curr)/2)) +
(zeta*(rhoMS(Tms_curr)/2)) +
(A_cs2/A_cs)*((f_r*(Lr/d_int)*(rhoMS(Tms_curr)/2)) +
((rhoMS(Tms_curr)*g*Lr)/(v_temp^2))) + (rhoMS(Tms_curr)/2) +
((((rhoMS(Tms_prev)*v*A_cs_prev)^2)/(rhoMS(Tms_prev)*v_temp^2)) -
(((rhoMS(Tms_curr)*A_cs)^2)/rhoMS(Tms_curr)));
        b1 = (f_h*(Lh/d_int)*(rhoMS(Tms_curr)/2));
        b2 = (zeta*(rhoMS(Tms_curr)/2));
        b3 = (A_cs2/A_cs)*((f_r*(Lr/d_int)*(rhoMS(Tms_curr)/2)) +
((rhoMS(Tms_curr)*g*Lr)/(v_temp^2)));
        b4 = (rhoMS(Tms_curr)/2);
        b5 =
((((rhoMS(Tms_prev)*v*A_cs_prev)^2)/(rhoMS(Tms_prev)*v_temp^2)) -
(((rhoMS(Tms_curr)*A_cs)^2)/rhoMS(Tms_curr)));

        v_temp = v_temp - 0.0001;
```

```
        if f_liquid == 0
            v_new = 0;
        else
            v_new = sqrt((105000)/b);
        end
    end
end
```

B.5 Pressure Sub-Function Script

```
%Receiver pressure drop

function Pr_new = PressureR(Tms, v, d_int, Lr)
%Gravity
g = 9.81;

%Molten Salt Freezing Temperature
T_L = 246 + 273.15;

%Molten Salt Melting Temperature
T_S = 222 + 273.15;

%Molten salt phase
if Tms > T_L
    f_liquid = 1;
else if Tms >= T_S && Tms <= T_L
        f_liquid = (Tms - T_S)/(T_L - T_S);
    else
        f_liquid = 0;
    end
end

%Receiver tube cross sectional area (m^2)
A_cs = f_liquid*pi*(d_int/2)^2;

%Receiver tube cross sectional area with no freezing (m^2)
A_cs1 = pi*(d_int/2)^2;

%The molten salt (MS) mass flow rate (kg/s)
m_dot = rhoMS(Tms)*v*A_cs;

%Reynolds number
Re = ((m_dot/A_cs)*d_int)/uMS(Tms);

%Receiver tube friction factor
if Re ~= 0
    f_r = 0.3164/(Re^0.25);
else
    Re_temp = 1;
    f_r = 0.3164/(Re_temp^0.25);
end

%New receiver pressure (Pa)
if f_liquid == 0
    Pr_new = 0;
```

```
else
    Pr_new = (A_cs1/A_cs)*((f_r*(Lr/d_int)*(rhoMS(Tms)/2))*(v^2) +
(rhoMS(Tms)*g*Lr));
end
end
```

B.6 Molten Salt Sub-function Script

```
%Molten salt (MS) time sub-function

function [Tms_new, f_liquid_curr, b, v, Lr, b1, b2, b3] = MSt(Ts,
Tms_prev, Tms_curr, Tms_next, v, dz, t, d_int, Lr)
%Molten Salt Liquidus Temperature
T_L = 246 + 273.15;

%Molten Salt Solidus Temperature
T_S = 222 + 273.15;

%Molten salt phase
if Tms_prev > T_L
    f_liquid_prev = 1;
else if Tms_prev >= T_S && Tms_prev <= T_L
        f_liquid_prev = (Tms_prev - T_S)/(T_L - T_S);
    else
        f_liquid_prev = 0;
    end
end

%Molten salt phase
if Tms_curr > T_L
    f_liquid_curr = 1;
else if Tms_curr >= T_S && Tms_curr <= T_L
        f_liquid_curr = (Tms_curr - T_S)/(T_L - T_S);
    else
        f_liquid_curr = 0;
    end
end

if f_liquid_curr == 0
    Tms_new = 0;
    b = 0;
    b1 = 0;
    b2 = 0;
    b3 = 0;
else
    %Receiver tube cross sectional area (m^2)
    A_cs = f_liquid_curr*pi*(d_int/2)^2;

    %Receiver tube internal circumferential area (m^2)
    A_int = sqrt(f_liquid_curr)*d_int*pi*dz;

    %The molten salt (MS) mass flow rate (kg/s)
    m_dot = rhoMS(Tms_curr)*v*A_cs;

    %Latent heat of fusion (J/kg)
```

```
    Lh = 161000;                        %(Archimede, n.d.)

    %Density
    rho_MS = rhoMS(Tms_curr);

    %MS specific heat
    cp_MS = cpMS(Tms_curr);

    %Volume of MS in the control volume
    V_MS = A_cs*dz;

    if f_liquid_curr == 1
        %Heat transfer coefficient between the steel receiver tube
and the MS
        if A_cs == 0
            A_cs = 0.01*pi*(d_int/2)^2;
        end
        Re = ((m_dot/A_cs)*d_int)/uMS(Tms_curr);
        f = 0.3164/(Re^0.25);
        PrMS = (cpMS(Tms_curr)*uMS(Tms_curr))/kMS(Tms_curr);
        if Re > 1500
            Nu     =     ((f/8)*(Re     -     1000)*PrMS)/(1     +
12.7*((f/8)^0.5)*((PrMS^(2/3)) - 1));
        else
            x_star = Lr/(d_int*Re*PrMS);
            Nu = 1.076*(x_star^(-1/3)) - 1.064;
            if Nu < 4.364
                Nu = 4.364;
            end
        end
        hsms = (kMS(Tms_curr)/d_int)*Nu;
    end

    if f_liquid_curr < 1
        %Convection heat transfer coefficient between the liquid
and solid salt
        if A_cs == 0
            A_cs = 0.01*pi*(d_int/2)^2;
        end
        Re = ((m_dot/A_cs)*d_int)/uMS(Tms_curr);
        f = 0.3164/(Re^0.25);
        PrMS = (cpMS(Tms_curr)*uMS(Tms_curr))/kMS(Tms_curr);
        if Re > 1500
            Nu     =     ((f/8)*(Re     -     1000)*PrMS)/(1     +
12.7*((f/8)^0.5)*((PrMS^(2/3)) - 1));
        else
            x_star = Lr/(d_int*Re*PrMS);
            Nu = 1.076*(x_star^(-1/3)) - 1.064;
            if Nu < 4.364
                Nu = 4.364;
            end
        end
        r_ints = sqrt(f_liquid_curr)*(d_int/2);
        hmsLmsS = (kMS(Tms_curr)/(r_ints*2))*Nu;

        %Conduction heat transfer in the solid salt
```

```
        Rsalt = (log((d_int/2)/r_ints))/(2*pi*kMS(T_S)*dz);
    end

    %Latent fusion heat energy change
    Q = (Lh*rhoMS(Tms_curr)/t)*(f_liquid_curr - f_liquid_prev);

    if f_liquid_curr == 1
        %Constant b
        if dz == 0
            b1 = 0;
        else
            b1 = (hsms*A_int)/(rho_MS*V_MS*cp_MS);
        end
        if v~= 0
            b2 = (Tms_prev - Tms_curr)/(Tms_curr - Ts);
        else
            b2 = 0;
        end
        b3 = (Q*t)/(rho_MS*cp_MS*(Tms_curr - Ts));

        b = b1 + b2 + b3;

        %Update molten salt temperature
        Tms_new = (Tms_curr - Ts)*exp(-b*t) + Ts;
    end

    if f_liquid_curr < 1
        %Constant b
        if dz == 0
            b1 = 0;
        else
            b1 = (hmsLmsS*A_int)/(rho_MS*V_MS*cp_MS);
        end
        if v~= 0
            b2 = (Tms_prev - Tms_curr)/(Tms_curr - T_S);
        else
            b2 = 0;
        end
        b3 = (Q*t)/(rho_MS*cp_MS*(Tms_curr - T_S));

        b = b1 + b2 + b3;

        %Update molten salt temperature
        Tms_new = (Tms_curr - T_S)*exp(-b*t) + T_S;
    end
end
end
```

B.7 Solid Salt Sub-function Script

```
function Tss_new = SS(Tss, Ts, Tms_prev, Tms_curr, v, dz, t,
d_int, Lr)
%Approximate error between solid salt and steel temperatures (K)
Err = 0.0025;
```

```
Error = Ts - Tss;

if Error > Err
    %Molten Salt Liquidus Temperature
    T_L = 246 + 273.15;

    %Molten Salt Solidus Temperature
    T_S = 222 + 273.15;

    %Assume previous solid salt temperature if none is available
    if Tss == 0
        Tss = T_S;
    end

    %Molten salt phase
    if Tms_prev > T_L
        f_liquid_prev = 1;
    else if Tms_prev >= T_S && Tms_prev <= T_L
            f_liquid_prev = (Tms_prev - T_S)/(T_L - T_S);
        else
            f_liquid_prev = 0;
        end
    end

    %Molten salt phase
    if Tms_curr > T_L
        f_liquid_curr = 1;
    else if Tms_curr >= T_S && Tms_curr <= T_L
            f_liquid_curr = (Tms_curr - T_S)/(T_L - T_S);
        else
            f_liquid_curr = 0;
        end
    end

    %Receiver tube cross sectional area (m^2)
    A_cs = f_liquid_curr*pi*(d_int/2)^2;

    %Receiver tube internal circumferential area (m^2)
    A_int = sqrt(f_liquid_curr)*d_int*pi*dz;

    %The molten salt (MS) mass flow rate (kg/s)
    m_dot = rhoMS(Tms_curr)*v*A_cs;

    %Latent heat of fusion (J/kg)
    Lh = 161000;                        %(Archimede, n.d.)

    %Density
    rho_MS = rhoMS(Tms_curr);

    %MS specific heat
    cp_MS = cpMS(Tms_curr);

    %Inner radius of the frozen salt
    r_ints = sqrt(f_liquid_curr)*(d_int/2);
```

```
    %Cross sectional area of the solid salt (m^2)
    As_cs = (pi*(d_int/2)^2) - (pi*(r_ints)^2);

    %Mass of the solid salt control volume (kg)
    m_ss = As_cs*dz*rhoMS(Tss);

    %Convection heat transfer coefficient between the liquid and
solid salt
    if A_cs == 0
        A_cs = 0.01*pi*(d_int/2)^2;
    end
    Re = ((m_dot/A_cs)*d_int)/uMS(Tms_curr);
    f = 0.3164/(Re^0.25);
    %f = (0.790*log(Re) - 1.64)^(-2);
    PrMS = (cpMS(Tms_curr)*uMS(Tms_curr))/kMS(Tms_curr);
    if Re > 1500
        Nu      =      ((f/8)*(Re      -      1000)*PrMS)/(1      +
12.7*((f/8)^0.5)*((PrMS^(2/3)) - 1));
    else
        x_star = Lr/(d_int*Re*PrMS);
        Nu = 1.076*(x_star^(-1/3)) - 1.064;
        if Nu < 4.364
            Nu = 4.364;
        end
    end
    hmsLmsS = (kMS(Tms_curr)/d_int)*Nu;

    %Resistance between the liquid and the solid salt - convection
(K/W)
    RmsLmsS = 1/(hmsLmsS*A_int);

    %Heat transfer rate between the liquid and the solid salt -
convection (W)
    QmsLmsS = (1/RmsLmsS)*(Tss - Tms_curr);

    %Latent fusion heat energy change
    Q = (Lh*rhoMS(Tms_curr)/t)*(f_liquid_curr - f_liquid_prev);

    %Conduction heat transfer in the solid salt
    Rsalt = (log((d_int/2)/r_ints))/(2*pi*kMS(Tss)*dz);

    %Constant b
    if dz == 0 || f_liquid_curr == 0
        b1 = 0;
    else
        b1 = QmsLmsS/(m_ss*cpMS(Tss)*(Tss - Ts));
    end
    b2 = (Q*t)/(rho_MS*cp_MS*(Tss - Ts));

    %Mass of the solid salt control volume (kg)
    m_salt = As_cs*dz*rhoMS(Tss);

    b3 = 1/(m_salt*cpMS(Tss)*Rsalt);

    b = b1 + b2 + b3;
```

```
    %Update solid salt temperature
    Tss_new = (Tss - Ts)*exp(-b*t) + Ts;
else
    Tss_new = Ts;
end
end
```

B.8 Receiver Tube Sub-function Script

```
%Steel receiver tube sub-function

function Ts_new = Steelt(Ta, Ts, Tms, Tss, dz, v, t, d_ext, d_int,
Lr)
%Gravity (m/s^2)
g = 9.81;

%Molten Salt Liquidus Temperature
T_L = 246 + 273.15;

%Molten Salt Solidus Temperature
T_S = 222 + 273.15;

%Error to approximate a liquid fraction of 1
Err = 0.01;

%Molten salt phase
if Tms > T_L
    f_liquid = 1;
else if Tms >= T_S && Tms <= T_L
        f_liquid = (Tms - T_S)/(T_L - T_S);
    else
        f_liquid = 0;
    end
end

Error = 1 - f_liquid;

%Test to see if the liquid fraction is sufficiently close too 1
if Error < Err
    f_liquid = 1;
end

%Temperature of the rain (K)
Train = 5 + 273.15;

%Rain depth during a violent shower (mm)
Rain_depth = 50;

%Rain intensity (kg/m^2s)
Vrain = (((Rain_depth/1000)*1*1)*1000)/(60*60);

%Temperature difference between the steel tube and the rain water
(K)
```

```
dT = Ts - Train;

%Wind speed
v_wind = (103*1000)/(60*60);

%Direct Normal Irradiation (DNI) (W/m^2)
DNI = 50;

%Concentration ratio
C = 600;

%Stephan-Boltzmann constant (W/m^2.K^4)
sigma = 5.67*(10^-8);

%Steel tube emissivity
emiss_s = 0.88;                     %(Serrano 2017)

%Shape factor between steel tube and the sky
Fssky = 1;

%Receiver tube external circumferential area (m^2)
A_ext = d_ext*pi*dz;

%Receiver tube internal circumferencial area (m^2)
A_int = sqrt(f_liquid)*d_int*pi*dz;

%Receiver tube cross sectional area (m^2)
A_cs = f_liquid*pi*(d_int/2)^2;

%The molten salt (MS) mass flow rate (kg/s)
m_dot = rhoMS(Tms)*v*A_cs;

%Heat transfer coefficient between steel and air (W/m^2.K)
Tmean = (Ta + Ts)/2;
beta = 1/Tmean;
Ra = ((beta*(Ts - Ta)*g*d_ext^3)/((vAIR(Tmean))^2))*PrAIR(Tmean);
Nu       =       0.36       +       (0.518*(Ra^(1/4)))/((1       +
(0.559/PrAIR(Tmean))^(9/16))^(4/9));
hsa = (kAIR(Tmean)/d_ext)*Nu;

%Heat transfer coefficient between steel and sky (W/m^2.K)
hssky = emiss_s*Fssky*sigma*((Ts^2) + (Ta^2))*(Ts + Ta);

%Resistance between steel and air - convection (K/W)
Rsa = 1/(hsa*A_ext);

%Resistance between steel and sky - convection (K/W)
Rssky = 1/(hssky*A_ext);

if f_liquid == 1
    %Heat transfer coefficient between the steel receiver tube and
the MS (W/m^2.K)
    Re = ((m_dot/A_cs)*d_int)/uMS(Tms);
    f = 0.3164/(Re^0.25);
    PrMS = (cpMS(Tms)*uMS(Tms))/kMS(Tms);
```

```
    if Re > 1500
        Nu      =      ((f/8)*(Re      -      1000)*PrMS)/(1      +
12.7*((f/8)^0.5)*((PrMS^(2/3)) - 1));
    else
        x_star = Lr/(d_int*Re*PrMS);
        Nu = 1.076*(x_star^(-1/3)) - 1.064;
        if Nu < 4.364
            Nu = 4.364
        end
    end
    hsms = (kMS(Tms)/d_int)*Nu;

    %Resistance between the steel receiver tube and the MS -
convection (K/W)
    Rsms = 1/(hsms*A_int);

    %Heat transfer rate between the steel receiver tube and the MS
- convection (W)
    Qsms = (1/Rsms)*(Ts - Tms);

else if f_liquid < 1
     %Conduction heat transfer in the solid salt
     r_ints = sqrt(f_liquid)*(d_int/2);
     Rsalt = (log((d_int/2)/r_ints))/(2*pi*kMS(Tss)*dz);

     %Heat transfer rate between the steel receiver tube and the
salt - conduction (W)
     Qsms = (1/Rsalt)*(Ts - Tss);
     end
end

%Heat transfer rate from the sun incident on the steel tube (W)
Qdni = C*DNI*0.5*A_ext;

%Heat transfer coefficient between the steel receiver tube and the
rain (W/m^2.K)
hsr    =    (190+25)    +    (tanh(Vrain/8))*((140+4)*Vrain*(1    -
((Vrain*dT)/((72000+3500))))     +     (3.26+0.16)*(dT^2)*(1     -
tanh(dT/(128+1.6))));       %(Wendelstorf et al. 2008)

%Resistance between the steel receiver tube and the rain -
convection (K/W)
Rsr = 1/(hsr*A_ext);

%Heat transfer coefficient due to wind over steel receiver tube
(W/m^2.K)
Tmean = (Ts + Ta)/2;
Re_w = (v_wind*d_ext)/vAIR(Tmean);
if Re_w <= 10^4
    Nu_w = 0.3 + ((0.62*(Re_w^(1/2))*(PrAIR(Tmean)^(1/3)))/((1 +
((0.4/PrAIR(Tmean))^(2/3)))^(1/4)));
else if Re_w > 10^4 && Re_w <= 4*(10^5)
        Nu_w = 0.3 + ((0.62*(Re_w^(1/2))*(PrAIR(Tmean)^(1/3)))/((1
+ ((0.4/PrAIR(Tmean))^(2/3)))^(1/4)))*(1 + ((Re_w/282000)^(1/2)));
    else
```

```
        Nu_w = 0.3 + ((0.62*(Re_w^(1/2))*(PrAIR(Tmean)^(1/3)))/((1
+             ((0.4/PrAIR(Tmean))^(2/3)))^(1/4)))*((1             +
((Re_w/282000)^(5/8)))^(4/5));
     end
end
hsw = (kMS(Tmean)/d_ext)*Nu_w;

%Resistance due to wind over steel receiver tube (K/W)
Rsw = 1/(hsw*A_ext);

%Steel density (kg/m^3)
rho_s = 8000;                                   %(Xu et al. 2016)

%Steel specific heat capacity (J/Kg.K)
cp_s = 455;                                   %(Xu et al. 2016)

%Cross sectional area of the steel (m^2)
As_cs = (pi*(d_ext/2)^2) - (pi*(d_int/2)^2);

%Mass of the steel control volume (kg)
m_s = As_cs*dz*rho_s;

dTsa = Ts - Ta;
err = 0.5;
if dTsa < err
    Ts = Ts + err;
end

%Constant b (DNI)
%b   =   Qsms/(m_s*cp_s*(Ts   -   Ta))   +   (1/(m_s*cp_s*Rsa))   +
(1/(m_s*cp_s*Rssky)) - Qdni/(m_s*cp_s*(Ts - Ta));
%Constant b (Rain, Wind)
%b   =   Qsms/(m_s*cp_s*(Ts   -   Ta))   +   (1/(m_s*cp_s*Rsa))   +
(1/(m_s*cp_s*Rssky)) + (1/(m_s*cp_s*Rsr)) + (1/(m_s*cp_s*Rsw));
%Constant b (Rain)
%b   =   Qsms/(m_s*cp_s*(Ts   -   Ta))   +   (1/(m_s*cp_s*Rsa))   +
(1/(m_s*cp_s*Rssky)) + (1/(m_s*cp_s*Rsr));
%Constant b (Wind)
%b   =   Qsms/(m_s*cp_s*(Ts   -   Ta))   +   (1/(m_s*cp_s*Rsa))   +
(1/(m_s*cp_s*Rssky)) + (1/(m_s*cp_s*Rsw));
%Constant b (Nothing)
b   =   Qsms/(m_s*cp_s*(Ts   -   Ta))   +   (1/(m_s*cp_s*Rsa))   +
(1/(m_s*cp_s*Rssky));

%Update steel temperature (K)
Ts_new = (Ts - Ta)*exp(-b*t) + Ta;
end
```

REFERENCES

Alexiades, V., 1992. *Mathematical modeling of melting and freezing processes*, CRC Press.

Ambrosini, A. et al., 2011. Improved high temperature solar absorbers for use in concentrating solar power central receiver applications. In *ASME 2011 5th International Conference on Energy Sustainability*. pp. 587–594.

Archimede, Molten Salt Properties. Available at: http://www.archimedesolarenergy.it/molten_salt.htm [Accessed January 17, 2017].

Association, N.E.S.T., Classification of Wind Speeds. Available at: http://www.windows2universe.org/earth/Atmosphere/wind_speeds.html [Accessed January 25, 2017].

Azizian, K. et al., 2011. Analysis of shiraz solar thermal power plant response time. *Journal of Clean Energy Technologies*, 1(1), pp.22–26.

Biencinto, M. et al., 2014. Simulation and assessment of operation strategies for solar thermal power plants with a thermocline storage tank. *Solar Energy*, 103, pp.456–472.

Blair, N., Mehos, M. & Christensen, C., 2008. Sensitivity of concentrating solar power trough performance, cost, and financing with the Solar Advisor Model. Las Vegas, Nevada, USA, March 2008. In *Proceedings of the SolarPACES International Symposium*.

Cardozo, F.R., 2012. *Concentrating Solar Power Technologies using Molten Salts for Storage and Production of Energy*.

Delameter, W.R. & Bergan, N.E., 1986. *Review of the Molten Salt Electric Experiment: A solar central receiver project*,

DNV.GL, 2014. OPTIMIZING CONCENTRATING SOLAR POWER WITH THERMAL ENERGY STORAGE SYSTEMS IN CALIFORNIA. *California Energy Commission*.

Dobos, A., Neises, T. & Wagner, M., 2014. Advances in CSP simulation technology in the System Advisor Model. *Energy Procedia*, 49, pp.2482–2489.

Doupis, D. et al., 2016. Transient simulation of molten salt central receiver. In *SOLARPACES 2015: International Conference on Concentrating Solar Power and Chemical Energy Systems*. p. 030013.

El Hefni, B. & Soler, R., 2015. Dynamic Multi-configuration Model of a 145 MWe Concentrated Solar Power Plant with the ThermoSysPro Library (Tower Receiver, Molten Salt Storage and Steam Generator). *Energy Procedia*, 69, pp.1249–1258.

Falchetta, M. & Rossi, A., 2014. Dynamic simulation of the operation of a molten salt parabolic trough plant, comprising draining procedures. *Energy Procedia*, 49, pp.1328–1339.

Falcone, P.K., 1986. *A handbook for solar central receiver design*,

Ferri, R., Cammi, A. & Mazzei, D., 2008. Molten salt mixture properties in RELAP5 code for thermodynamic solar applications. *International Journal of Thermal Sciences*, 47(12), pp.1676–1687.

Grena, R. et al., 2010. Detection of frozen salt in pipes using gamma-ray spectrometry of potassium self-activity. *Solar Energy*, 84(1), pp.51–58.

Hartnett, J.P. et al., 1998. *Advances in heat transfer*, Academic press.

Heller, L., 2013. Literature review on heat transfer fluids and thermal energy storage systems in CSP plants. *STERG Report, May*, 31.

Hibiki, T. & Ishii, M., 2003. One-dimensional drift-flux model and constitutive equations for relative motion between phases in various two-phase flow regimes. *International Journal of Heat and Mass Transfer*, 46(25), pp.4935–4948.

High Temp Metals, 2015. INCONEL 625 TECHNICAL DATA. Available at: http://www.hightempmetals.com/techdata/hitempInconel625data.php [Accessed July 21, 2017].

Hirt, C.W. & Nichols, B.D., 1981. Volume of fluid (VOF) method for the dynamics of free boundaries. *Journal of computational physics*, 39(1), pp.201–225.

Jafari, M., 2014. Analysis of heat transfer in spray cooling systems using numerical simulations.

Janz, G.J. & Tomkins, R.P., 1980. Molten Salts: Vol. 5, Part 1, Additional Single and Multi-Component Salt Systems. Electrical Conductance, Density, Viscosity, and Surface Tension Data. *Journal of Physical and Chemical Reference Data*, 9(4), pp.831–1022.

Kearney, D. et al., 2003. Assessment of a molten salt heat transfer fluid in a parabolic trough solar field. *Journal of solar energy engineering*, 125(2), pp.170–176.

Koo, J. & Kleinstreuer, C., 2003. Liquid flow in microchannels: experimental observations and computational analyses of microfluidics effects. *Journal of Micromechanics and Microengineering*, 13(5), p.568.

Liao, Z. et al., 2015. Numerical Model and Validation for Simulating the Cold Filling of the Molten Salt Receiver Tube. *Energy Procedia*, 69, pp.451–460.

Liao, Z. et al., 2014. Phase change of molten salt during the cold filling of a receiver tube. *Solar Energy*, 101, pp.254–264.

Lu, J., Ding, J. & Yang, J., 2013. Filling dynamics and phase change of molten salt in cold receiver pipe during initial pumping process. *International Journal of Heat and Mass Transfer*, 64, pp.98–107.

Lu, J., Ding, J. & Yang, J., 2010. Solidification and melting behaviors and characteristics of molten salt in cold filling pipe. *International Journal of Heat and Mass Transfer*, 53(9), pp.1628–1635.

Manenti, F. & Ravaghi-Ardebili, Z., 2013. Dynamic simulation of concentrating solar power plant and two-tanks direct thermal energy storage. *Energy*, 55, pp.89–97.

Mills, A.F. & Ganesan, V., 2015. *Heat Transfer* Second. Dorling Kindersley, ed., Pearson.

NERL, 2015. Integrated Layout and Optimization Tool for Solar Power Towers. Available at: http://www.nrel.gov/csp/solarpilot.html [Accessed September 7, 2016].

Ortega, J.I., Burgaleta, J.I. & TÃ\vSllez, F.M., 2008. Central receiver system solar power plant using molten salt as heat transfer fluid. *Journal of Solar energy engineering*, 130(2), p.024501.

Pacheco, J.E. et al., 1995. *Results of molten salt panel and component experiments for solar central receivers: cold fill, freeze/thaw, thermal cycling and shock, and instrumentation tests*,

Pacheco, J.E. & Dunkin, S.R., 1996. Assessment of molten-salt solar central-receiver freeze-up and recovery events. *Solar Engineering*, pp.85–90.

Pletcher, R.H., Tannehill, J.C. & Anderson, D., 2012. *Computational fluid mechanics and heat transfer*, CRC Press.

Santini, R. et al., 1984. Measurement of thermal conductivity of molten salts in the range 100-500° C. *International journal of heat and mass transfer*, 27(4), pp.623–626.

Senge, P.M. & Forrester, J.W., 1980. Tests for building confidence in system dynamics models. *System dynamics, TIMS studies in management sciences*, 14, pp.209–228.

Serrano-López, R., Fradera, J. & Cuesta-López, S., 2013. Molten salts database for energy applications. *Chemical Engineering and Processing: Process Intensification*, 73, pp.87–102.

Sloan, S., Schultz, R. & Wilson, G., 1994. *RELAP5/MOD3 code manual*,

Suárez, C. et al., 2015. Transient analysis of the cooling process of molten salt thermal storage tanks due to standby heat loss. *Applied Energy*, 142, pp.56–65.

Terdalkar, R. et al., 2015. Transient Simulation of High Temperature High Pressure Solar Tower Receiver. *Energy Procedia*, 69, pp.1451–1460.

Thriumalai, N. et al., 2014. Global Review of Solar Tower Technology. *STEP*.

USGS, 2016. How much rain falls during a storm? Available at: https://water.usgs.gov/edu/activity-howmuchrain-metric.html [Accessed January 25, 2017].

Vergura, S. & Di Fronzo, V., 2012. Matlab based Model of 40-MW Concentrating Solar Power Plant. In *Internation Conference on Renewable Energies and Power Quality (ICREPQ'12)*. p. 41.

Voile, V. & Prakash, C., 1987. A fixed grid numerical modeling methodology for convection diffusion mushy region phase-change problem. *International Journal Heat Mass Transfer*, 30(9), pp.1709–1719.

Wagner, M., Blair, N. & Dobos, A., 2010. A detailed physical trough model for NREL's Solar Advisor Model. In *Proceedings of the SolarPACES International Symposium, SolarPACES. NREL/CP-5500-49368*.

Wagner, P.H. & Wittmann, M., 2014. Influence of different operation strategies on transient solar thermal power plant simulation models with molten salt as heat transfer fluid. *Energy Procedia*, 49, pp.1652–1663.

Walker, W.E. et al., 2003. Defining uncertainty: a conceptual basis for uncertainty management in model-based decision support. *Integrated assessment*, 4(1), pp.5–17.

Wendelstorf, J., Spitzer, K.-H. & Wendelstorf, R., 2008. Spray water cooling heat transfer at high temperatures and liquid mass fluxes. *International Journal of Heat and Mass Transfer*, 51(19), pp.4902–4910.

White, F.M. & Corfield, I., 2006. *Viscous fluid flow*, McGraw-Hill New York.

Wu, Y.-T. et al., 2012. Investigation on forced convective heat transfer of molten salts in circular tubes. *International Communications in Heat and Mass Transfer*, 39(10), pp.1550–1555.

Xu, T. et al., 2017. Numerical study of cold filling and tube deformation in the molten salt receiver. In *AIP Conference Proceedings*. p. 070007.

Yan, W., Tsay, Y. & Lin, T., 1989. Transient conjugated heat transfer in laminar pipe flows. *International Journal of Heat and Mass Transfer*, 32(4), pp.775–777.

Yang, X. et al., 2012. Numerical simulation study on the heat transfer characteristics of the tube receiver of the solar thermal power tower. *Applied Energy*, 90(1), pp.142–147.

Yang, Z. & Garimella, S.V., 2013. Cyclic operation of molten-salt thermal energy storage in thermoclines for solar power plants. *Applied energy*, 103, pp.256–265.

Zaversky, F. et al., 2013. Object-oriented modeling for the transient performance simulation of parabolic trough collectors using molten salt as heat transfer fluid. *Solar Energy*, 95, pp.192–215.

Zhang, Q. et al., 2015. Modeling and simulation of a molten salt cavity receiver with Dymola. *Energy*, 93, pp.1373–1384.